Durham E-Theses

New methods for the computer simulation of macromolecular liquid crystals

Hughes, Zak Elliot

How to cite:

Hughes, Zak Elliot (2006) *New methods for the computer simulation of macromolecular liquid crystals*, Durham theses, Durham University. Available at Durham E-Theses Online: http://etheses.dur.ac.uk/2339/

Use policy

New Methods for the Computer Simulation of Macromolecular Liquid Crystals

Zak Elliot Hughes

Department of Chemistry

Durham University

October 2006

Submitted in the partial fulfilment of the requirements for

the degree of

Doctor of Philosophy

2 9 NOV 2006

Abstract

New Methods for the Computer Simulation of Macromolecular Liquid Crystals

Zak Elliot Hughes

Molecular simulation of macromolecular liquid crystal (LC) systems has so far been limited by a number of factors: the large size of the molecules themselves and the fact that mesophase formation takes place on length and timescales that are not reasonable to simulate. The work in this thesis develops three methods that can be used to assist in the computer simulation of macromolecular LC systems.

Coarse-graining is a technique where instead of representing every atom within a molecule as a single site, a number of atoms are grouped into interaction centres. This coarse-graining procedure has been applied to a liquid crystal dendrimer to enable the bulk phase simulation of the molecule to be studied. The analysis of the results show that the behaviour for the coarse-grained model closely matches that of a more detailed atomistic model. Phase behaviour in the bulk matches results from X-ray data.

The parallel-tempering method (replica exchange method) uses a series of replicas of the same system at different temperatures to improve the sampling of phase space. This technique was applied to two different systems, a bulk phase simulation of an alkane chain and the gas phase simulation of a silsesquioxane liquid crystal dendrimer. The method was then extended to work with a set of replicas which used different potentials. The Tsallis potential was used to soften potentials and allow replicas to sample a greater area of phase space.

A third simulation method was applied which used soft-core potentials. This attempted to address the problem of the long timescales needed to see the formation of mesophases in macromolecular systems. Three different anisotropic single site soft-core models were developed and tested for liquid crystals. The results show that the time needed for mesophase formation is reduced for soft-core models and that these models are able to form multiple liquid crystal phases. In addition, the

most promising of these soft-core models has been applied to the simulation of more complex liquid crystal systems, represented by multi-site models.

Declaration

The work in this thesis is based on research carried out at Durham University. The material contained in this thesis has not previously been submitted for any other degree at Durham University or any other institution. The research within this thesis has been conducted by the author unless indicated otherwise.

The copyright of this thesis rests with the author. No quotations from it should be published without the author's prior consent and information derived from it should be acknowledged.

<div align="center">

Zak Elliot Hughes

October 2006

</div>

Acknowledgments

Contents

List of Figures

List of Tables

Chapter 1

Liquid Crystal Macromolecules

1.1   Liquid Crystals

There are a wide range of systems which exhibit a degree of molecular order that is intermediate to that seen in conventional liquids and crystals. These semi-ordered phases still possess some of the fluid properties of liquids, and are known as liquid crystal phases (or mesophases). Liquid crystals (mesogens) have been around for some time, with Friedich Reinitzer[1] discovering in 1888 that cholesteryl benzoate had two melting points, the first being the transition from a crystal to a liquid crystal phase (in this case a chiral nematic) and the second from the mesophase to the isotropic liquid. The classification of a number of different mesophases was achieved by Georges Friedel[2] in 1922 ensuring that the idea of liquid crystal phases was accepted by the scientific community.

Today liquid crystals are used in many commercial applications. The most obvious of these being the rapid growth in the use of liquid crystal display (LCD) technology.[3-5] However, liquid crystals are also have applications as lubricants,[6] in lasers[7,8] as templates for mesoporous materials[9] and in a number of other areas. In most cases applications arise from the anisotropic properties of the liquid crystal phases and their constituent molecules. The importance of these applications in the world today provides the need to understand liquid crystals better.

Liquid crystals can largely be divided into two different types; thermotropic and lyotropic. Thermotropic liquid crystals are characterised by the fact that the

1

transition between non-liquid crystalline phases and liquid crystalline phases are due to a change in temperature whereas in lyotropic systems phase transitions are also caused by changes in concentration.

1.2 Liquid Crystal Phases

1.2.1 Thermotropic Liquid Crystals

Thermotropic liquid crystal molecules are usually anisotropic in shape, being either prolate (rod like) or oblate (disk like) with the shape of the liquid crystal molecule playing an important role in determining the mesophases formed. The widely varying chemical structures of liquid crystal molecules has led to large number of different liquid crystal phases, some very complex. Some of the most common phases are outlined below.

For prolate LCs the most common LC phases formed are the nematic and smectic-A phases. Nematic mesophases (N) (see figure 1.1) are characterised by having some long-range orientational order but no long range translational order. The molecules prefer to align so that their long axes are roughly parallel to each other. The sum of the orientational alignments of the molecules gives a unit vector called the director, **n**, and degree of orientational order of the mesophase is measured by the order parameter, S_2, given by

$$S_2 = \left\langle \frac{3}{2} \cos^2 \theta - \frac{1}{2} \right\rangle, \tag{1.1}$$

where θ is the angle between the long axis of the mesogenic molecule and the director and the angular brackets denote an ensemble average. In the cholesteric (chiral nematic) mesophase (N*) the director rotates in a helix about an axis perpendicular to the director making the phase chiral. Depending on the chirality, the direction of rotation can be clockwise or anti-clockwise. The distance over which molecules rotates by 2π is known as the pitch, P (see figure 1.2).

Smectic phases not only have some long range orientational order (usually greater than that possessed by a nematic phase) but also have a degree of translational
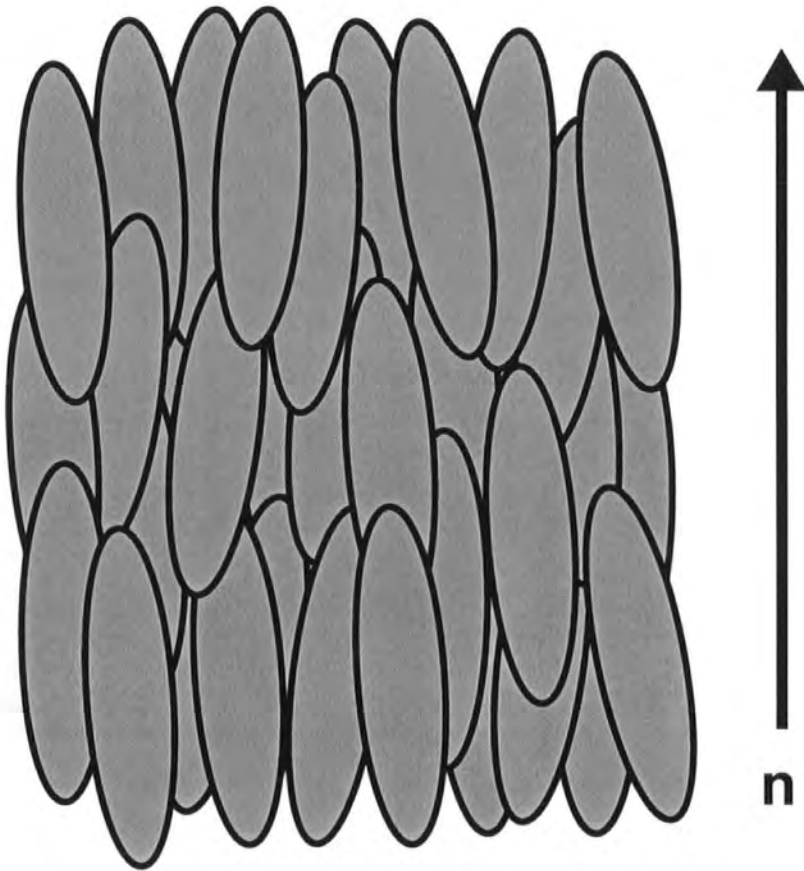
Figure 1.1: A schematic diagram of a nematic liquid crystal phase.
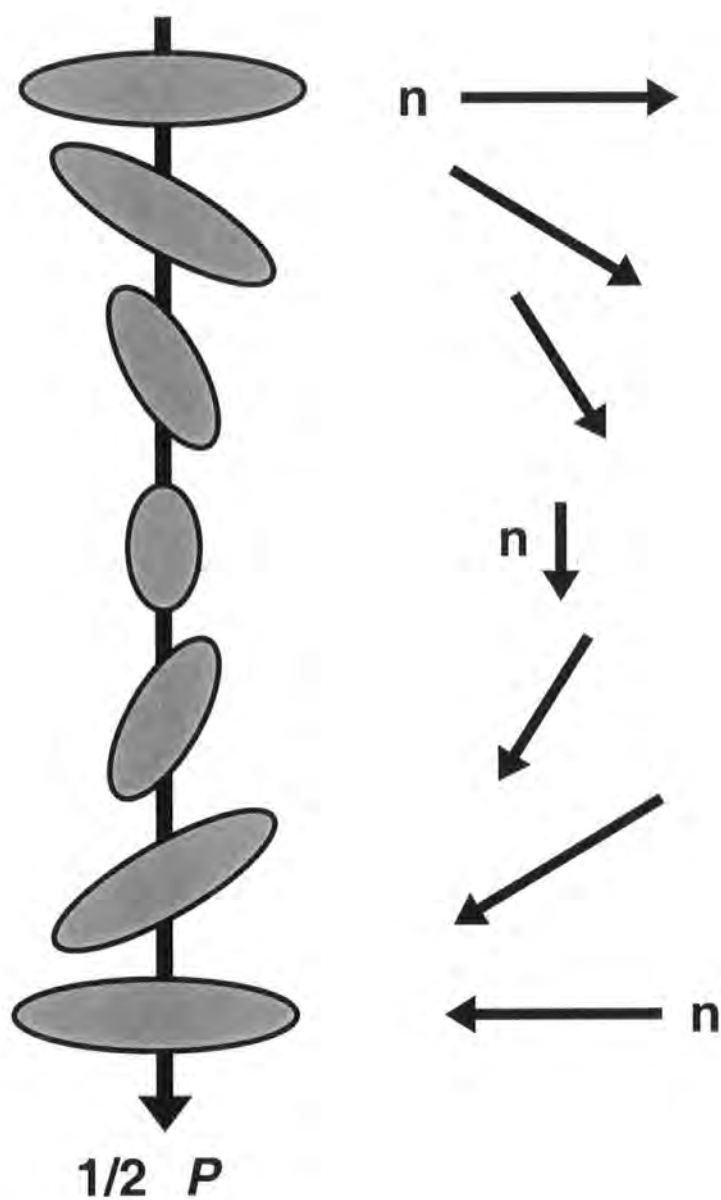
Figure 1.2: Showing how the director rotates in a helix about an axis perpendicular to the director, in a cholesteric liquid crystal phase.

order. The liquid crystal molecules will form into layers, with the molecules having translational freedom within the layers but not between layers. The type of smectic phase formed is determined by how the layers are aligned. There are a large number of smectic phases but the two most common are the smectic-A phase (SmA), where the layers are aligned perpendicularly to the director, and the smectic-C phase (SmC), where the layers are titled at an angle, θ, to the director (both shown in figure 1.3).

The phases formed by discotic liquid crystals are more-or-less analogous to those formed by calamitic molecules. A discotic nematic phase has orientational order but no long range translational order in the same way as a normal nematic phase. However, here it is the short axes of the molecules which align, (likewise with the chiral discotic nematic and a normal chiral nematic phases). Columnar phases[10,11] (Col) occur when the mesogens stack on top of each other forming columns which can then pack together, most often in a hexagonal or rectangular lattice.

1.2.2 Lyotropic Liquid Crystals

Lyotropic crystal systems[12] consist of at least two components, and the formation of a liquid crystal phase is based not only on the temperature but upon the ratio of these components. An example of a typical lyotropic system would be the mesophases formed from amphiphilic molecules in water. Amphiphiles are molecules consisting of two general parts; a polar head-group and one or more non-polar (usually organic) tails. If the concentration of amphiphiles is low then it is likely that the amphiphiles will try to form micelles where the polar head groups form a shell around the hydrophobic tails protecting them from the water. If the concentration of the amphiphiles is increased then these micelles become too large to be stable and instead other liquid crystal phases are formed such as the lamellar phase (consisting of a bilayer of the amphiphiles) or the hexagonal phase (where amphiphiles assemble into cylinders, which in turn pack into an hexagonal array).
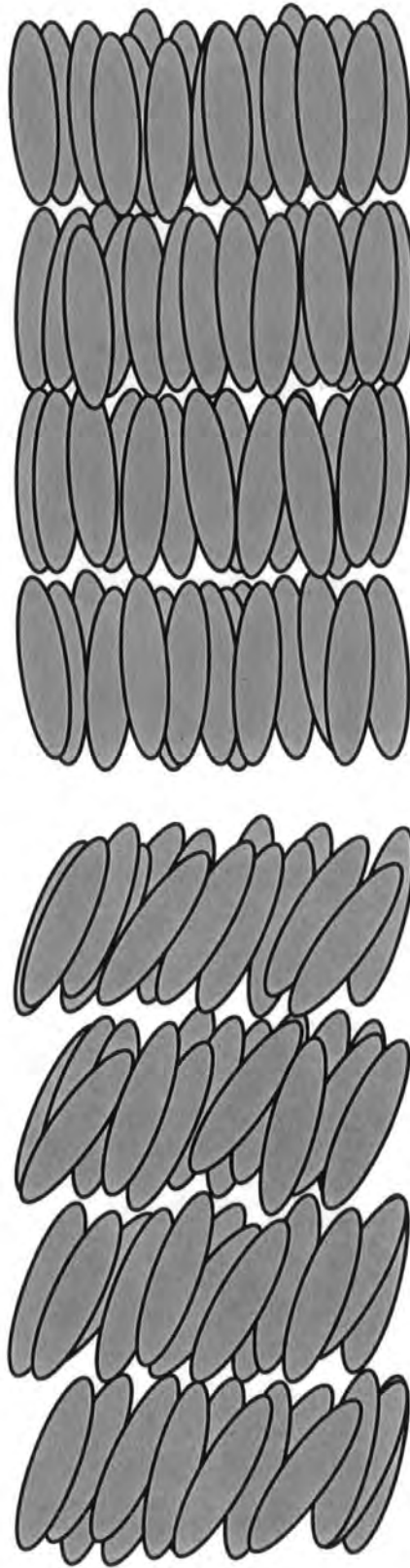
Figure 1.3: Schematic diagram of liquid crystal smectic phases:(Top) smectic-A phase and (bottom) smectic-C phase
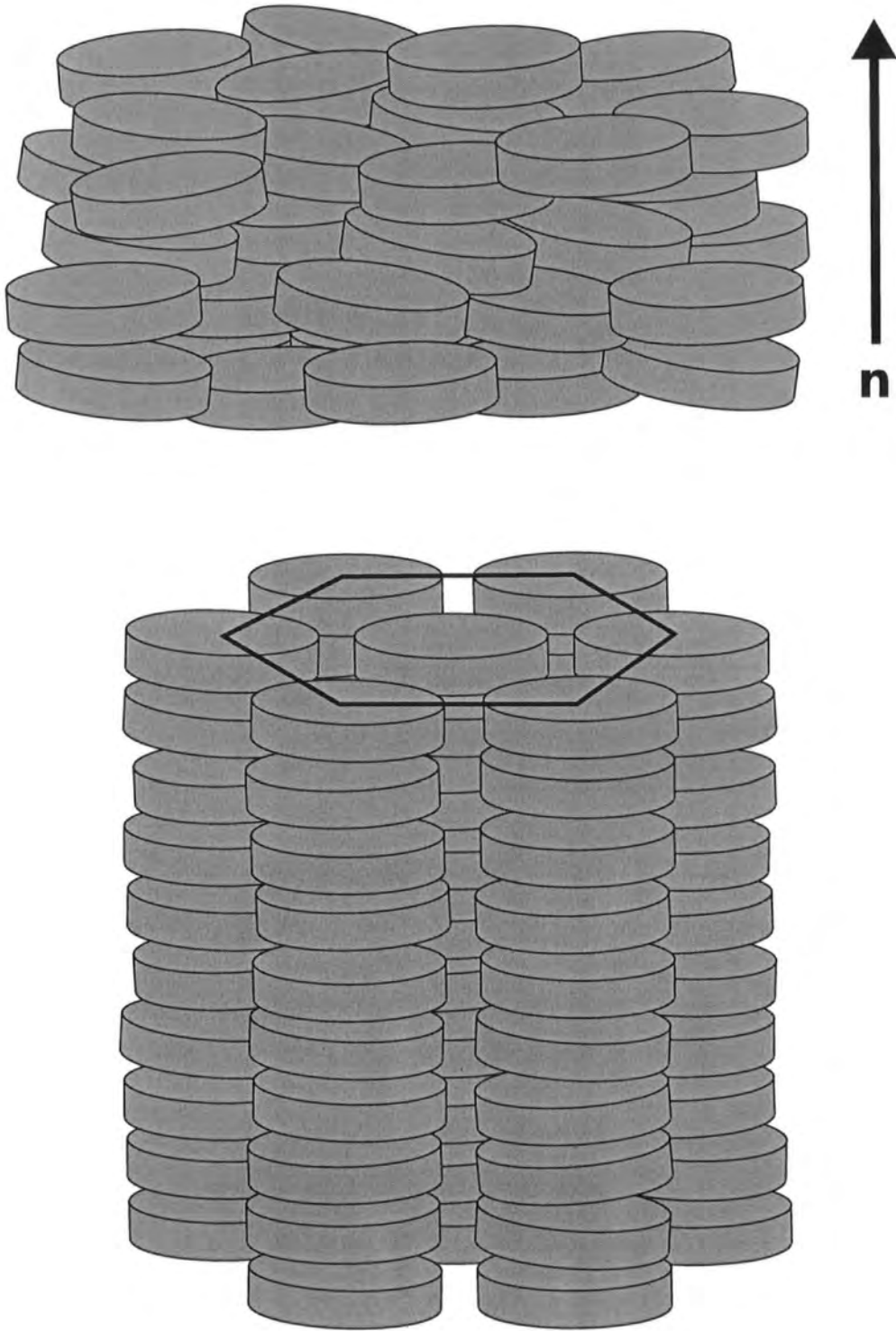
Figure 1.4: A Schematic diagram of liquid crystal discotic phases: a discotic nematic phase (top) and a hexagonal columnar phase (bottom)

Water   Water
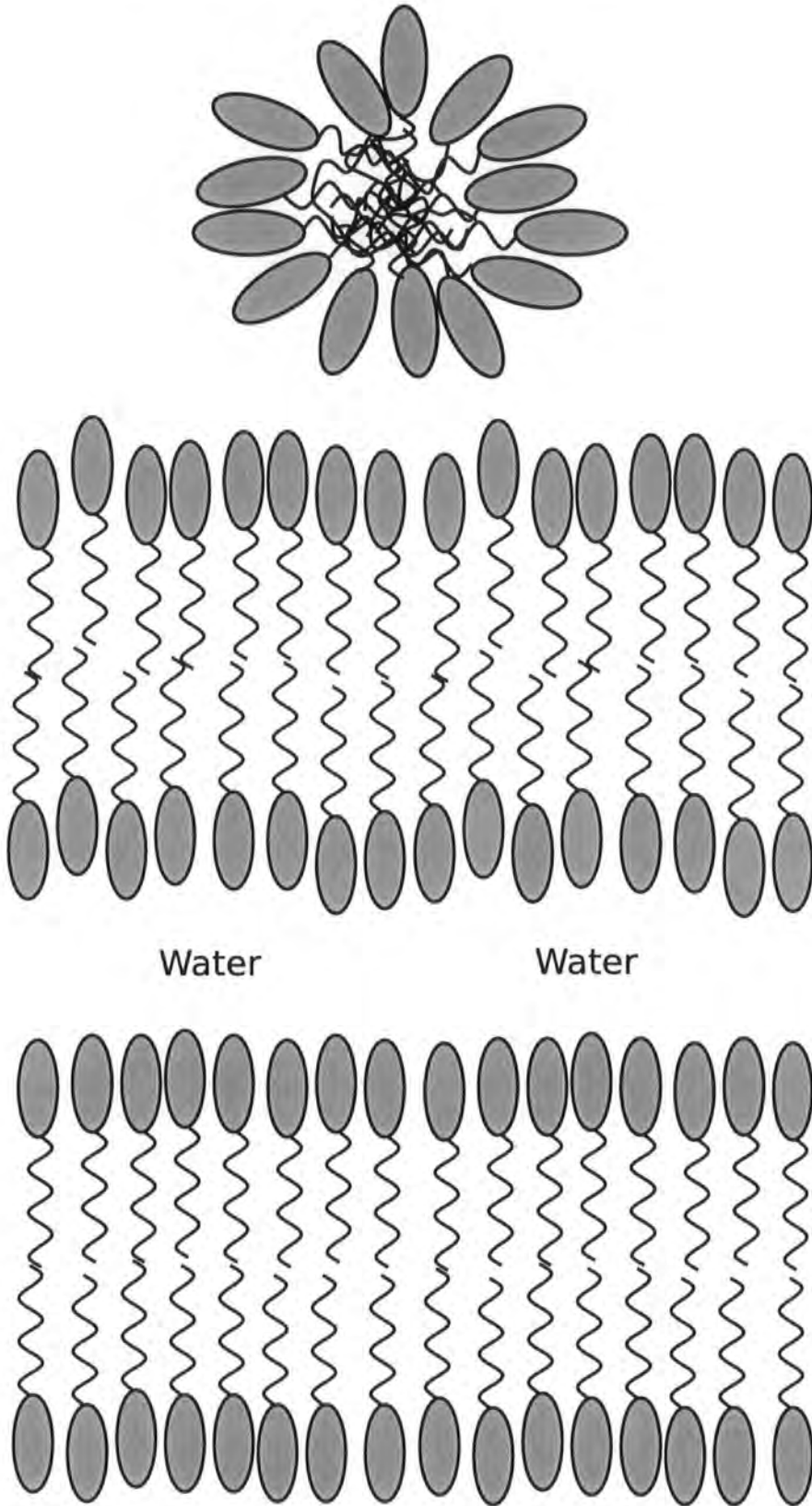
Figure 1.5: Schematic representations of some lyotropic systems: a micelle (top) and a lamellar phase (bottom).

1.3   Liquid Crystal Macromolecules

Experimental, theoretical and computational studies of liquid crystals have been carried out for some time and many low molecular weight liquid crystal systems are now quite well understood. Recent interest has therefore turned to more unusual liquid crystal systems and improved synthetic techniques have allowed large macromolecular systems (polymers or dendrimers) containing mesogens to be made.[13-21] These systems will form many of the "normal" liquid crystal phases but have also shown a large range of new mesophase morphologies.[21-23] One of the driving forces for the synthesis (and thus simulation) of these macromolecular liquid crystals is that they have quite a large number of potential applications[19,24] particularly on the nano-scale level. For example potential uses of liquid crystal dendrimers include their use as a scaffold for metal complexes in catalysis,[19,24-26] in host-guest chemistry[27] and as a precursor molecule to the creation of nano-scale polymer networks.[28,29]

The formation of mesophases in these systems is linked to how the various different parts of the macromolecule (such as mesogenic groups, the organic backbone of a polymer or the rigid core in a dendrimer) interact with each other. Thus by controlling the architecture of the macromolecule it is possible to control the phase behaviour and consequently the electronic and optical properties of the system.

The most common macromolecular liquid crystal systems are liquid crystal polymers[30-32] and dendrimers[16,17,33] but other systems can be constructed such as systems built from a fullerene unit and dendrons.[33-35]

1.3.1   Liquid Crystal Polymers

The different ways of arranging the mesogens with respect to the polymer backbone in liquid crystal polymers (LCPs) leads to a number of different types of polymer systems. If the mesogens are incorporated directly into the polymer backbone then you have a main chain liquid crystal polymer (MCLCP), within which the mesogens can be attached either parallel to the polymer backbone (giving a terminal system) or perpendicular to it (a lateral system) (see figure 1.6).

Alternatively, if you have a short linker group running from the carbon backbone

and connecting to the mesogen then you have a side chain liquid crystal polymer. Again the mesogens can be arranged either terminally (the linker connecting to the end of the liquid crystal) or laterally (the side-chain connecting to the long axis of the molecule). The large number of ways of arranging the mesogens within the molecules means that a large number of different types of systems can be built from just a few building blocks. So using only one type of liquid crystal and organic backbone but varying how these parts are arranged you can create a number of different polymer architectures:

- a main chain terminal liquid crystal polymer

- a main chain lateral liquid crystal polymer

- a side chain terminal liquid crystal polymer

- side chain lateral liquid crystal polymer

- a side-chain liquid crystal with alternating terminal and lateral mesogens etc.

If the number of building blocks used in the macromolecule is increased, by using two different types of mesogen for example, then the number of possible polymer systems increases rapidly and some very complex systems can be created.

1.3.2 Liquid Crystal Dendrimers

As with LCPs, liquid crystal dendrimers (LCDr) have a large number of ways in which mesogenic units can be arranged. In addition they have an additional variable arising from the fact that the generation of the dendrimer can be altered. The generation of a dendrimer corresponds to the number of branching points the dendrimer has, excluding the central branch (see figure 1.7). Systems that branch out in a single direction, thus forming a wedge type shape rather than a sphere are called dendrons. These can also have mesogenic units connected to them and can form mesophases. Liquid crystal dendrimers can have an advantage over polymers, in that they can have a high concentration of mesogenic end groups but do not suffer from the entanglement problem that polymers do. The latter sometimes stops mesogenic groups in polymers from self-organising
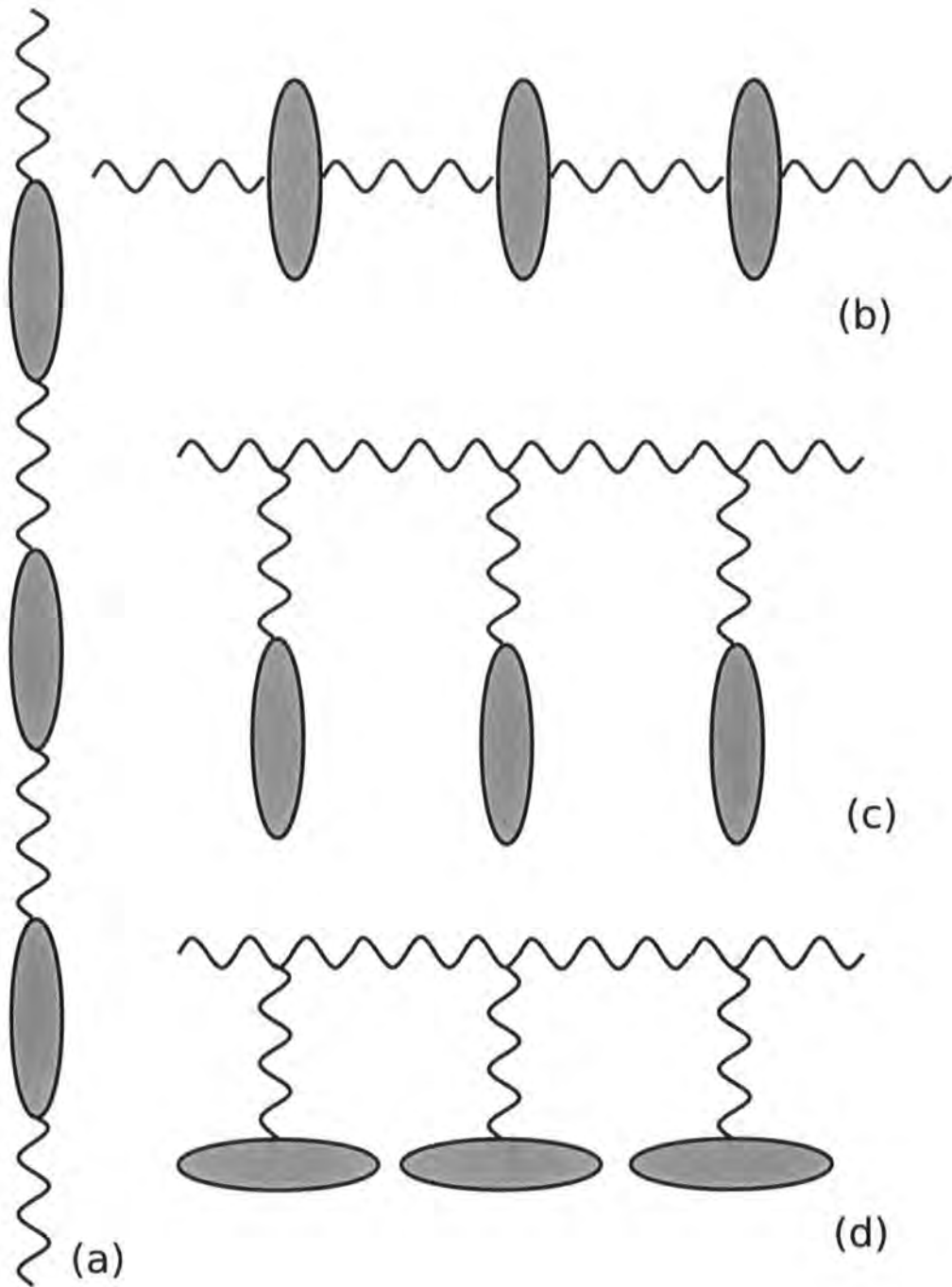
Figure 1.6: LC polymers: (a) main chain terminal polymer, (b) main chain lateral polymer, (c) terminal side chain polymer and (d) lateral side chain polymer.
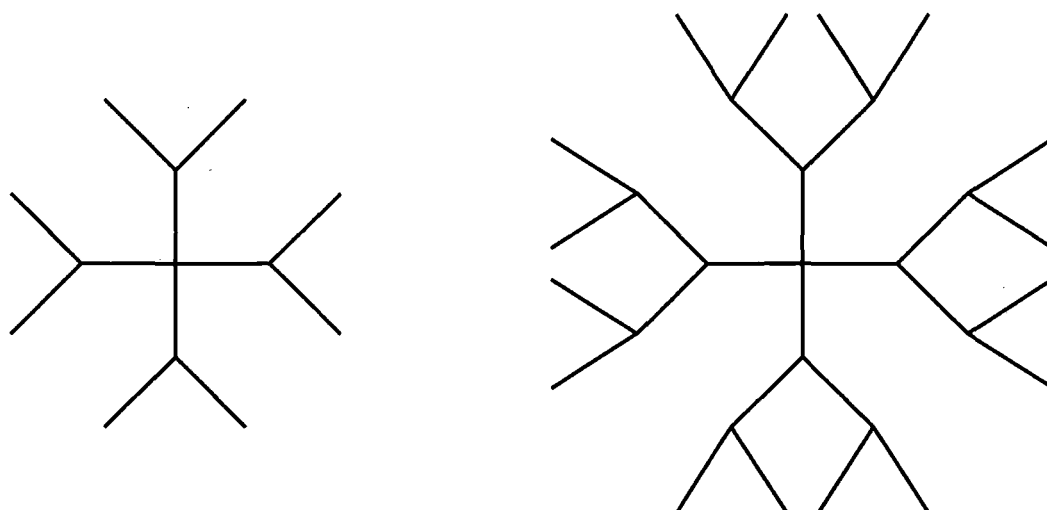
Figure 1.7: A first generation dendrimer (left) and a second generation dendrimer (right).

Most liquid crystal dendrimer systems can be divided into three different parts: a rigid central core, a set of flexible spacer units (often organic chains of some type) and mesogenic units (usually attached to the end of the flexible chains). The behaviour of the macromolecular system depends upon the characteristics of these three parts and how they interact. So systems that have short spacer units will generally act as a single macromolecular entity, whereas systems which have a long spacer will tend to act more like the individual mesogenic units they contain (as the mesogens are divorced from the macromolecular system to some extent).

There are a number of different types of liquid crystal dendrimer (see figure 1.8). As with LCPs the mesogens can be attached either terminally (Fig 1.8(a)) or laterally (Fig 1.8(b)). In the case of molecules where mesogens are attached both laterally and terminally it is possible to either create Janus-like compounds (Fig 1.8(c)), so that the molecule has two differing halves, or have an alternating system (Fig 1.8(d)). It is also possible to create functionalised dendrimers where chemically or physically active groups are incorporated into the dendrimer with the aim of creating a self-organising system capable of interacting with other molecules, in a manner reminiscent of proteins (Fig 1.8(f)). The creation of such systems would be a useful

step in the area of nanoscience, with the possibility of "smart" self-organising systems allowing many of the processing and modification steps traditionally needed in the synthesis of large systems to be removed, both speeding synthesis up and making it less expensive. The way the mesogens are attached to the dendrimer will determine the phase behaviour of the molecule. For instance, where the liquid crystals are attached to the dendrimer terminally, the molecules will often tend to prefer to form a smectic phase (see figure 1.9(top)) even though the mesogenic moieties will often prefer to form a nematic phase[21] and the stability of the mesophase formed is often linked to the number of mesogenic units within the molecule.[36] Generally, the greater the number of mesogenic units the greater the stability of the phase. If, however, the liquid crystals are attached to the dendrimer in a lateral manner then nematic phases are often preferred (see figure 1.9(bottom)) and the stability of the phases is not affected by the number of mesogens connected to the dendrimer to any large degree.[37] In many cases the dendrimers form a liquid crystal phase through re-arranging their molecular structure to form some type of shape that will then go on to form a mesophase. So the dendrimers may re-arrange to form a rod-like shape with their mesogens distributed at opposite ends of the molecule, alternatively the dendrimer could form a disc by arranging the mesogens around it in a plane, these structures then pack in the same way low molecular weight oblate and prolate mesogens do. Here the generation of the dendrimer plays an important role on the type of mesophase formed, as higher generation dendrimers will tend to form a disc and pack in a columnar type phase, while the lower generation systems will re-arrange into rods and then form a smectic phase.

1.4 Supramolecular Systems and Self-Assembly

The macromolecular systems outlined above consist of single supermolecules that have covalent bonds connecting a series of different molecular parts together, these systems may then self-organise into mesophases. This is different to the behaviour of supramolecular systems, where molecular units self-assemble to form a supramolecular entity through non-covalent forces, and these supramolecular entities subse-
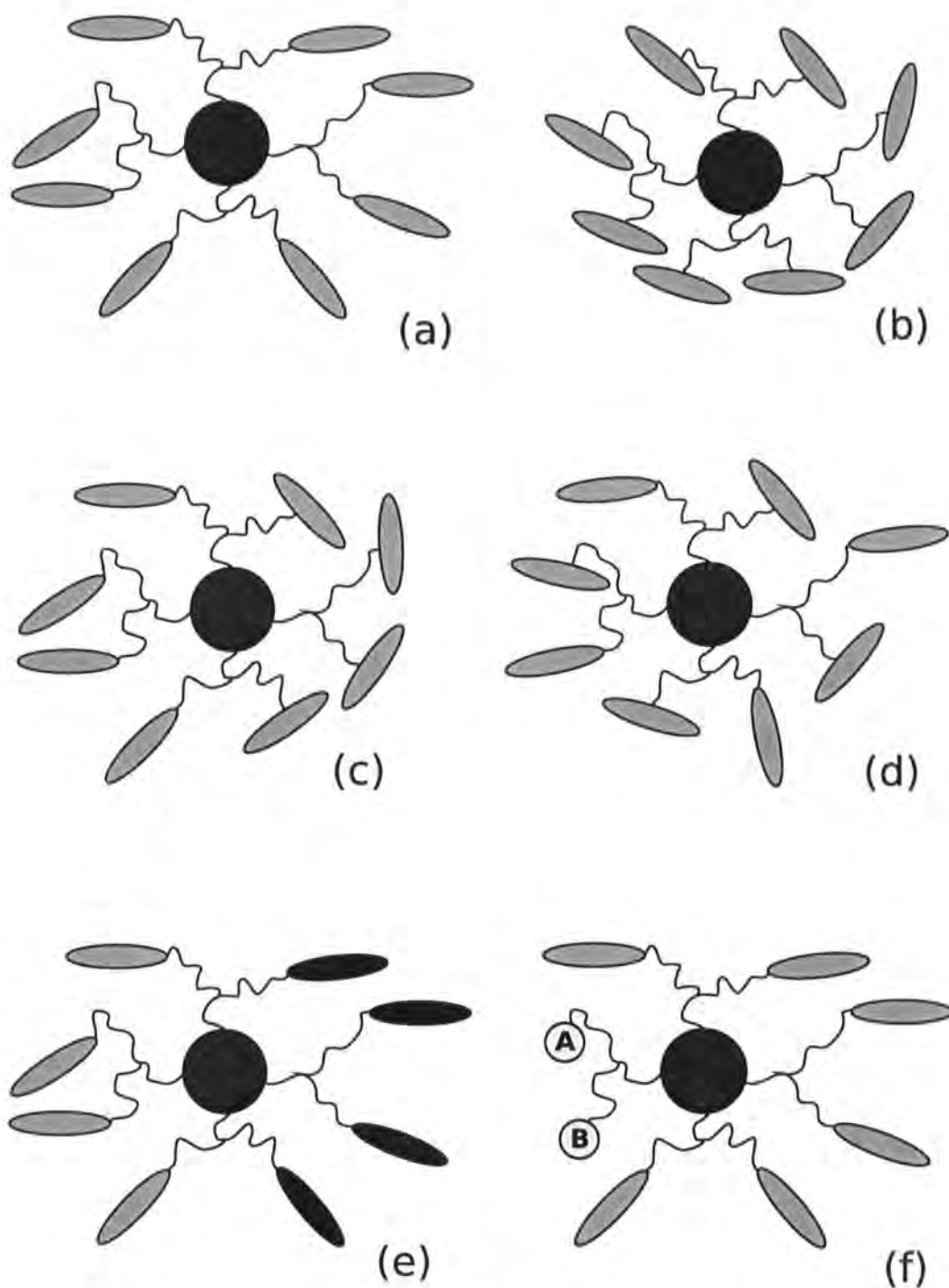
Figure 1.8: Liquid Crystal dendrimers: (a) terminal mesogens units, (b) lateral mesogen units, (c) a Janus type dendrimer, (d) an alternating system, (e) a system with two different types of liquid crystal and (f) a functionalised dendrimer
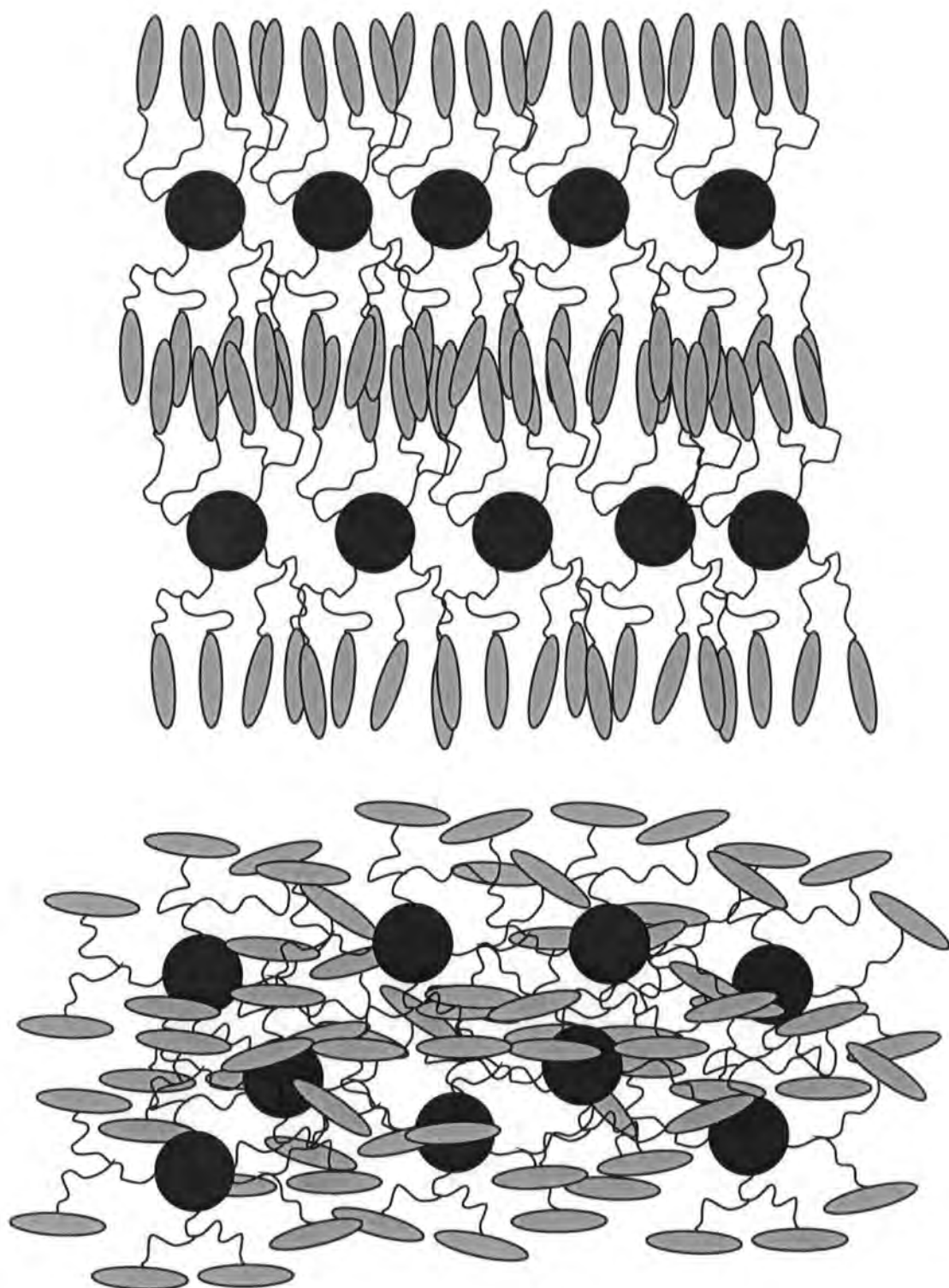
Figure 1.9: Mesophases of liquid crystal dendrimers: (top) smectic-A phase, (bottom) nematic phase.

quently self-organise to form some type of liquid crystal phase. An example of this is shown in figure 1.10, where dendrons pack together to form discs, which then stack on top of each other forming cylinders, which in turn form a hexagonal lattice. Despite these differences supramolecular systems have many of the same potential applications that supermolecular systems do. As with supermolecular systems, controlling molecular structure means that it is possible to control the phase behaviour of the system. One example of this is the work of Percec et al.,[38-41] which has been highly influential in this field. Here the supramolecular entities are assembled from dendrons, those dendrons which have little steric hindrance have a wedge like structure and pack together in columns, but by increasing the steric hindrance of the system (using more bulky tail groups and/or having more tail groups) the dendrons will form a conical shape and then pack together to form a sphere.

While this thesis consists of work done on supermolecular systems, many of the methods used could potentially be used to simulate the behaviour of supramolecular systems.

1.5   Computer Simulation of Liquid Crystal Macromolcules

There are a number of uses of molecular simulation as a tool for studying liquid crystal macromolecules. As with low molecular weight systems, simulation can be used to help elucidate phase behaviour or to provide information about how systems interact. Beyond this, however, one aim of simulation is to help guide synthesis. While liquid crystal macromolecules are extremely interesting molecules they are still very challenging to produce synthetically compared to low molecular weight mesogens. In addition, the large number of different systems that can be constructed from the same building blocks presents synthetic chemists with a difficulty. They cannot make all of the different types of system and so have to make choices about which molecules will give the properties they are looking for. This is were the advantages of computer simulation are apparent. If the different molecular systems could be simulated easily then the molecules with the most promising properties
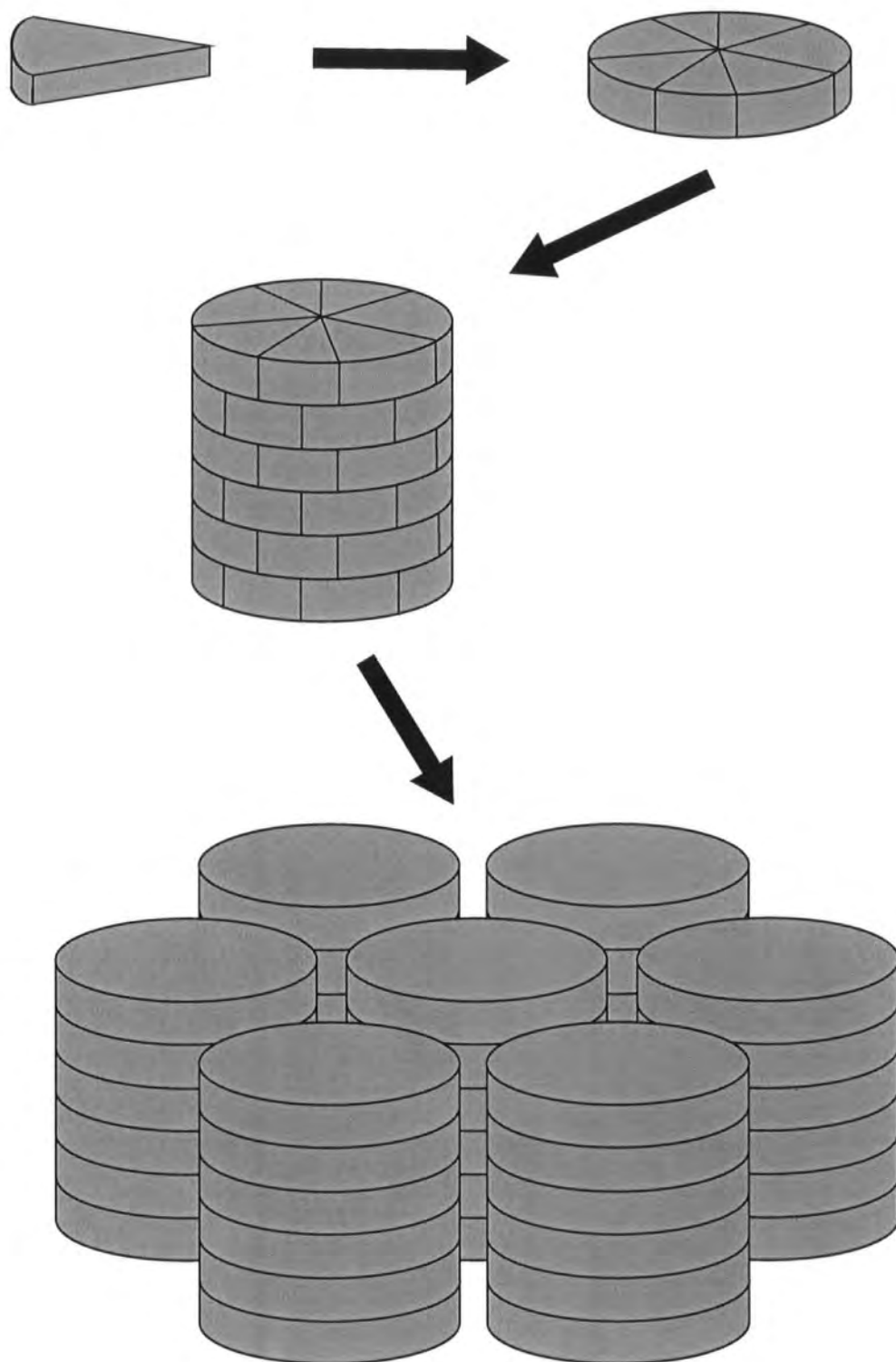
Figure 1.10: A schematic diagram showing how supramolecular structures may be formed from dendron units and how these, in turn, can form a mesophase.

and phases could be identified. Hence the number of systems made synthetically could be reduced.

1.6 Difficulties of Liquid Crystal Macromolecule Simulation

While simulation of macromolecular liquid crystals is highly desirable, the nature of the macromolecules gives rise to a number of factors making simulation difficult. The most obvious problem is the sheer size of the molecules. Even the smallest liquid crystal dendrimer will generally contain thousands of atoms and some of the large polymer systems will dwarf even these. Running a simulation of several hundred or more of these types of molecules is simply too computational demanding to be practical. In addition to the size of the molecules, the length and time scales on which the mesophases of these systems form are much larger than for the low molecular weight liquid crystal systems, increasing the computational demands even further. Therefore new methods that allow macromolecules to be simulated quickly but accurately need to be designed.

Two new simulation methods designed to make progress in this area are described below: they are parallel-tempering (described in chapter 4 of this report) and coarse-graining (described in chapter 3 of this report). Both methods have been tested for liquid crystal dendrimers. Prior to this, chapter 2, contains a brief outline of the computer simulation techniques used and liquid crystal models employed in this report.

1.7 Scope of Thesis

The aim of this thesis is to develop and apply new methods of simulation which will allow macromolecular liquid crystals to be studied more effectively. There are three methods investigated: coarse-grained systems in chapter 3, parallel-tempering in chapter 4 and soft-core potentials in chapters 5 and 6.

Chapter 3 looks at how a macromolecular liquid crystal, in this case a liquid

crystal dendrimer, can be broken down into a number of different sites each containing a number of atoms, thus reducing the number of sites required for simulation. It outlines how this procedures was done so as to reduce computational demands while still maintaining those elements of the molecule that give rise to its properties. Bulk phase simulations of the coarse-grained dendrimer were then carried out and the phase behaviour of the system was observed, which matched both theory and experiment.

Chapter 4 outlines the method known as parallel-tempering (or extended ensembles) and applies it to a variety of cases; a mesogen, an alkyl chain and a liquid crystal dendrimer. Both temperature and potential ensembles are investigated. The benefits and problems of the method are then discussed.

The soft-core models developed in chapter 5 attempt to deal with some of the problems encountered in bulk phase simulation of the LC dendrimer in chapter 3. A number of different types of soft-core potentials are tried out, and tested on liquid crystal systems modelled by spherocylinders. The preliminary results of the expansion of one of these soft-core models to more complex liquid crystal systems are discussed in chapter 6. Where a mesogen with twin alkyl chains attached to each end and a side-chain liquid crystal polymer are modelled using one of the soft-core potentials.

Finally, what conclusions can be drawn from the methods and what improvements can be made are considered in chapter 7. First, however, there is a brief overview of the methods used for the computer simulation of liquid crystals.

Chapter 2

Introduction to Computer Simulation

The formation of liquid crystal phases occur over relatively long time and length-scales meaning that simulations of liquid crystals need to be carried out on relatively large sized systems and for relatively long simulation times (especially for the more ordered phases) in order obtain good results. In addition, as almost all liquid crystals are non-spherical, any model must also take into account the orientational dependence of the intermolecular interactions between molecules, as this is one of the factors which critically determine the behaviour of the system. There are a number of different liquid crystal models[42] including simple lattice models, non-spherical particle models, atomistic models and semi-atomistic or hybrid models. Atomistic, hybrid and soft non-spherical models were used in the simulations carried out in this report. These are described below.

2.1 Liquid Crystal Model Potentials

There are a large number of different potentials used to model liquid crystal phases. The type of model chosen will obviously depend upon the system being simulated and what properties are being investigated. The simplest models include the Lebwohl-Lasher[43,44] lattice model where vectors on a lattice (representing liquid crystal molecules or groups of molecules) are allowed to interact with each other in order to form liquid crystal phases. As the vectors are confined to the lattice there can be no translational motion and the molecular structure of the molecules

is also ignored, thus this model is only used to study very large systems which are not capable of being simulated using more detailed techniques. At the other end of the spectrum we have atomistic potentials where all the atoms in the liquid crystal are represented,[45–48] these models allow the full structure of the liquid crystal to be taken into account by the simulation but have the drawback that they are computationally demanding limiting the number of molecules that can be simulated (<1000). In between are models where each liquid crystal molecule is treated as a single site, these allow a greater number of molecules to be simulated while only taking into the account the gross features of the molecular structure ($\approx$10,000 molecules).

Most potentials used for simulating liquid crystals are pair potentials as including three body terms increases computing time greatly.

2.1.1 Hard Potentials

Systems with hard potentials permit no overlap between molecules, the simplest case is that of hard spheres where the potential, $U(r)$, has the form

$$U(r) = \begin{cases} \infty & r \leq r_0 \\ 0 & r > r_0 \end{cases}, \tag{2.1}$$

where r is the distance between the centre of the two spheres and r_0 is the radius of the spheres. The potential can be used for liquid crystal molecules by replacing the sphere with some type of anisotropic shape: such as a prolate ellipsoid or a spherocylinder[49–51] for calamitic liquid crystals, or a cut-sphere[52] or oblate ellipsoid for discotic mesogens. The potential is purely repulsive and thus the formation of phases is based on excluded volume considerations, meaning that phase behaviour is determined by density and molecular shape rather than by temperature. Despite this liquid crystal phases, which are typical of thermotropic systems (i.e. nematic and smectic-A), will form as predicted by Onsager theory.[53] The I-N phase transition is caused by the competition between the orientational and translational entropy. As the density of the system increases then it becomes favourable to maximise the latter at the expense of the former.
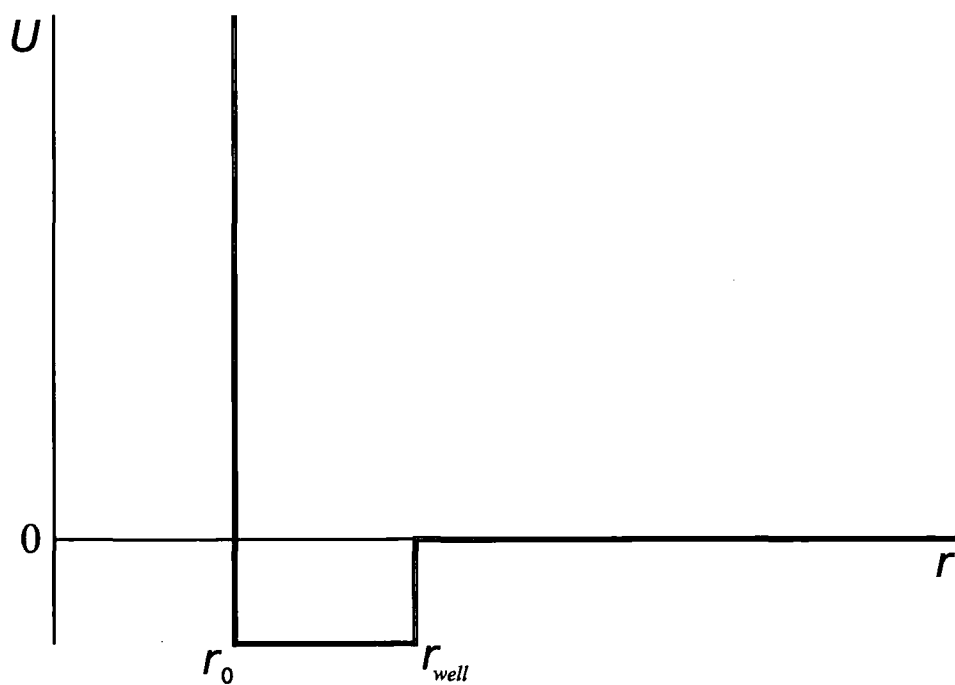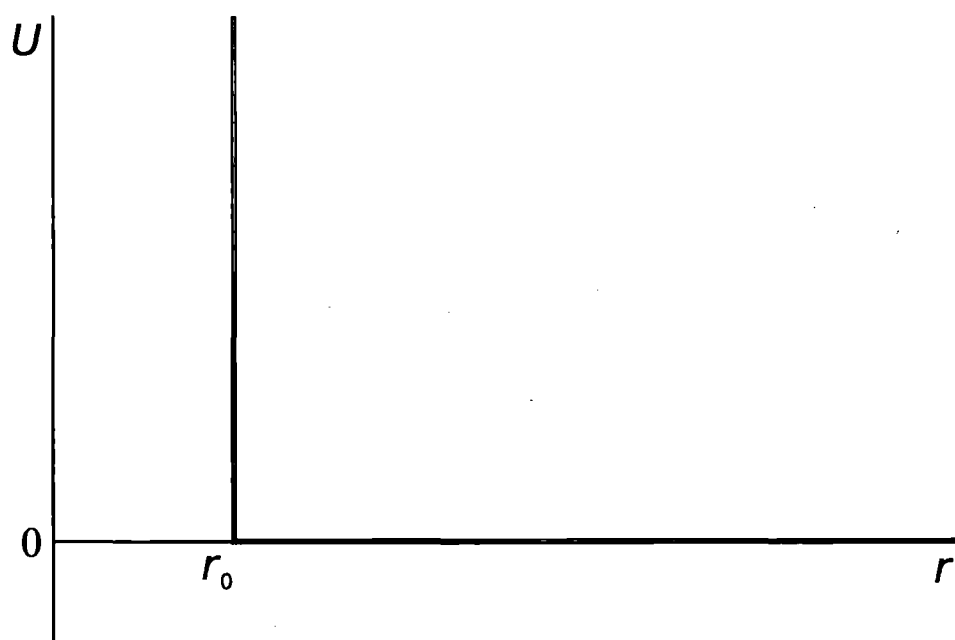
Figure 2.1: Hard Potentials: simple hard wall potential (top) and hard square well potential (bottom).

A simple modification to the hard potential gives the square well potential, $U_{SW}(r)$,[54-56] which has an attractive well placed before the hard wall

$$U_{SW}(r) = \begin{cases} \infty & r \leq r_0 \\ \varepsilon & r_0 < r \leq r_{well} \\ 0 & r > r_{well} \end{cases} \cdot \qquad (2.2)$$

The depth of the well is given by ε and r_{well} is the distance over which the attractive force applies. The main effect of adding this well is to shift the I-N and N-Sm phase boundaries to higher densities.[56]

2.1.2 Soft Potentials

Soft potentials allow molecules to overlap to some degree. There are a number of different forms of soft potential depending upon the nature of the system you are simulating. The potential which is often used for soft spheres is the Lennard-Jones potential which has the form

$$U_{LJ}(r_{ij}) = 4\epsilon_{ij} \left[\left(\frac{\sigma_{ij}}{r_{ij}} \right)^{12} - \left(\frac{\sigma_{ij}}{r_{ij}} \right)^6 \right], \qquad (2.3)$$

where r_{ij} is the distance between the centre of masses of particles i and j, ε_{ij} is the well depth and σ_{ij} the distance between the particles when U is 0. Different values of ε_{ij} and σ_{ij} can be used to model different species.

The Lennard-Jones potential is isotropic and for the simulation of liquid crystal an anisotropic potential is needed. Two of the most common soft potentials for liquid crystals are the soft repulsive spherocylinder (SRS)[56-60] potential and the Gay-Berne (GB) potential[61-63] which is used for ellipsoids. Both consider the whole of the liquid crystal molecule as a single site.

Soft Repulsive Spherocylinder Potential

Spherocylinders are shapes consisting of a cylinder of length L and diameter D capped on each end by a hemi-sphere, also possessing a diameter equal to D (see figure 2.3). The soft repulsive spherocylinder potential, $U_{SRS}(d_{ij})$, is simply a cut
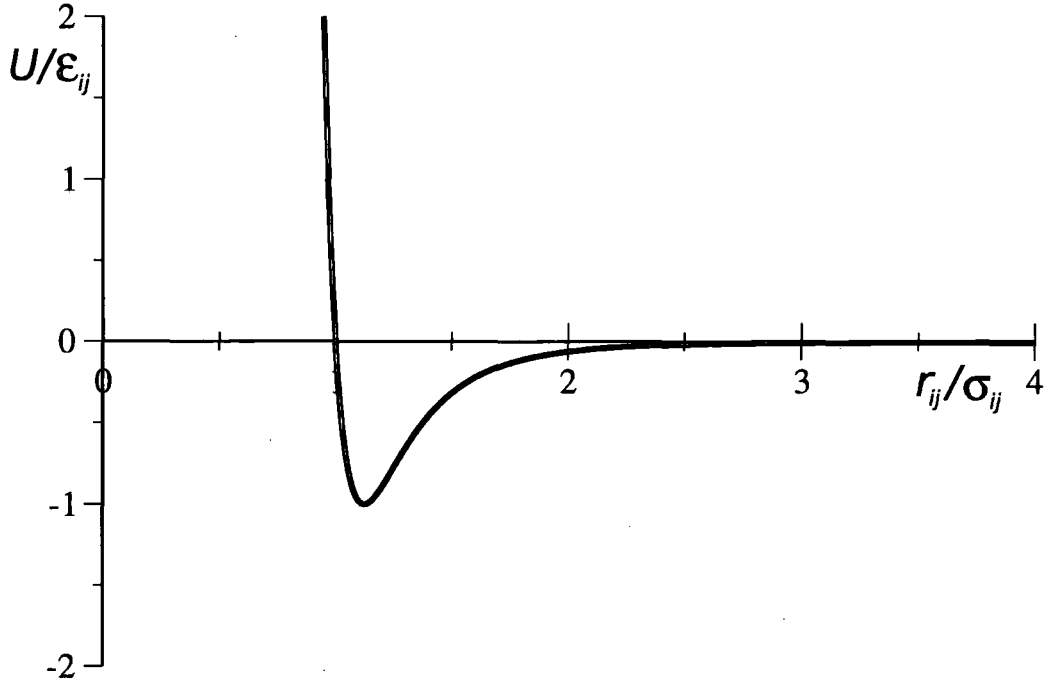
Figure 2.2: Plot of the Lennard-Jones potential.

and shifted version of the Lennard-Jones potential which takes into account the anisotropic shape of the molecule. It has the form

$$
U_{SRS}(d_{ij}) = \begin{cases} 4\epsilon_{ij} \left[\left(\frac{\sigma_0}{d_{ij}}\right)^{12} - \left(\frac{\sigma_0}{d_{ij}}\right)^{6} + \frac{1}{4} \right] & d_{ij} < d_{cut} \\ 0 & d_{ij} \geq d_{cut} \end{cases}, \tag{2.4}
$$

where $\sigma_0 = D$, the diameter of the spherocylinder and d_{ij} is the shortest separation between the long axis of the cylinders. The cutoff value, d_{cut}, is usually set to $2^{\frac{1}{6}}\sigma_0$. The anisotropic form of the potential is shown in figure 2.4. The aspect ratio, L/D, of the spherocylinder determines the phase behaviour of the molecule. The greater the aspect ratio the greater the excluded volume contribution to the entropy will be at any given density, meaning that liquid crystal phases are more likely to form. The SRS potential has been shown to form nematic and smectic liquid crystal phases, also its short ranged nature makes it especially useful in domain decomposition parallelisation techniques (see section 2.2.6 for more details).
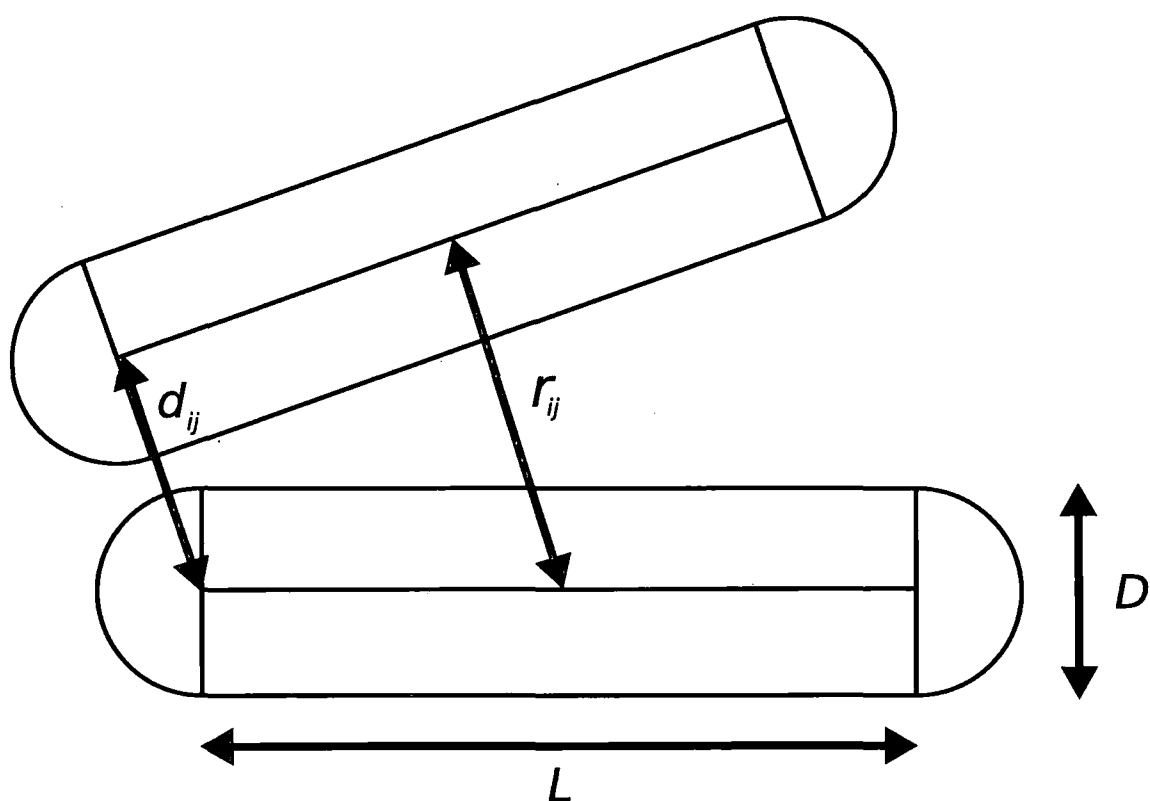
Figure 2.3: Schematic diagram of two spherocylinders, showing the definitions of r_{ij}, d_{ij}, L and D.
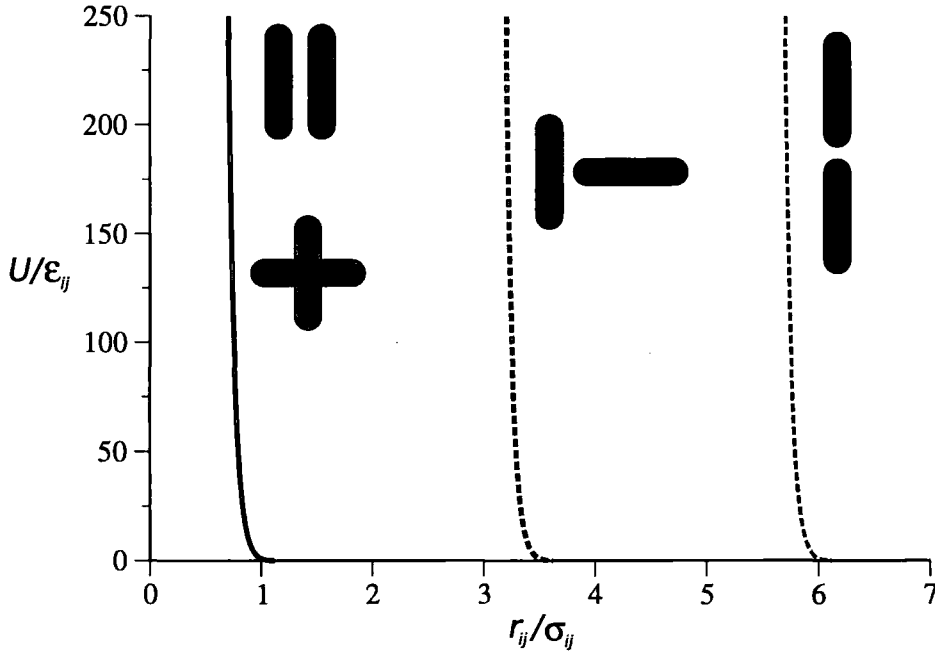
Figure 2.4: SRS potential for a $L/D = 5$ spherocylinder system.

Gay-Berne Potential

The Gay-Berne potential[61] is another soft potential that is widely used. It represents the liquid crystal molecules as ellipsoidal particles, with the precise shape of the molecule being defined by shape anisotropy parameter, χ, which takes the form

$$\chi = \frac{\kappa^2 - 1}{\kappa^2 + 1}, \tag{2.5}$$

where κ is the ratio of the end to end distance to the side to side distance ($\kappa = \sigma_{ee}/\sigma_{ss}$). Therefore $\chi = 0$ means that the particle will be a sphere, $\chi = 1$ the particle an infinitely long rod and $\chi = -1$ an infinitely thin disc. The other parameter which determines the exact form of the potential is the well depth anisotropy parameter, χ', is given by

$$\chi' = \frac{\kappa'^{\frac{1}{\mu}} - 1}{\kappa'^{\frac{1}{\mu}} + 1} \tag{2.6}$$

where $\kappa' = \epsilon_{ss}/\epsilon_{ee}$, ϵ_{ss} and ϵ_{ee} being the well depths when molecules i and j are side to side and end to end respectively. The Gay-Berne potential not only varies with

the intermolecular distance, r, but also orientations of the two particles, $\mathbf{u}_i$ and $\mathbf{u}_j$ (see figures 2.5 and 2.6). The Gay-Berne potential between two particles i and j takes the form,

$$U_{ij}(\mathbf{r}_{ij}, \mathbf{u}_i, \mathbf{u}_j) = 4\epsilon_{ij}(\mathbf{r}_{ij}, \mathbf{u}_i, \mathbf{u}_j) \left[\left(\frac{\sigma_0}{r - \sigma(\mathbf{r}_{ij}, \mathbf{u}_i, \mathbf{u}_j) + \sigma_0} \right)^{12} - \left(\frac{\sigma_0}{r - \sigma(\mathbf{r}_{ij}, \mathbf{u}_i, \mathbf{u}_j) + \sigma_0} \right)^6 \right],$$

$$(2.7)$$

where $\epsilon_{ij}(\mathbf{r}_{ij}, \mathbf{u}_i, \mathbf{u}_j)$ is the orientationally dependant well depth and is given by

$$\epsilon_{ij}(\mathbf{r}_{ij}, \mathbf{u}_i, \mathbf{u}_j) = \epsilon_0 \epsilon^{GB}(\mathbf{u}_i.\mathbf{u}_j)^{\nu} \epsilon'^{GB}(\mathbf{r}_{ij}, \mathbf{u}_i, \mathbf{u}_j)^{\mu}, \qquad (2.8)$$

consisting of

$$\epsilon^{GB}(\mathbf{u}_i.\mathbf{u}_j) = [1 - \chi^2(\mathbf{u}_i.\mathbf{u}_j)^2]^{-\frac{1}{2}}, \qquad (2.9)$$

and

$$\epsilon'^{GB}(\mathbf{r}_{ij}, \mathbf{u}_i, \mathbf{u}_j) = \left[1 - \chi' \left(\frac{(\mathbf{r}_{ij}.\mathbf{u}_i)^2 + (\mathbf{r}_{ij}.\mathbf{u}_j)^2 - 2\chi'(\mathbf{r}_{ij}.\mathbf{u}_i)(\mathbf{r}_{ij}.\mathbf{u}_j)(\mathbf{u}_i.\mathbf{u}_j)}{1 - \chi'^2(\mathbf{u}_i.\mathbf{u}_j)^2} \right) \right].$$

$$(2.10)$$

The orientationally dependant contact distance $\sigma(\mathbf{r}_{ij}, \mathbf{u}_i, \mathbf{u}_j)$ depends upon the shape of the molecule,

$$\sigma(\mathbf{r}_{ij}, \mathbf{u}_i, \mathbf{u}_j) = \sigma_0 \left[1 - \chi \left(\frac{(\mathbf{r}_{ij}.\mathbf{u}_i)^2 + (\mathbf{r}_{ij}.\mathbf{u}_j)^2 - 2\chi(\mathbf{r}_{ij}.\mathbf{u}_i)(\mathbf{r}_{ij}.\mathbf{u}_j)(\mathbf{u}_i.\mathbf{u}_j)}{1 - \chi^2(\mathbf{u}_i.\mathbf{u}_j)^2} \right) \right]^{-\frac{1}{2}},$$

$$(2.11)$$

σ_0 and ϵ_0 are simply scaling constants. The form of the Gay-Berne potential can be varied by altering the parameters κ, κ', μ and ν. Different sets of values for these parameters have been studied,[63-65] as have systems comprising of discotic Gay-Berne particles,[66] chiral GB particles[67] and other modified GB models.[68-71]

2.2   Simulation Methods

There are a number of different methods that can be used in the simulation of liquid crystals, and the choice of which method to use will depend upon a number of factors, particularly the size of the system and the properties of interest of the system. For
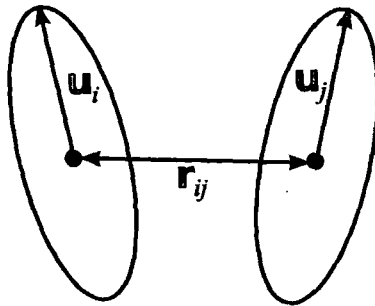
Figure 2.5: Diagram showing the definitions of the intermolecular distance, $\mathbf{r}_{ij}$, and the two orientational vectors, $\mathbf{u}_i$ and $\mathbf{u}_j$, for two Gay-Berne particles.
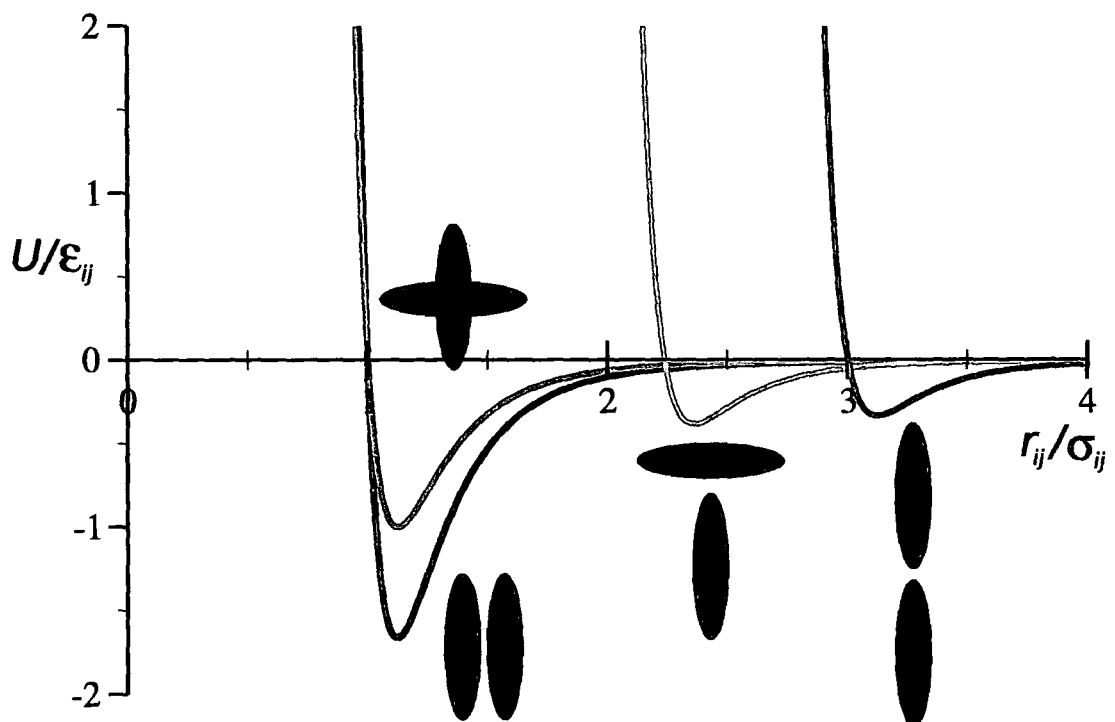
Figure 2.6: Diagram showing the Gay-Berne potential for different particle alignments. The parameters of the potential are $\mu = 2$, $\nu = 1$, $\kappa = 3$ and $\kappa' = 5$.

the simulation to give accurate data then it is vital that different configurations of the system are explored (i.e. that the *phase space* of the system is properly sampled). For small systems molecular mechanics (MM) can be used, for large systems then molecular dynamics (MD) and/or Monte Carlo (MC) will need to be used.

2.2.1   Molecular Mechanics

Molecular Mechanics (MM)[72,73] is one of the simplest computational techniques which can be used to obtain data about molecules. It works by calculating the energy of different conformers of the molecule in question meaning that such things as the global minima conformation, the profile of dihedral angles or the heat of formation[74-76] can be obtained.

Molecular mechanics works by calculating the energy of a conformation from a force field (see below) and minimising the energy of the system to find the lowest energy conformation. While this process is quite easy for simple systems where the number of conformations is not too large (meaning the global energy minima can be found easily) for large systems there can be thousands, if not millions of different conformations. The calculations will not only take a long time but it is difficult to know if all the conformations have been found, meaning that the potential energy minima found may not include the global minimum. When the system is able to exhibit many configurations molecular mechanics becomes impractical. Here a better approach is to employ Monte Carlo (MC) or molecular dynamics (MD) simulation techniques (see sections 2.2.2 and 2.2.3) which find the sample the potential energy surface rather than simply finding the minimum potential energy.

Force Fields

The energy of any molecular conformation is determined from a force field, this is true not only of molecular mechanics but also in Monte Carlo and molecular dynamics simulations. In a force field a molecule is represented as a collection of connected sites coupled to each by a number of different (classical) potentials. In molecular mechanics calculations the sites will usually be the atoms the molecule is made up of but for large systems an united atom (UA) model may be used. Here the

hydrogens are combined with the atom they are attached to, forming a single site, if the molecule is very large this coarse-graining process can be expanded further as discussed in section 2.3.

The exact nature of the force field and the terms within it can vary. Force fields are often built with a specific purpose or area of focus in mind, for instance the AMBER[77,78] or OPLS[79,80] force fields are designed for bulk phase simulations while the MM2,[81] MM3[82] and MM4[83,84] force fields, designed by Allinger and co-workers, are used for the simulation of small organic molecules.

The force field used for the work presented in this report was based on the OPLS-AA[85] force field, which breaks the energy down into five different terms; bond-stretching, E_{bond}; angle bending, E_{angle}; dihedral angle rotations, $E_{dihedral}$; electrostatic interactions, $E_{electrostatic}$; and the energy arising from Van der Waals interactions, E_{VdW}. It takes the form

$$E_{Total} = \sum_{bonds} E_{bond} + \sum_{angles} E_{angle} + \sum_{dihedrals} E_{dihedral} + \sum_{pairs} E_{electrostatic} + \sum_{pairs} E_{VdW},$$

(2.12)

where the individual components of the force field have the functional forms given below. The bonding term for each bond in the molecule is given by

$$E_{bond} = \frac{1}{2} k_{bond} \left(r - r_0 \right)^2,$$

(2.13)

where k_{bond} is the force constant of the bond, r is the bond length and r_0 is the equilibrium bond length. The angle bending term is likewise described using a harmonic potential

$$E_{angle} = \frac{1}{2} k_{angle} \left(\theta - \theta_0 \right)^2,$$

(2.14)

where k_{angle} is the force constant of the bond angle, θ is the bond angle and θ_0 is the equilibrium angle. For dihedral angles a Fourier series expansion is used

$$E_{dihedrals} = \sum_{m} \frac{V_m}{2} \left(1 + \cos \left(m\phi - \delta_m \right) \right).$$

(2.15)

Here, V_m are the torsional force constants, ϕ the torsional angle and δ_m the phase angle which will either be $0°$, when m is odd, or $180°$, when m is even. The number of terms used in the expansion can vary but for the work in this report was never less than three.

The electrostatic interactions are modelled using the Coulomb potential

$$E_{electrostatics} = \frac{q_i q_j}{4\pi\epsilon_0 r_{ij}}, \qquad (2.16)$$

where q_i and q_j are the atomic charges, r_{ij} the distance between the two atoms and ϵ_0 the permittivity of free space. Van der Waal forces between two particles are modelled using the Lennard-Jones potential (Eqn.2.3). The electrostatic and Van der Waal interactions are not calculated for those atoms which are bonded together or share a bond angle (1-2 and 1-3 interactions respectively), 1-4 interactions (those atoms that are connected by a dihedral) are scaled. Usually the scaling factor is an eighth for the electrostatic interactions, and a half for the Van der Waal interactions.

Other force fields may have extra terms, for instance the MM3 also has stretch-bend, stretch-torsion and bend-bend interactions in addition to the above terms and the MM4 introduces even more terms. The large number of terms means that these force fields allow accurate predictions of molecular structures but limit them to being used with relatively small systems, whereas the simpler nature of the OPLS/AMBER force fields mean that large structures can be modelled.

2.2.2   Monte Carlo

As mentioned above it is vital that the conformations of a system are sampled correctly, something that becomes increasingly difficult to do using molecular mechanics as the system increases in size. Monte Carlo simulations are one of the methods used to solve this problem. In statistical mechanics it is possible to measure the average value of a property, A, from the expression

$$\langle A \rangle = \frac{\int A(\mathbf{r}) \exp\left[\frac{-E(\mathbf{r})}{k_B T}\right] d(\mathbf{r})}{\int \exp\left[\frac{-E(\mathbf{r})}{k_B T}\right] d(\mathbf{r})}, \qquad (2.17)$$

where k_B is the Boltzmann constant, T the temperature, $A(\mathbf{r})$ the value of the property measured in configuration $\mathbf{r}$ and $E(\mathbf{r})$ the internal energy of that configuration. The integrals cannot be calculated analytically, but by calculating the energy of the system in different conformations the integrals can be estimated and $\langle A \rangle$ calculated. This task can be achieved in a Monte Carlo simulation. The main difficulty here is ensuring that the phase space of the system is sampled correctly. If the configurations are simply selected at random then conformations that are physically very unlikely (conformations with a high energy, those having a Boltzmann factor, $\exp\left(\frac{-E(\mathbf{r})}{k_B T}\right)$, of approximately zero) would be selected as often as those conformers which are much more likely to occur (those with a low energy). The solution to this problem is to use Metropolis Monte Carlo[86] which biases the sampling to ensure that phase space is sampled correctly.

Metropolis Monte Carlo

In Metropolis Monte Carlo[86] the configurations are sampled from a Boltzmann distribution meaning that the low energy conformations that are the most realistic are sampled more often than high energy, physically unlikely, conformations.

Metropolis Monte Carlo works by taking an initial configuration (with an internal energy, E_{old}) of a randomly chosen particle and making random changes in the degrees of freedom of that molecule. Thus for a rigid body molecule there is a translation of the centre of mass, δr, followed by a rotation about the centre of mass, $\delta \Theta$. For flexible systems there are more degrees of freedom and the Monte Carlo move will now consist of a random change to a random dihedral angle, $\delta \phi$, bond angle, $\delta \theta$, and bond length, δl, in the molecule as well as a centre of mass displacement and a rotation about the centre of mass. The random change in each of the degrees of freedom is capped at a maximum value and minimum value, so for the translational degree of freedom, $-\delta r_{max} < \delta r < +\delta r_{max}$. Once the Monte Carlo move is made the energy of the new conformation, E_{new}, is calculated. The move is accepted, and the new conformation used as the next starting point, if either $E_{old} > E_{new}$ or

$$\zeta \leq \exp\left(\frac{-(E_{new} - E_{old})}{k_B T}\right), \tag{2.18}$$

where ζ is a random number between 0 and 1. The process is then repeated over and over till the simulation run finishes.

Phase space is explored most efficiently when the number of moves accepted is about 50% of the trial moves. If the acceptance ratio is too large it means that the maximum values of the degrees of freedom are too small and phase space is being explored very slowly as all conformers are very similar. If, however, the acceptance ratio is quite small then most moves are being rejected because the limits are large and the simulation is inefficient. Therefore in the equilibrium stage of a simulation feedback loops are created that alter the value of the maximums so that the acceptance ratio remains around 50%.

The process outlined above is for the canonical ensemble (NVT, constant volume, V, constant temperature, T, and constant number of particles, N) but Monte Carlo can be easily adapted for the isothermal-isobaric ensemble (constant pressure NpT), where the volume of the system is allowed to fluctuate. In the NpT ensemble there are box moves, where the volume of the simulation box[87] is changed, as well as the usual moves described above. The new volume of the box is determined by

$$V_{new} = V_{old} \exp(\delta box), \tag{2.19}$$

where V_{new} and V_{old} are the new and old box volumes respectively and δbox is a random number. Once this trial state has been generated the parameter δH is calculated from

$$\delta H = (E_{new} - E_{old}) + p(V_{new} - V_{old}) - Nk_BT \ln\left(\frac{V_{new}}{V_{old}}\right), \tag{2.20}$$

and the move is accepted if

$$\zeta \leq \min\left(1, \exp\left(\frac{-\delta H}{k_BT}\right)\right). \tag{2.21}$$

In addition to the translational, orientational and intramolecular Monte Carlo moves it is also possible to create other moves, most of which are relatively specific to the system studied. For example in MC polymer simulations it is possible to have

Monte Carlo moves that make or split loops, that break or join polymer chains. Examples are given in the recent work of Theodorou and co-workers.[88-90]

2.2.3 Molecular Dynamics

Molecular dynamics ensures that phase space is sampled correctly by making all the atoms/sites in the system subject to Newtonian laws of motion and then allowing the system to evolve over time. The force on atom/site i, $\mathbf{F}_i$, is given by

$$\mathbf{F}_i(t) = -\nabla_{\mathbf{r}_i} E(\mathbf{r}_i(t)) \qquad (2.22)$$

where $E(\mathbf{r}_i(t))$ is the potential energy of the site at coordinate $\mathbf{r}_i$ at time t. From equation 2.22, Newton's second law of motion

$$m_i \frac{d^2 \mathbf{r}_i}{dt^2} = \mathbf{F}_i(t) \qquad (2.23)$$

where m_i is the mass of atom/site i, can then be solved.

For a system with continuous potentials the motions of the sites in the system interact with each other meaning that a numerical solution must be used. The numerical solution is to use a finite difference method, breaking time down into discrete parts, called timesteps, with length δt. Knowing the positions, velocities and accelerations of the sites at time t we can calculate the positions, velocities and accelerations of the sites at time $t + \delta t$, which in turn allows the force on each site to be recalculated. The process is then repeated with the recalculated forces used to give the positions, velocities and accelerations of the sites at time $t + 2\delta t$, allowing the system to evolve over time. Although the longer the timestep the greater the length of time that can be simulated if the timestep is too large the energy of the system will not be conserved.

Integration Algorithms

The finite difference method uses a integration algorithm to solve equation 2.23. There are a number of different algorithms that it is possible to use.

The Verlet algorithm[91] was one of the first used and is very simple, it is derived by taking a Taylor expansion of the positions at time t

$$\mathbf{r}(t + \delta t) = \mathbf{r}(t) + \mathbf{v}(t)\delta t + \frac{1}{2}\mathbf{a}(t)\delta t^2 + \cdots, \tag{2.24}$$

$$\mathbf{r}(t - \delta t) = \mathbf{r}(t) - \mathbf{v}(t)\delta t + \frac{1}{2}\mathbf{a}(t)\delta t^2 - \cdots, \tag{2.25}$$

which are combined to give

$$\mathbf{r}(t + \delta t) = 2\mathbf{r}(t) - \mathbf{r}(t - \delta t) + \mathbf{a}(t)\delta t^2 + \ldots, \tag{2.26}$$

and if the expression is truncated at the δt^2 term the velocities have the form

$$\mathbf{v}(t) = \frac{\mathbf{r}(t + \delta t) - \mathbf{r}(t - \delta t)}{2\delta t}. \tag{2.27}$$

The main deficiency of the Verlet algorithm is that while the error in the calculation of the coordinates is of the order δt^4 the error in the velocities is of the order δt^2, this means that the energy in long simulations can drift appreciably. These drawbacks have meant that the Verlet algorithm has been replaced with two algorithms based on it.

The leapfrog algorithm takes its name form the fact that it calculates the mid-step $(t + \frac{1}{2}\delta t)$ velocities and then calculates the coordinates from these velocities, meaning that the positions and velocities leapfrog over each other. The mid-step velocities have the form

$$\mathbf{v}(t - \frac{\delta t}{2}) = \frac{\mathbf{r}(t) - \mathbf{r}(t - \delta t)}{\delta t}, \tag{2.28}$$

$$\mathbf{v}(t + \frac{\delta t}{2}) = \frac{\mathbf{r}(t + \delta t) - \mathbf{r}(t)}{\delta t}, \tag{2.29}$$

and from (2.29) the new positions can be found

$$\mathbf{r}(t + \delta t) = \mathbf{r}(t) + \mathbf{v}(t + \frac{\delta t}{2})\delta t, \tag{2.30}$$

which will then give

$$\mathbf{v}(t + \frac{\delta t}{2}) = \mathbf{v}(t - \frac{\delta t}{2}) + \mathbf{a}(t)\delta t. \tag{2.31}$$

The velocities at time t, needed to calculate the kinetic energy simultaneously with the potential energy, are given by

$$\mathbf{v}(t) = \frac{\mathbf{v}(t + \frac{1}{2}\delta t) - \mathbf{v}(t - \frac{1}{2}\delta t)}{2} \tag{2.32}$$

A second algorithm based on the Verlet algorithm is the velocity Verlet[92] algorithm which takes the form

$$\mathbf{r}(t + \delta t) = \mathbf{r}(t) + \mathbf{v}(t)\delta t + \frac{1}{2}\mathbf{a}(t)\delta t^2, \tag{2.33}$$

$$\mathbf{v}(t + \delta t) = \mathbf{v}(t) + \frac{1}{2}[\mathbf{a}(t) + \mathbf{a}(t + \delta t)]\delta t. \tag{2.34}$$

The Velocity verlet algorithm works in practice by first calculating the new positions using equation 2.33, then the velocity at the mid-step point is calculated from

$$\mathbf{v}(t + \frac{\delta t}{2}) = \mathbf{v}(t) + \frac{1}{2}\mathbf{a}(t)\delta t \tag{2.35}$$

using the accelerations at time t. The accelerations at time $t + \delta t$ are then calculated and used to finish calculating the velocity with the expression

$$\mathbf{v}(t + \delta t) = \mathbf{v}(t + \frac{\delta t}{2}) + \frac{1}{2}\mathbf{a}(t + \delta t)\delta t. \tag{2.36}$$

2.2.4 Molecular Dynamics Ensembles

The equations outlined above are based on using MD in the microcanonical ensemble (constant NVE) as the new trajectories are generated with constant energy. However, it is often more useful to carry out simulations using different ensembles, usually either the canonical ensemble (constant NVT) or the isothermal-isobaric ensemble (constant NpT). In order to do this the molecular dynamics equations need to be modified.

Constant Temperature (NVT) Molecular Dynamics

In the canonical ensemble the temperature, which is directly related to the kinetic energy of the system, can be kept constant by scaling the velocities of the particles. This scaling of the velocities is done by applying a thermostat to the system and there are a number of different thermostats that it is possible to use, the choice of which thermostat to use will depend on the system being simulated and what the aim of the simulation is.

The Andersen thermostat[93] keeps the temperature constant by colliding the particles with a heat bath. In simulation terms this is done by replacing the velocities of randomly selected molecules (or the entire system) with a velocity generated from a Maxwell-Boltzmann distribution corresponding to the constant temperature. The frequency that the system collides with a heat bath can be controlled in the simulation.

A second thermostat is the one developed by Berendsen,[94] here the old velocities, $\mathbf{v}$, are rescaled to new velocities, $\mathbf{v}'$, by $\mathbf{v}' = \chi\mathbf{v}$. The rescaling parameter, χ, is given by

$$\chi = \left[1 + \frac{\delta t}{\tau} \left(\frac{T}{T_0} - 1 \right) \right]^{\frac{1}{2}}, \qquad (2.37)$$

where T is the current temperature of the system, T_0 the desired temperature of the system, δt the timestep and τ a time constant. The Berendsen method is very useful in the initial stages of a simulation as it can drive the temperature towards the desired value quite fast. However, it is not as useful a thermostat to use during the equilibration stage of a simulation as it does not sample the canonical ensemble correctly.

The thermostat developed by Nosé works in a similar manner to the Andersen thermostat, in that the constant temperature is maintained by using a heat bath. The difference is that rather than simply replacing the original velocities, energy is allowed to flow between the heat bath and the system. Originally this was controlled by the thermal inertia, Q, which represented the rate of the flow of energy between the heat bath and the system.[95] The thermostat was then simplified by Hoover,[96]

and in the Nosé-Hoover thermostat the equations of motion are

$$\dot{\mathbf{r}}_i = \frac{\mathbf{p}_i}{m_i},$$

(2.38)

$$\dot{\mathbf{p}}_i = \mathbf{f}_i - \xi\mathbf{p}_i,$$

(2.39)

$$\dot{\xi} = \frac{gk_B(T - T_0)}{Q},$$

(2.40)

where ξ is a thermodynamic friction coefficient, g is the number of degrees of freedom the system has and Q is the aforementioned thermal inertia coefficient.

Constant Pressure (NpT) Molecular Dynamics

The pressure of the simulation can be kept constant by allowing the size of the simulation box to change during the simulation run. The simulation box can be set to allow anisotropic changes in the volume, where the shape of the box will change, or can be constrained to give isotropic changes in volume, where the shape of the box will remain constant. Many of the barostats developed for constant pressure molecular dynamics are adapted versions of thermostats developed for constant temperature MD.

The Berendsen barostat[94] maintains the system at constant pressure by coupling the system to a pressure bath. The system is made to obey the equation

$$\dot{P} = \frac{P_0 - P}{\tau_p},$$

(2.41)

where P is the current pressure of the system, P_0 is the desired pressure and τ_P is a time constant. At each time step the volume is scaled by a factor of ξ, meaning that the coordinates are scaled by a factor of $\xi^{\frac{1}{3}}$ ($\mathbf{r}' = \xi^{\frac{1}{3}}\mathbf{r}$) where

$$\xi = 1 - \lambda_T \frac{\delta t}{\tau_P}(P_0 - P),$$

(2.42)

and λ_T is a compressibility factor.

It is also possible to develop barostats based on the Nosé-Hoover thermostat, one example is that proposed by Toxvaerd.[97] Here a friction coefficient ζ is introduced

and the equations of motion become

$$\dot{\mathbf{r}}_i = \frac{\mathbf{p}_i}{m_i V^{\frac{1}{3}}}, \tag{2.43}$$

$$\dot{\mathbf{p}}_i = \mathbf{f}_i - \left(\dot{\zeta} - \xi\right)\dot{\mathbf{p}}_i, \tag{2.44}$$

$$\dot{\zeta} = \frac{\dot{V}}{3V}, \tag{2.45}$$

$$\ddot{\zeta} = \frac{(P - P_0)V}{Nk_BT_0\tau_P}, \tag{2.46}$$

where ξ is given in equation 2.40.

An alternative way of ensuring the pressure stays constant is to use a Monte Carlo box move[87] as described in section 2.2.2. Here one of the thermostats described above would be used and then a trial MC box move would be attempted which would be accepted or rejected as determined by equations 2.20 and 2.21.

2.2.5 Monte Carlo vs Molecular Dynamics

Both Monte Carlo and molecular dynamics have their advantages and disadvantages and the choice of which method to use will depend on the system and properties being studied. For single molecules or gas phase studies Monte Carlo is the preferred option as the high energy barriers of the dihedral angles and the lack of force interactions from other molecules means that molecular dynamics samples the phase space very poorly. For any property that needs to be measured over an objective time frame (e.g. viscosity coefficients) then obviously molecular dynamics must be used as Monte Carlo simulations do not evolve naturally with time. For simulations where there is a varying number of particles (occurring in the grand canonical ensemble, μVT) then Monte Carlo must be used as new Monte Carlo moves that create and remove molecules can be added to the simulation.

For simulations in the liquid phase the choice is less obvious. As collisions between molecules are common in the liquid phase, energy barriers can be crossed more easily and MD simulations will generally have good sampling. While on the other hand the higher density means that a Monte Carlo move can often cause the

overlap of two particles meaning that the number of rejected moves may increase (and/or δr decrease) to such a point that sampling becomes inefficient. However, the unphysical nature of some Monte Carlo moves can act as a counterbalance to this problem, particularly if new Monte Carlo moves, such as those mentioned in section 2.2.2, are added.

2.2.6 Other Considerations

Parallelisation

It is possible to speed up molecular dynamics simulations by carrying out the simulation on a number of different nodes (usually each node will be a single computer processor). This increases the speed of the simulations and allows large systems to be simulated much more effectively. The two most common parallelisation techniques[98-100] are the replicated data (RD) method and the domain decomposition (DD) method.

In the RD method each node runs the program simultaneously and for the most part separately but will have certain operations (the most complicated and time consuming) broken down into pieces and run in parallel over all the nodes. Once each node has completed its part of the parallel calculation that information will be passed to a master computer and the information will be combined to give a global sum. The master computer will then pass the now combined information back to each node and the simulation will continue. This type of parallelisation has a number of drawbacks, because each node will be carrying out the same calculations for some of the time, some of the computing power of the system is being wasted. A second problem is that as the number of processors are increased so is the number of messages that are passed between nodes. Above a certain number of nodes the simulation will begin to slow down due to the increase in communication time outweighing any decrease in calculation time.[98,101] The replicated data method was used in the molecular dynamics calculations described in chapter 6.

A more efficient method of parallelisation is the DD method. Although a drawback is that the method is more complex to implement. In DD method the simula-

tion box is broken down into a number of domains (of the same size) equal to the number of nodes, each domain is then divided into a number of cells. The number of cells is the maximum possible such that each cell is of equal size and that the sides of the cells are larger than the cut-offs of the potential used. Each node can carry out the simulation independently for the particles in the inner cells, it is only for those cells on the edges of a domain where the particles will interact with particles in a different domain that information about the particles needs to be exchanged between nodes. The DD becomes more efficient the shorter the range of the potential as a shorter potential will reduce the size of the cells, which in turn reduces the amount of message passing between nodes. It is this reason why the DD is very effective when used with the SRS potential (section 2.1.2). The simulations described in chapter 3 were carried out using the GBMOLDD[102,103] program which uses the domain decomposition technique.

Periodic Boundary Conditions

As most computer simulations are limited to a few thousand sites at the most then a large number of molecules will be at the edges of the box. These molecules will experience different forces to those in the centre of the box so the simulation cannot represent a proper bulk phase. The solution to this problem is to use periodic boundary conditions. An infinite bulk phase is created by making identical copies of the simulation box extend in all directions as shown in figure 2.8. The movement of a molecule in the "proper" simulation box is copied in all the simulation boxes, so if a molecule moves out of one side an identical molecule will enter on the other side of the box. Essentially the system wraps around on itself. Although periodic boundary conditions do allow a bulk phase to be simulated they can cause some system artifacts for some properties, particularly if the system is small or the property is long range.

Usually the periodic boxes will be cubes or cuboids but if desired can be a range of different shapes such as truncated octahedrons or rhombic dodecahedrons. In addition it is possible to study the behaviour of systems at surfaces by using two dimensional periodic boundary conditions.
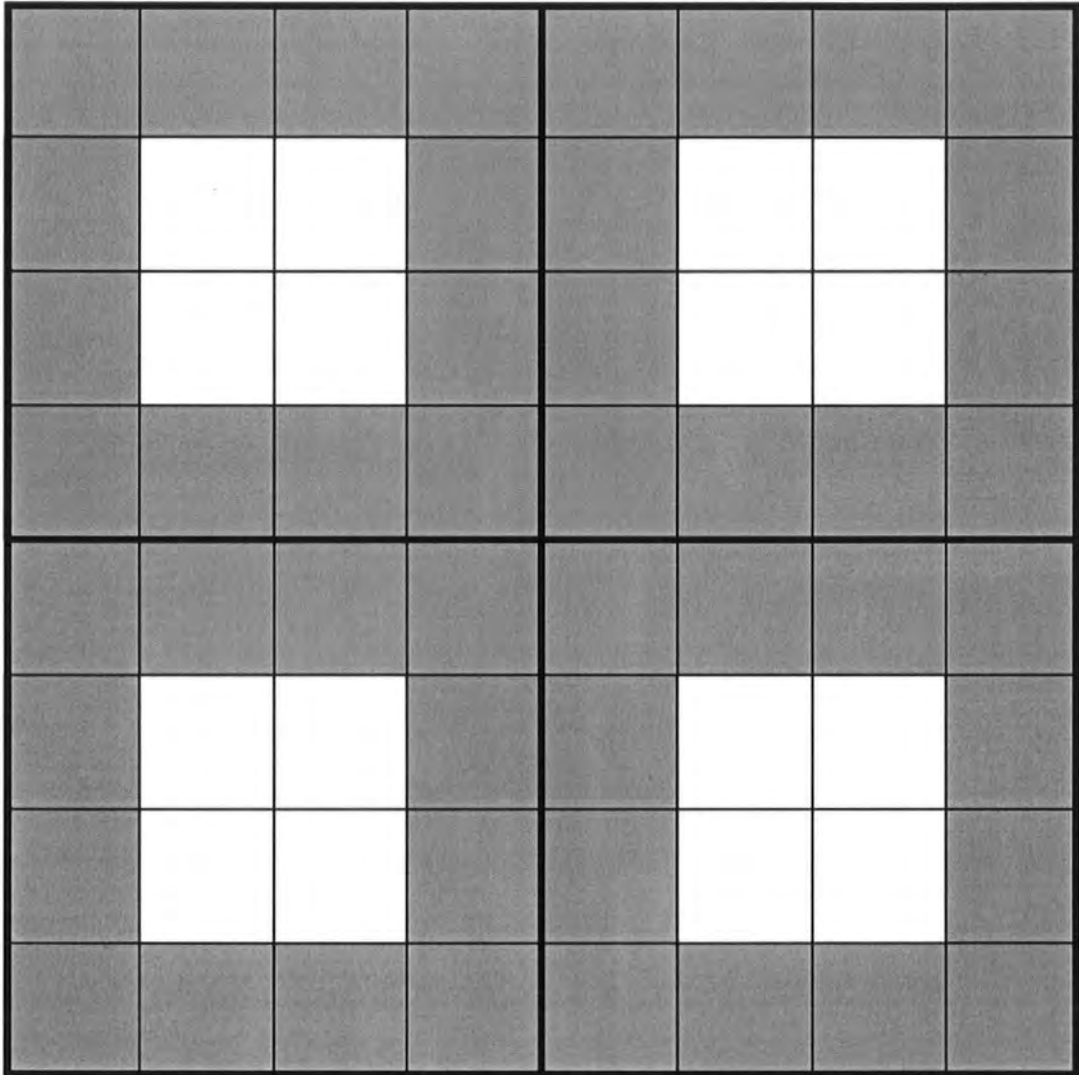
Figure 2.7: A 2 dimensional illustration of the domain decomposition technique, with the system split into four domains. The particles in the light cells do not interact with any particles outside their domain but the particles in the dark cells interact with those in neighbouring dark cells.

The minimum image convention is used in conjunction with periodic boundary conditions. If the cut-off distance of the potential is less than half a box length then only the interactions between a molecule and the nearest images of its neighbouring atoms need to be considered.
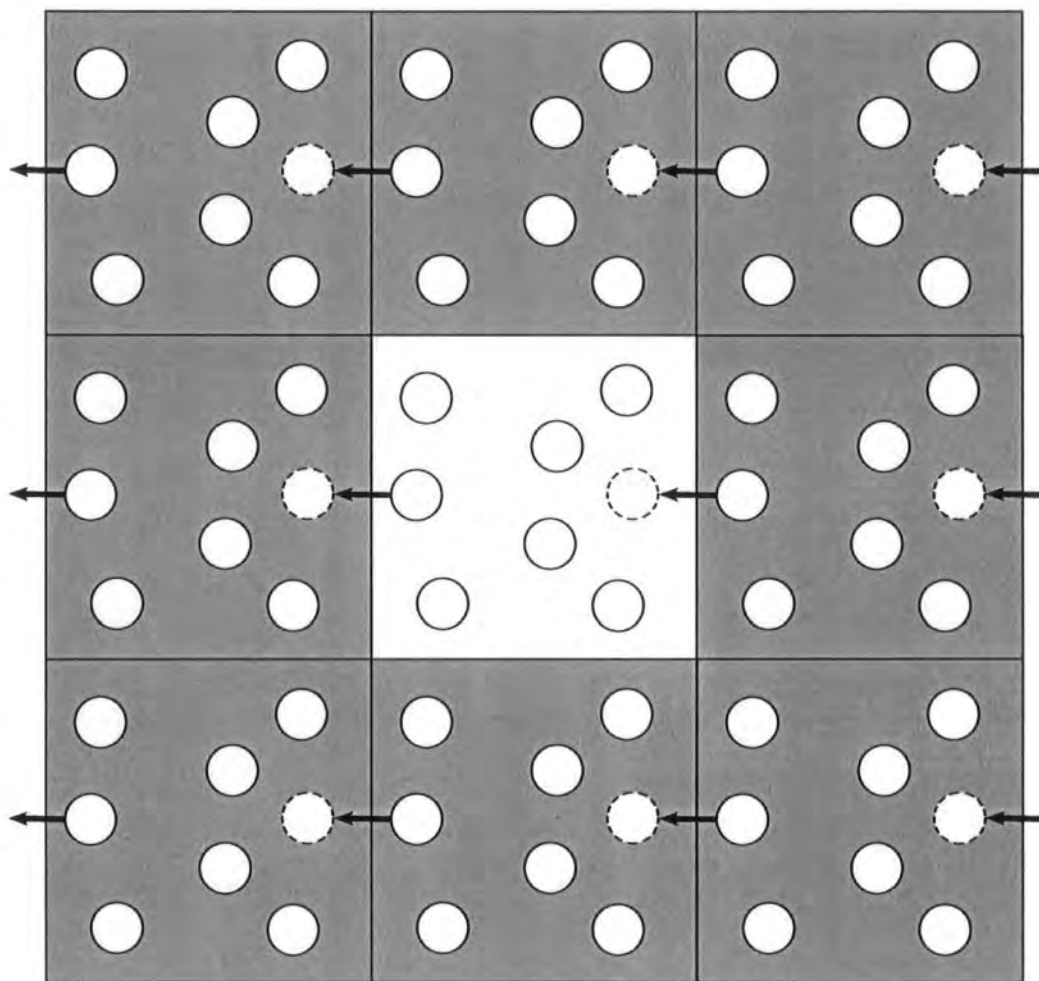
Figure 2.8: A 2 dimensional illustration of periodic boundary conditions.

2.3 Coarse-Grained Models

If systems are modelled atomistically then the number of molecules that can be simulated is limited, and obviously as the size of the molecules increases the number of molecules that can be simulated decreases. This makes the simulation of macro-
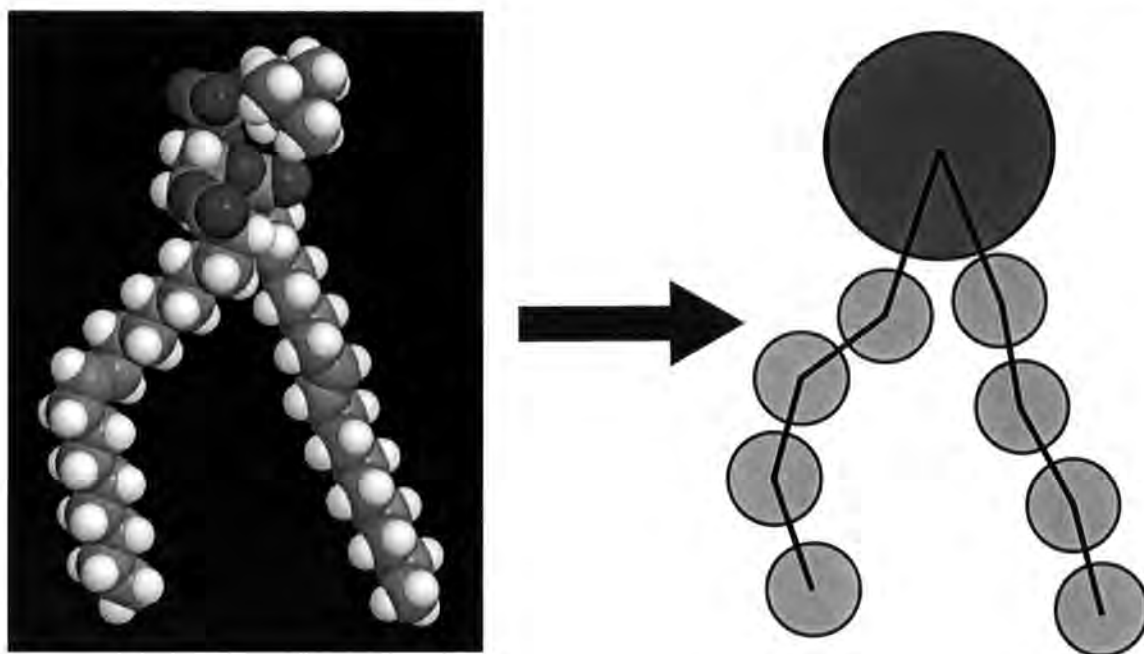
Figure 2.9: Phosphatidylcholine: a fully atomistic model (left) and a coarse-grained model (right).

molecules very difficult. One method that can be used to facilitate the bulk phase simulation of large molecules is coarse-graining. By coarse-graining the atomistic molecule into a series of sites, each consisting of a number of atoms, the number of sites in a molecule can be reduced meaning that the number of molecules simulated in the system can be increased. Coarse-graining is therefore really nothing more than an extension of the united atom model or single site potentials which are already used to model liquid crystals. The scale of coarse-graining will vary depending upon the system being simulated. At the lower end of the scale there are semi-atomistic models. Here a liquid crystal macromolecule could be coarse-grained so that a united atom model was used for the organic backbone while the mesogenic units were replaced with Gay-Berne molecules. The upper end of the coarse-graining spectrum consists of effective pair potentials where thousands of atoms will be represented by a single site. Techniques such as dissipative particle dynamics[104–109] (DPD) lie between these two extremes.

Whatever the scale of the coarse-graining all coarse-grained models must replicate the characteristic features of the atomistic molecules they are supposed to rep-

resent if they are to give the correct phase behaviour (and other physical behaviour) of the molecule. For example, phospholipids generally consist of a hydrophilic head which has two organic tails bonded to it. Figure 2.9 shows a coarse-grained model of the phospholipid phosphatidylcholine. Here the hydrophilic head group is represented by a large spherical site, while the flexible carbon tails are represented by a series of smaller spheres bonded together.

Coarse-grained models can have force fields in just the same way as an atomistic model, with the model having bond stretching, bond bending and dihedral angle terms as well as non-bonded interactions between sites.

2.4 Analysis of Data

2.4.1 Radial Distribution Functions

Radial distribution functions allow the phases of a system to be characterised. For liquid crystals, where phase behaviour can sometimes be quite subtle, the radial distribution functions can be very useful. The pair distribution function, $g(r)$, gives the probability of there being a separation distance of $|\mathbf{r}|$ between a pair of atoms and is measured relative to the probability at the same distance in an ideal gas of the same density.

$$g(r) = \frac{V}{N^2} \left\langle \sum_i \sum_{j \neq i} \delta \left(\mathbf{r} - \mathbf{r}_{ij} \right) \right\rangle, \qquad (2.47)$$

where V is the volume of the system, N the number of molecules in the system and $\mathbf{r}_{ij}$ is the intermolecular vector between atoms i and j.

For liquid crystals it is possible to calculate the radial distribution functions parallel, $g_\parallel(r)$, and perpendicular, $g_\perp(r)$, to the director. Smectic phases have periodic peaks in $g_\parallel(r)$ which can help in identifying a nematic-smectic transition, while $g_\perp(r)$ can provide information about the ordering within layers.
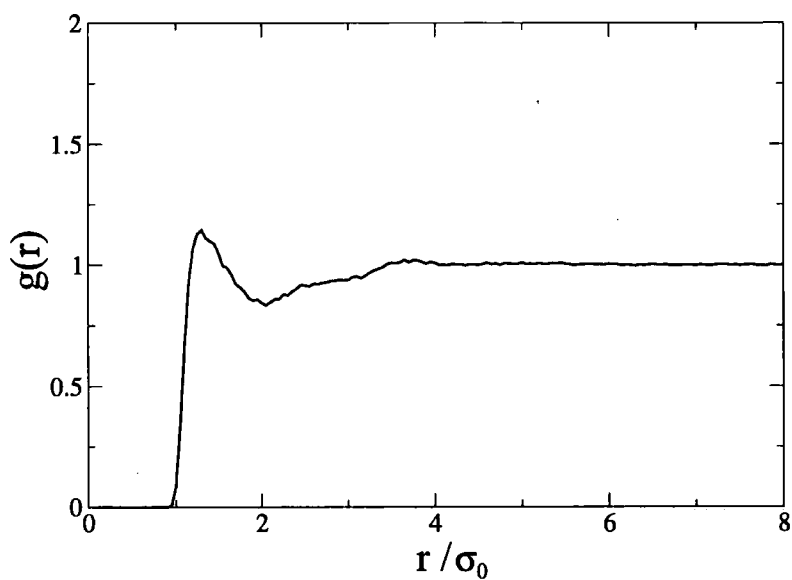
Figure 2.10: A example of the radial distribution function of a liquid crystal system in the isotropic phase.

Chapter 3

Coarse-grained Simulation Studies of a Liquid Crystal Dendrimer

3.1 Introduction

As described in section 2.3 coarse-grained simulations are a method which allows large macromolecular systems to be simulated in the bulk. This chapter describes the simulation of a coarse-grained liquid crystal dendrimer and analyses the structure of the phases formed. The coarse-grained model was based on a third generation carbosilane LCDr[14,15] shown in figure 3.1. This model was chosen as recent synthetic and X-ray diffraction studies of carbosilane LCDrs[14,15] have given important information about the phase behaviour of this family of dendrimers. For this group of molecules the mesophase behaviour is strongly influenced by the generation of the dendrimer. In the isotropic phase the molecules assume a roughly spherical shape. However, this must change for mesophases to form. For the lower generation systems, the dendrimers are believed to rearrange themselves into rods and this leads to the formation of smectic phases characterised in X-ray measurements by a layer spacing. For generation five, which has a higher density of mesogens on the surface of the macromolecule, the dendrimers can also form a columnar phase. Here it is likely that conformational changes can lead to the dendrimer rearranging its structure in a second way to form discs, which can stack to form columns, which in turn pack to form columnar phases. Figure 3.2[110] shows the phase behaviour of this type

of system.

Unlike simpler macromolecules, such as linear homopolymers (which can be coarse-grained by designing a suitable model for a single monomer unit) a CG model of the dendrimer must account for a range of different interaction sites. Moreover, it must be able to represent a complicated molecular shape, which can change structure through conformational rearrangement, yet be sufficiently "cheap" to simulate a relatively large numbers of molecules over long simulation times.

3.2 Construction of the Coarse-grained Model

Any coarse-grained model must describe accurately the most important features of the molecule it is to represent. For the model used in this study the data to build it was taken from a series of more detailed molecular simulations. Previously both atomistic Monte Carlo simulations and semi-atomistic[111] simulations of the molecule in a liquid crystal solvent had already been carried out. In the semi-atomistic simulations the dendrimer backbone was modelled using a united atom model and the mesogenic units on the dendrimer and liquid crystal solvent were represented by Gay-Berne particles. The system was simulated in the mesogenic solvent in the isotropic, nematic and smectic-A liquid phases, the results showed that the dendrimer structure interacts strongly with its molecular environment. In the isotropic solvent, the dendrimer itself forms an isotropic sphere with the mesogenic groups randomly arranged on the periphery. In the nematic solvent, the dendrimer rearranges its molecular structure, so that the mesogenic groups can lie, on average, parallel to the nematic director with an average order parameter approaching that of the solvent (see figure 3.3). In the smectic solvent, the dendrimer rearranges further, so that mesogens can lie commensurate with the smectic layers. In addition it was found that the inner layers of the dendrimer were not penetrated by the liquid crystal solvent, only the mesogenic groups and the linker chains were solvated.

The MC simulations of a single fully atomistic dendrimer molecule were carried out in the gas phase. After energy minimisation and equilibration, production run lengths of approximately 20×10^6 MC steps were carried at 400 K to obtain structural

$$X = -(CH_2)_3Si(CH_3)_2OSi((CH)_3)_2 - (CH_2)\overline{_{10}}CO \cdot O - \langle\langle\rangle\rangle - \langle\langle\rangle\rangle - \equiv N$$
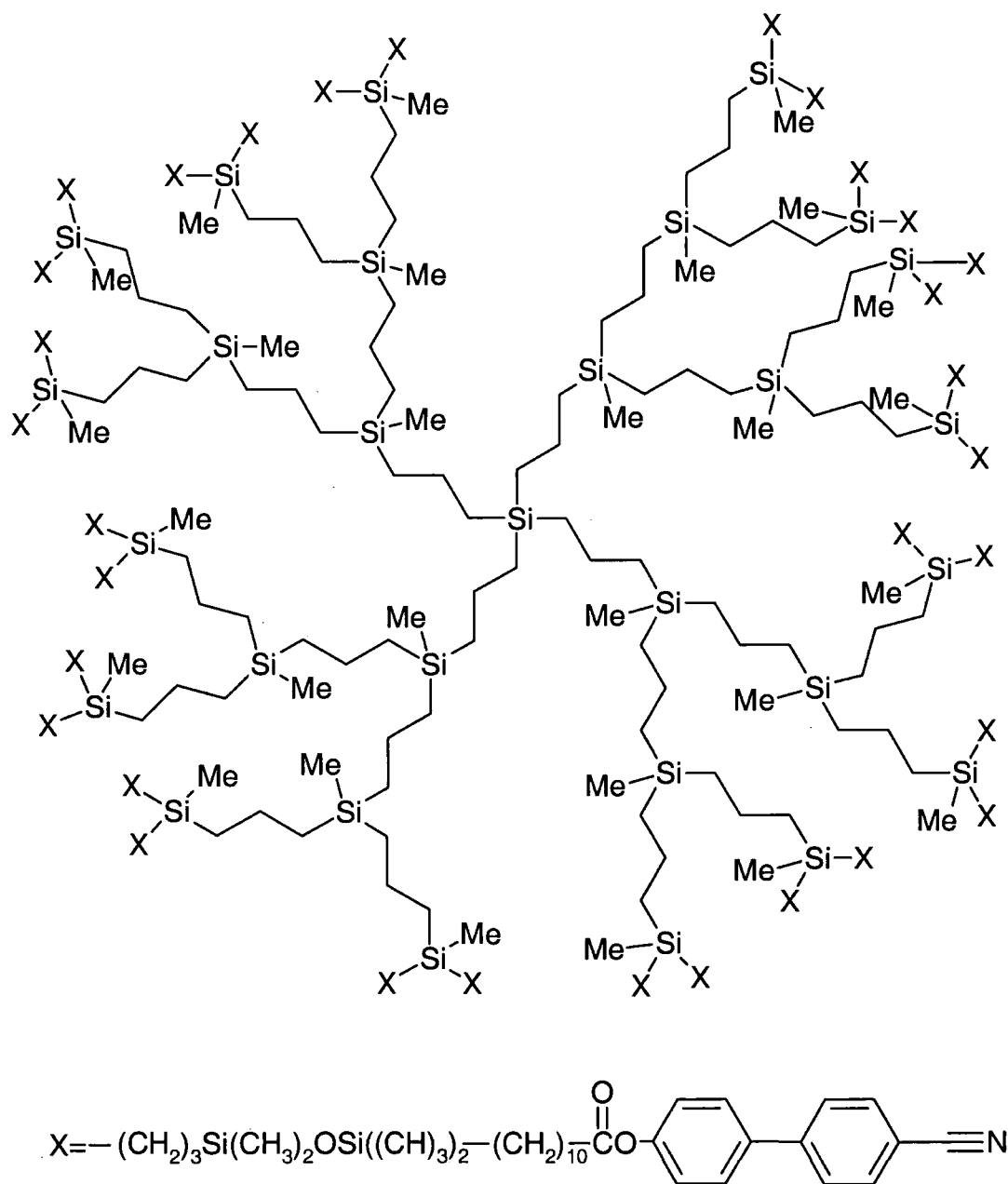
Figure 3.1: Chemical structure of the coarse-grained third generation carbosilane dendrimer.
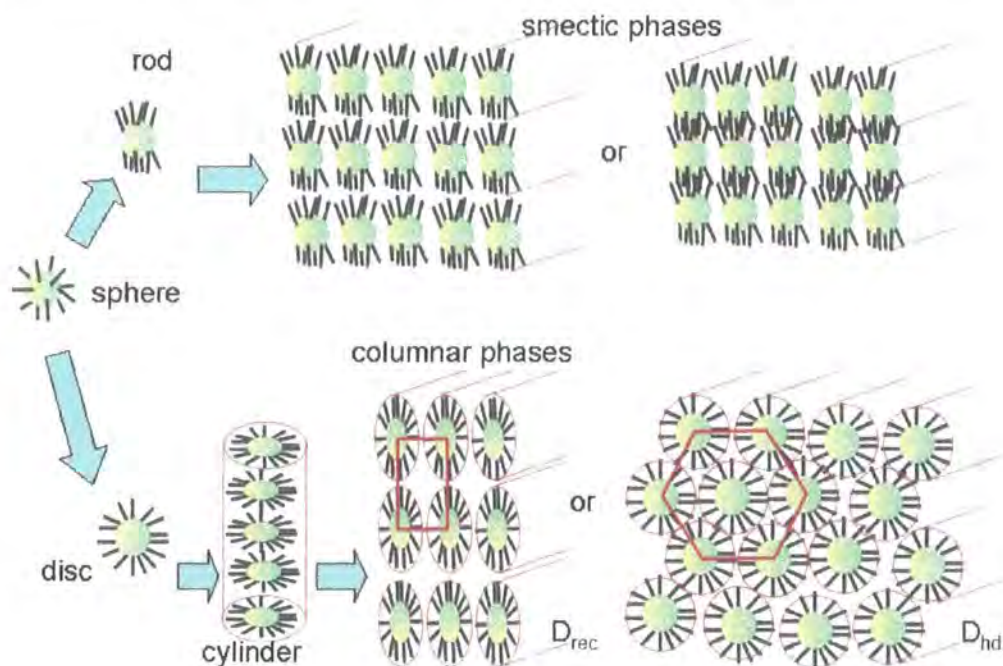
Figure 3.2: Schematic diagram showing how the carbosilane dendrimer can form liquid crystal phases (taken from ref 110).

information for a dendrimer molecule in the gas phase. From these more detailed simulations several observations can be made about the molecule:

- the inner dendritic core (from the central Si atom out to the third generation branching Si atom) forms a fairly rigid scaffold, which is approximately spherical in shape and is largely decoupled from the outer parts of the molecule. The degree of penetration of the outer parts of the molecule (and solvent) into the spaces within this inner core is small.

- the flexible chains (from the third generation branching Si to the mesogenic units) exhibit considerable conformational freedom allowing the molecule to react to its environment and change its shape.

- in the gas phase the dendrimer is, on average, spherical in structure but conformational changes can lead to fluctuations in which the overall dendrimer is instantaneously prolate or oblate in shape. In a solvent the molecule tends to elongate along one direction and form a "rod-like" shape.
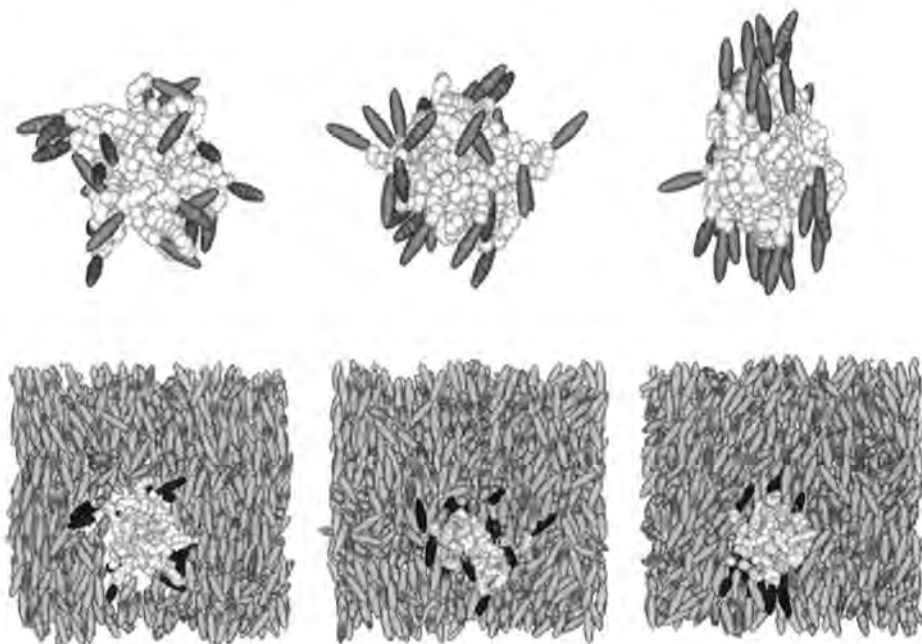
Figure 3.3: Snapshots of the semi-atomistic dendrimer model in a nematic solvent, showing how the dendrimer aligns with the solvent (taken from ref 111).

- in the gas phase there is no ordering of the terminal mesogenic units and the mesogens are able to sample all directions in response to changes in conformation of the flexible chains. However, application of a small ordering potential, $U_{ext} = -\epsilon_{ext} P_2 (\cos \theta)$, of strength $\epsilon_{ext} = 10$ kJ mol^{-1} coupling the C$\equiv$N bond axes to a mean field director leads to an average order parameter of $\langle S_2 \rangle \approx 0.55$ for the mesogenic groups by preferentially promoting conformations in which the mesogenic groups lie parallel/anti-parallel to the mean field director. Application of the ordering potential also leads to the dendrimer becoming more "rod-shaped" overall.

Based on these observations the coarse-grained (CG) model shown in figure 3.4 was designed. The rigid inner core of the dendrimer was represented as a single sphere, while the chains linking the mesogens to the dendrimer were divided into four spheres: with one representing the O(SiMe$_2$)$_2$ group and three each representing a (CH$_2$)$_3$ segment. Finally, the mesogens were modelled as spherocylinders.

The size of the coarse-grained sites was determined by matching the excluded
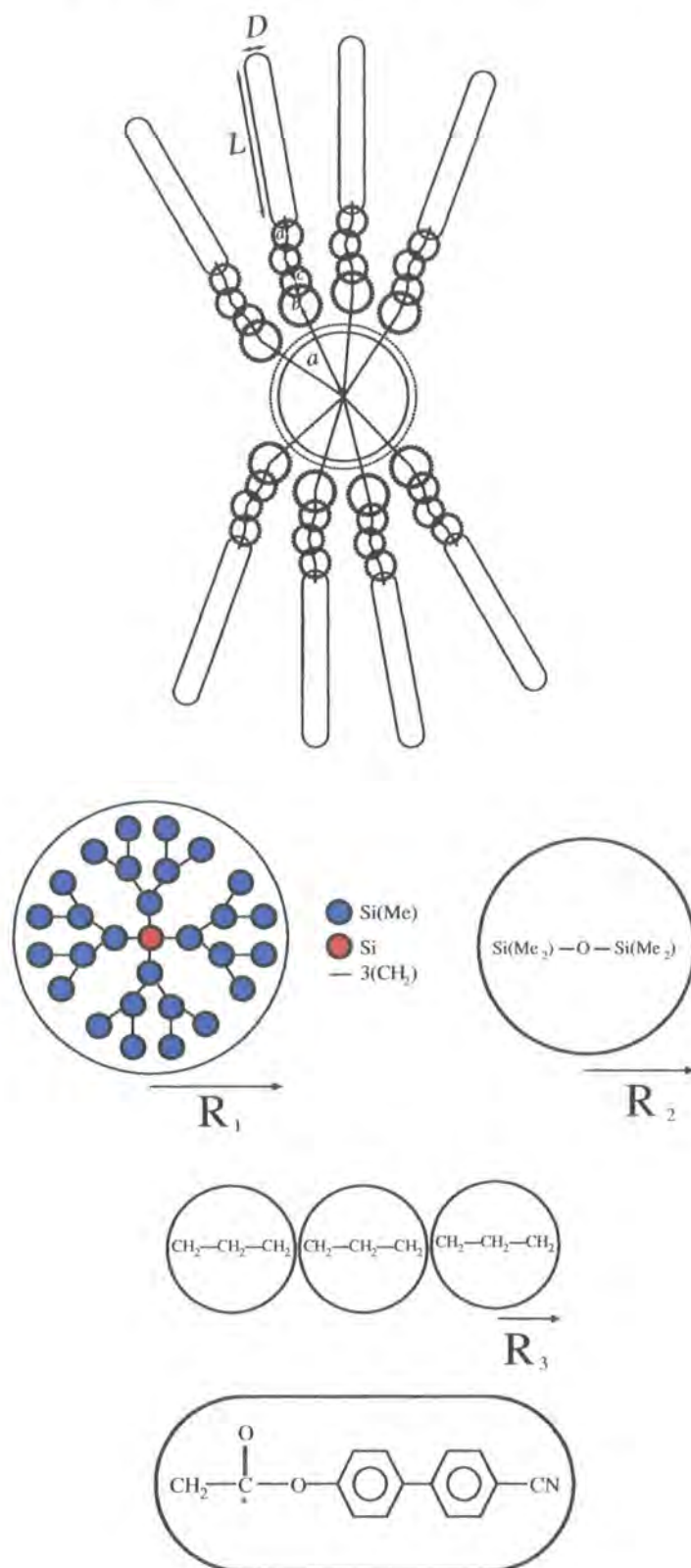
Figure 3.4: Schematic diagram showing the dimensions and coarse-grained mapping for the model dendrimer. In the top part of the diagram bold lines around the spheres are drawn to scale for appropriate σ values and dotted lines indicate the potential cutoff ($2^{1/6}\sigma$). Only 8 of the 32 chains are shown for clarity.

volume of each site with that of the atomistic structure it represented. The ensemble averaged volumes obtained from the Monte Carlo calculations were measured using a Connelly surface with probe radius 0.1 Å, to obtain the radii, R_1, R_2, R_3 (table 3.1). The equilibrium bond distances, $a - d$, (table 3.1) for the CG-sites were obtained also as ensemble average values from the Monte Carlo calculations. The distribution functions for the angles and dihedrals were also calculated. However, as these distributions were very broad and showed no strong peaks, it was decided to neglect the angular and torsional terms for the model system.

Determination of appropriate L and D parameters for the spherocylinders was more problematic. The initial Monte Carlo simulations yielded a mean mesogen length of 16.14 Å $(L+D)$ including van der Waals radii. The volume of the mesogenic group, $V = \frac{4}{3}\pi \left(\frac{D}{2}\right)^3 + L\pi \left(\frac{D}{2}\right)^2$, therefore yields a value of $L/D = 2.84$, with $\sigma_{sc} = 3.74$ Å. However, it is know from previous simulations of pure spherocylinders that liquid crystal phases will not form with such a small aspect ratio. Instead while fixing the diameter of the spherocylinder at $D = \sigma_{sc} = 3.74$ Å, which is appropriate for the chemical structure, the aspect ratio of the spherocylinder was increased to a $L/D = 6$. This ratio is known from earlier simulations to give a large nematic region in the spherocylinder phase diagram. We also carried out simulations with a longer $L/D = 8$ spherocylinder mesogen.

For simplicity and in common with many CG-polymer models[112,113] purely repulsive potentials were used. For the spherical sites the cut and shifted form of the Lennard-Jones potential was employed

$$U_{LJ} = \begin{cases} 4\epsilon \left[\left(\frac{\sigma}{r_{ij}}\right)^{12} - \left(\frac{\sigma}{r_{ij}}\right)^6 + \frac{1}{4} \right], & r_{ij} < r_{cut}, \\ 0, & r_{ij} \geqslant r_{cut}, \end{cases} \tag{3.1}$$

where U_{LJ} is the Lennard-Jones potential at a position r_{ij} and ϵ and σ are respectively the well depth and distance of closest approach, which characterize the potential. The potential goes smoothly to zero at $r_{cut} = 2^{1/6}\sigma$. For mesogenic units the soft repulsive spherocylinder (SRS) potential,[56,60] was used where r_{ij} in equation 3.1 is replaced by the distance of closest approach for the spherocylinder (see section 2.1.2). This potential can also be used to describe the interaction of a spherocylinder

with a Lennard-Jones site, by considering d_{ij} as the minimum separation between the centre point of the sphere and the line that runs along the centre of the spherocylinder. (This is equivalent to considering a sphere as a spherocylinder where the length of the spherocylinder, L, is equal to zero.) The value of ϵ for each CG-site was set to 0.247×10^{-20} J based on earlier work using hybrid Lennard-Jones/Gay-Berne models.[114,115]

In CG-polymer models it is common to use FENE[116] potentials for the bonding terms, which have the form

$$U_{FENE}(r_{ij}) = -\frac{1}{2}k(l_{max} - l_0)^2 \ln \left(1 - \frac{(r_{ij} - l_0)^2}{(l_{max} - l_0)^2} \right). \tag{3.2}$$

The drawback of the FENE potential is that as it has finite bounds. So the timestep used in the simulation must be small enough to ensure that the bonds do not exceed the bounds, which would cause the potential to go to infinity. In order to allow the use of a larger timestep a similar, but slightly simpler bonding potential was used

$$U_{\text{bond}}(r_{ij}) = \frac{1}{2}k_{\text{bond}}(r_{ij} - l_0)^{12}, \tag{3.3}$$

where the bond length is given by r_{ij}, the force constant is given by k_{bond}, and l_0 values correspond to the equilibrium bond lengths a, b, c or d of table 3.1. Equation 3.3, has a shallow bottom and strongly repulsive walls like the FENE potential and is therefore restrictive in terms of bond distances allowed (see figure 3.5). As this potential was used all bonded pairs of CG-sites were excluded from the sum of nonbonded terms.

Finally, appropriate masses for each CG-site were taken, along with a moment of inertia of 5.9930×10^{-24}kg m^2 for the mesogenic particle.

3.3   Simulation Details

The bulk phase simulations consisted of 100 coarse-grained dendrimer molecules (12900 spherical sites and 3200 spherocylinders) and used cubic periodic boundary conditions. The system was initially set up in the gas phase on a lattice to ensure that
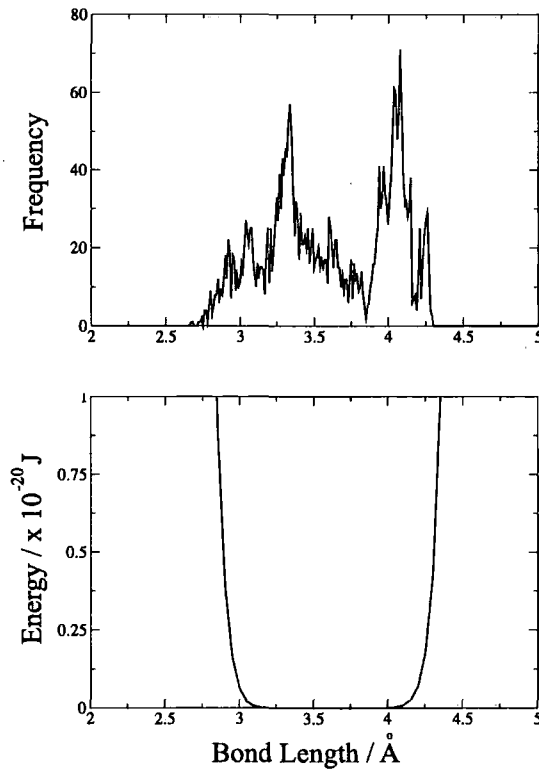
Figure 3.5: Top: The bond distribution of bond c obtained from the atomistic Monte Carlo calculations. Bottom the potential energy profile of bond c in the coarse-grained model.

Parameter	Measurement	Value
L	Length of spherocylinder	$6D$, $8D$
$D = \sigma_{sc}$	Breadth of spherocylinder	3.74 Å
$R_1 = \frac{2^{\frac{1}{6}}\sigma_{small}}{2}$	Radius of large sphere	10.6853 Å
$R_2 = \frac{2^{\frac{1}{6}}\sigma_{medium}}{2}$	Radius of medium sphere	3.1167 Å
$R_3 = \frac{2^{\frac{1}{6}}\sigma_{large}}{2}$	Radius of small sphere	2.2955 Å
a	Large sphere-medium sphere bond length	14.901 Å
b	Medium sphere-small sphere bond length	3.5973 Å
c	Small sphere-small sphere bond length	3.617 Å
d	Small sphere-spherocylinder bond length	2.979 Å
k_{bond}	Bond force constant	60×10^{-20} J Å^{-12}

Table 3.1: Parameters used in the definition of the CG-simulation model.

the molecules did not overlap. The system was then compressed, and a number of different densities obtained using NpT simulations with the Nosé-Hoover thermostat and barostat. The state points were then allowed to equilibrate during an NVT run, where changes in the energy, structure and order parameter could be observed and measured. The points at the highest densities were run solely in the NpT ensemble. For the isotropic systems both the NpT and NVT runs were typically 750 ps, for the systems at high density the runs were much longer, extending up to 35.75 ns.

The simulations were done using the parallel domain decomposition program, GBMOL_DD (see section 2.2.6), written by Ilnytskyi and Wilson,[98,102,103] and using a velocity Verlet algorithm suitable for anisotropic particles,[98,102,103] and employed time-steps of between 5.0-7.5×10^{-15} s. The value of the timestep was checked as the system changed density to ensure that there was conservation of the extended Hamiltonian in the appropriate ensemble.

3.4 Results

The pressure-density phase diagram for the two dendrimer systems are shown in figure 3.6. For each state point the evolution of nematic and smectic ordering was checked by measuring the order parameter of the system and calculating the radial distribution function (figure 3.7). The evolution of the order parameter with respect to the density in shown is figure 3.8. For the $L/D = 6$ system for the last few state points there was a slight increase in $\langle S_2 \rangle$ and snapshots of the system at these densities show the spontaneous formation of microphase segregated domains, which is accompanied by a rise in the first peak of the radial distribution function for the spherocylinders.

A further increase in the density leads to the formation of liquid crystal order within these domains as illustrated by the snapshot in figure 3.9b. However, despite run lengths of up to 7.5 ns, these domains did not merge to form an overall smectic phase. The orientational correlation function, given by

$$C_1 = \langle \cos(\hat{\mathbf{u}}(t) \cdot \hat{\mathbf{u}}(0)) \rangle , \tag{3.4}$$
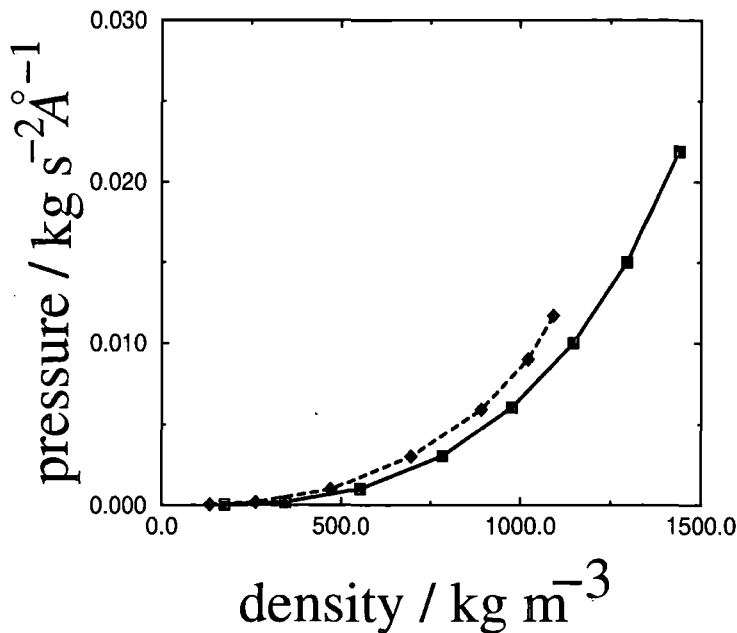
Figure 3.6: Pressure-density phase diagram for the model dendrimer. The bold line is for the system with $L/D = 6$ mesogens and the dashed line for the system with $L/D = 8$ mesogens.

where $\hat{\mathbf{u}}(t)$ is the orientation vector of a spherocylinder at time t and $\hat{\mathbf{u}}(0)$ the orientation vector at the $t = 0$ mark, shows that part of the problem is the extreme viscosities of these systems (see figure 3.10). To see if it was possible to speed up the annealing of the domains, an external potential was applied, $U_{\mathrm{ext}} = -\epsilon_{\mathrm{ext}} P_2 \left(\cos \theta \right)$, to the spherocylinders. This led to uniform alignment of the local directors within each domain within 1.0 ns. However, the high viscosity of the phase, allowed only slow movement of molecules within the phase and domains were not able to merge during the time scale of the simulations. Removal of the field led to a slow relaxation of the domain directors over a period of 1-2 ns (as shown in figure 3.11).

For the $L/D = 8$ system the four highest density state points also showed spontaneous microphase separation. Here, the use of longer spherocylinders led to microphase separation at a lower density and the spontaneous formation of larger liquid crystalline domains. However, despite runs of up to 35.75 ns the domains did not combine to form a mesophase, again it is possible that the viscosity of the system hindered the annealing process (figure 3.12 shows the decay of the pairwise orienta-
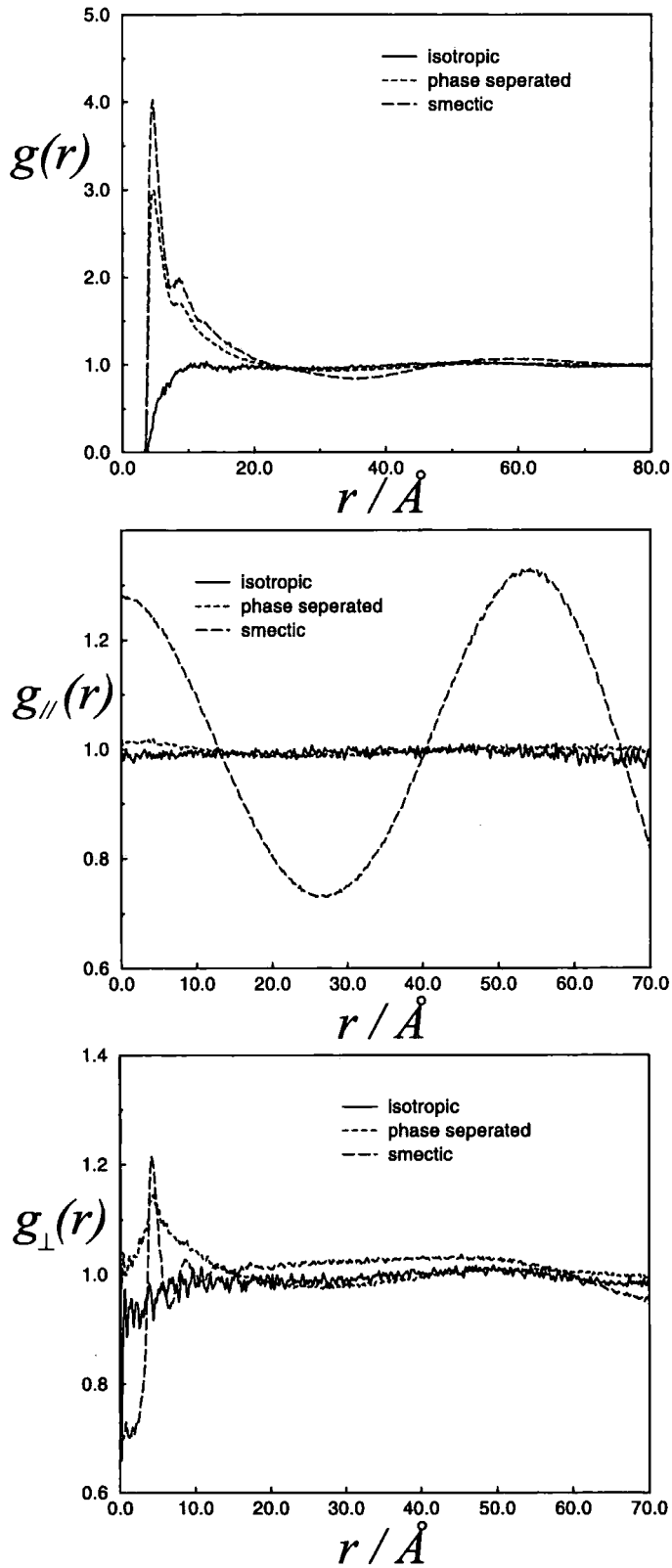
Figure 3.7: Radial distribution functions calculated for the isotropic phase (density 132.6 kg m^{-3}), phase separated system (density 891.3 kg m^{-3}) and smectic phase (density 1022.23 kg m^{-3}) of the $L/D = 8$ dendrimer.
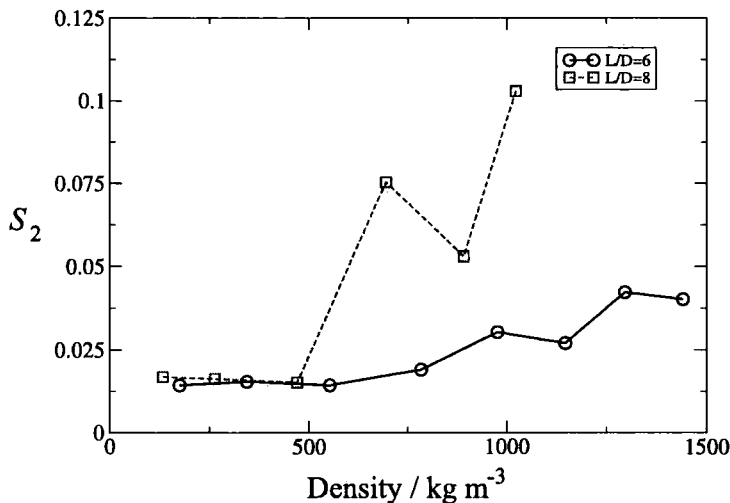
Figure 3.8: Order-density phase diagram. The bold line and circles are for the system with mesogens of $L/D = 6$, the dashed line and squares are for the system with mesogens of $L/D = 8$.

tional correlation function for the $L/D = 8$ model). Application of a small aligning field of strength $\epsilon_{\text{ext}} = 2$ kJ mol^{-1}, did lead to the domains merging and the formation of a smectic liquid crystal phase, as shown in figure 3.9c. This phase remained upon removal of the applied field and was completely stable. Simulations of > 5 ns were carried out to check that there was no decay of orientational or positional order over this period on removal of the field (see figure 3.13). Application of a field in this way does not guarantee the thermodynamic stability of the phase. However, given that there is no decay of orientational order on removal of the field and that the microphase separation leads spontaneously to the formation of smectic domains it seems likely that this smectic phase is the equilibrium structure.

The transition to a smectic phase can be seen in the change in the radial distribution functions as shown in the in figure 3.7. For the smectic phase there is a strong growth in the first peak of $g(r)$ for the mesogenic groups, accompanied by an abrupt change from no structure in $g_{\parallel}(r)$ to clearly defined peaks associated with the mesogenic layers. Liquid-like structure is seen in $g_{\perp}(r)$, with only one sharp peak in the smectic phase and a secondary smaller peak at approximately
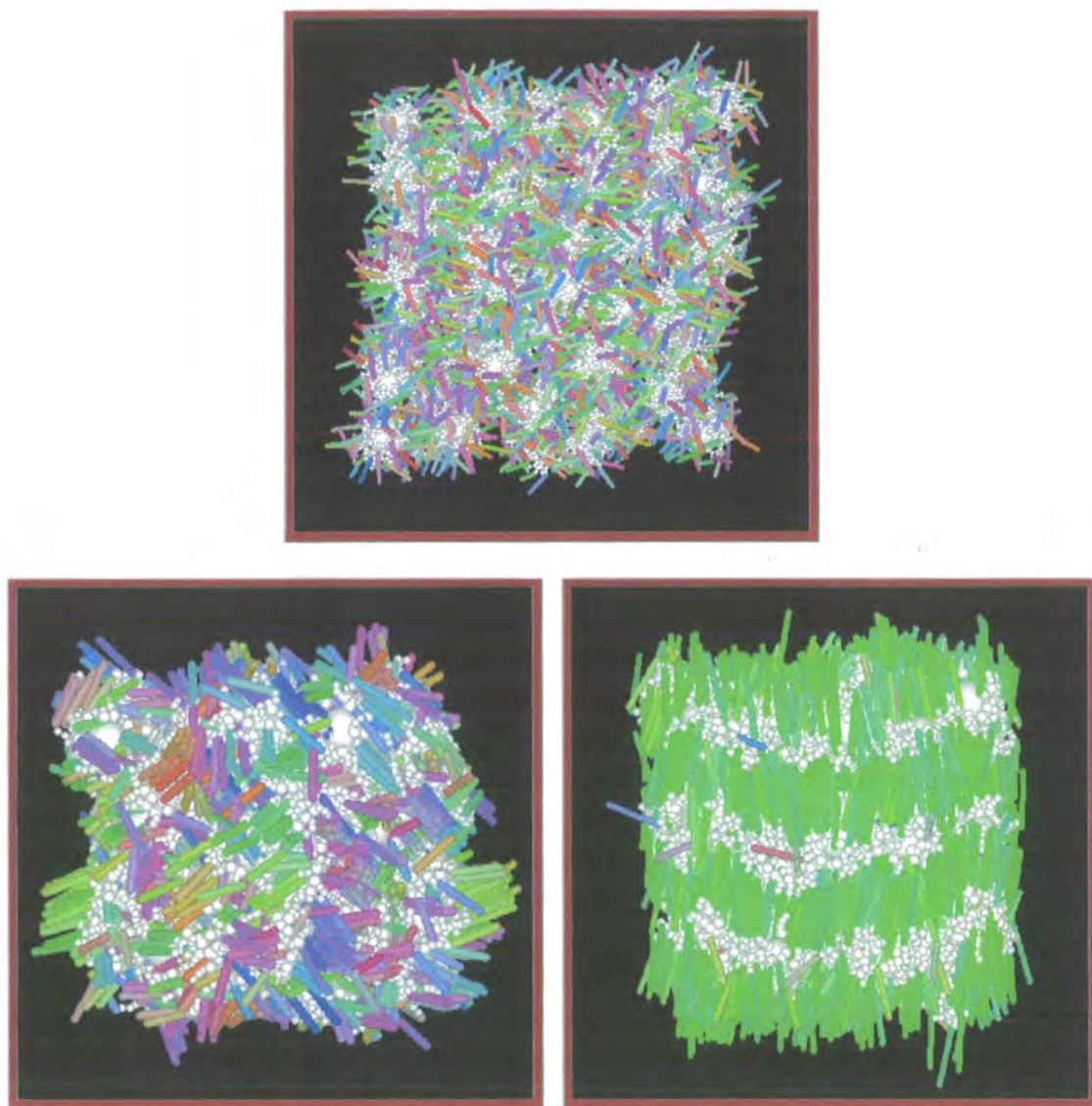
Figure 3.9: Snapshots from simulations showing the changing bulk structure of the model dendrimer fluid. Top: (a) Isotropic phase for the $L/D = 6$ system at a density of 174.5 kg m^{-3}. Bottom left: (b) Microphase segregated structure of the $L/D = 6$ system at a density of 1440.6 kg m^{-3}. Bottom right: (c) Smectic-A structure for the $L/D = 8$ system at a density of 1022.23 kg m^{-3}. Spherical sites are shown in white. Spherocylinders are colour coded with green along the director and red/green/blue colours corresponding to mutually perpendicular directions.
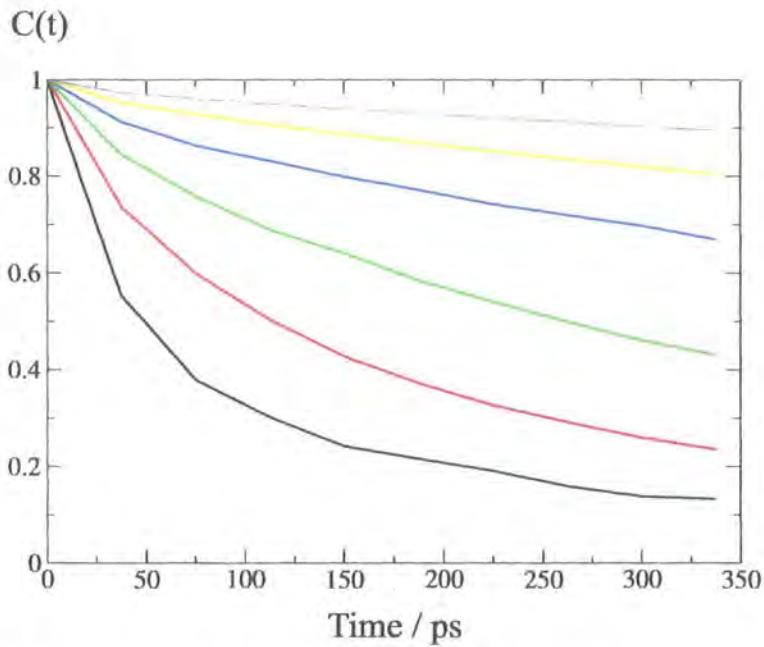
Figure 3.10: The correlation function of the $L/D = 6$ mesogen system for a range of densities: (from bottom to top) 553.4 kg m^{-3}, 784.5 kg m^{-3}, 997.7 kg m^{-3}, 1147.2 kg m^{-3}, 1296.2 kg m^{-3} and 1440.6 kg m^{-3}.
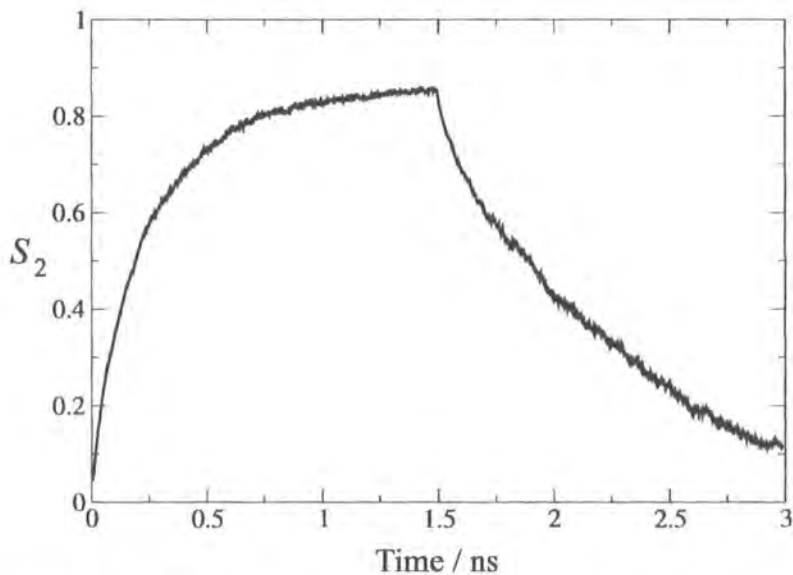
Figure 3.11: The time evolution of the order parameter of the $L/D = 6$ dendrimer system at a density of 1296.2 kg m^{-3}, the field was applied for 1.5 ns and then removed.
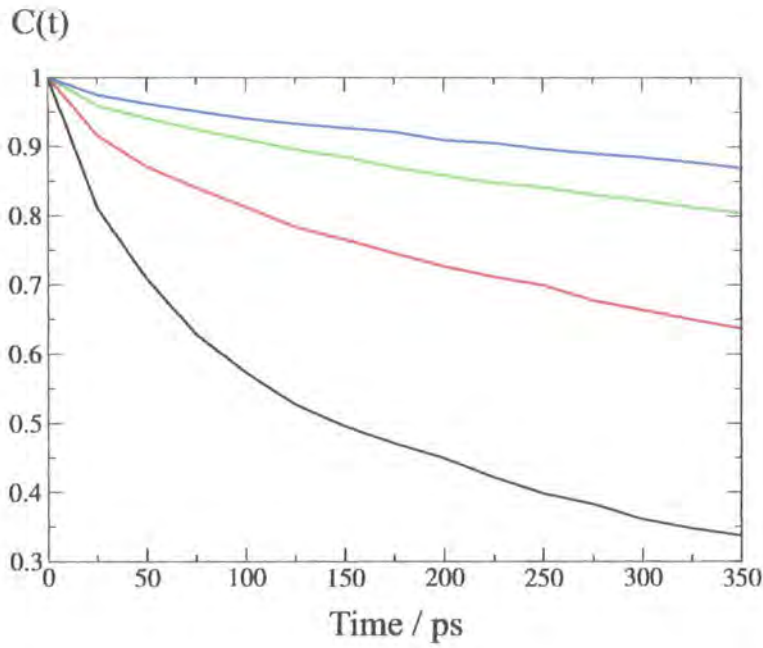
Figure 3.12: The correlation function of the $L/D = 8$ mesogen system at number of densities: (from bottom to top): 470.4 kg m^{-3}, 695.6 kg m^{-3}, 891.3 kg m^{-3} and 1022.2 kg m^{-3}.
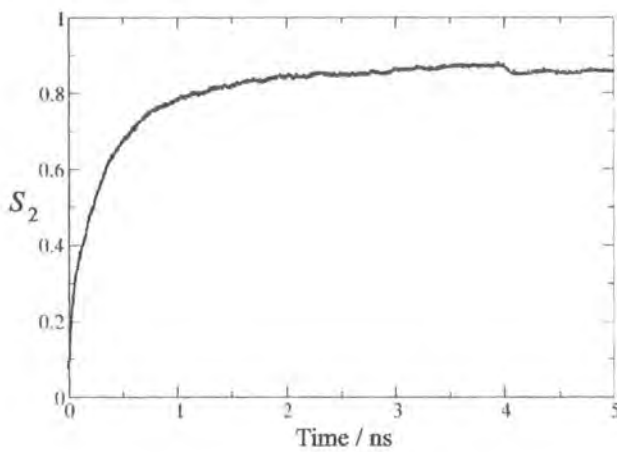
Figure 3.13: The time evolution of the order parameter of the $L/D = 8$ dendrimer system at a density of 1022.2 kg m^{-3}, the field was applied for 4.0 ns and then removed.

twice the distance of the first peak, indicating that this phase is a fluid smectic, i.e. smectic-A or smectic-C. The layer spacing of the smectic phase can be calculated from the distance between the peaks in $g_\parallel (r)$, this is approximately $d = 53.5$ Å. This value was confirmed by the independent calculation of the structure factor, $S(k)$, which has a maximum value for the wavevector $\mathbf{k_{max}} = 2\pi(0/L, 0/L, 3/L)$ with $k_{max} = |\mathbf{k_{max}}| = 0.1175$ for the cubic box of length $L = 160.4$ Å, at a density of 1022.23 kg m^{-3}. This inter-layer distance approximately corresponds to the distance across a dendrimer core plus a single spherocylinder (51.29 Å). This indicates that mesogen layers are fully interdigitated, with mesogens from the layer above mixing completely with those from the layer below. From the direction of the wavevector, $\mathbf{k_{max}}$, it is possible to define a layer normal vector, $\mathbf{p}$; and to calculate the mean tilt angle, $\langle\theta\rangle = \langle\mathbf{p}\cdot\mathbf{n}\rangle$, for the system. The tilt angle was calculated also for each layer individually, replacing $\mathbf{n}$ by a separate director for each layer, $\mathbf{n_{layer}}$. $\langle\theta\rangle$ for the system is equal to $0.4° \pm 0.2$ in the smectic phase and the maximum tilt angle detected for an individual layer during the course of the simulation was $2.7°$. These data indicate that the mesophase is smectic-A rather than smectic-C. However, there are local domains where layers are not uniformly parallel to $\mathbf{k_{max}}$ and there is local tilting of mesogenic groups relative to $\mathbf{n}$ (as can be seen in figure 3.9c).

These results tie in well with the interpretation of X-ray diffraction measurements from third generation dendrimers by Ponomarenko and co-workers.[14] These X-ray studies are consistent with a morphology corresponding to alternating mesogen/dendrimer core layers as that found in the simulation. Moreover, from the X-ray layer spacing in the Ponomarenko *et al.* work it is evident that each mesogenic layer contains spherocylinders from the dendrimer above and below the layer and there is a considerable degree of interdigitation of mesogens for the 3rd generation dendrimer.

In order for the interdigitated layer structure to form, the dendrimers must undergo a major change in shape from the spherical structure seen both in the gas and liquid phases (figure 3.16a). This can be seen from the plots of the site distribution function, $\rho(r)$, figure 3.14, for the liquid phase, microphase separated region and the smectic mesophase. Here the distances, r, of sites within the dendrimer are measured relative to the position of the central sphere in each molecule. In addition

figure 3.15, shows the partial distribution functions $\rho_{\parallel}(r)$ and $\rho_{\perp}(r)$ in the smectic mesophase. These were calculated for cone-like sectors limited by the angles $\theta = \pi/6$ around the head and tail directions of the director for $\rho_{\parallel}(r)$; and within the sector given by $\theta \in [\pi/3, 2\pi/3]$ for $\rho_{\perp}(r)$. The $\rho(r)$ curves demonstrate that the radially averaged structure of the dendrimer does not change much across the phases. (There is a small increase in the density of chains and spherocylinders close to the core in the microphase separated and smectic regimes arising from the increase in the bulk density of the system). However, there are major differences in the behaviour of partial distribution functions between phases. While $\rho_{\parallel}(r)$ and $\rho_{\perp}(r)$ in the isotropic phase take the same form as $\rho(r)$ in figure 3.14a (and are therefore not plotted), the form of $\rho_{\parallel}(r)$ and $\rho_{\perp}(r)$ in the smectic phase (figure 3.15) are radically different. There is a dramatic increase in the spherocylinder density in $\rho_{\parallel}(r)$ relative to $\rho_{\perp}(r)$ and an increase in the peaks corresponding to the chain atoms in $\rho_{\perp}(r)$ relative to $\rho_{\parallel}(r)$. These changes indicate that the mesogenic groups become aggregated at the two ends of the dendrimer. This shape change is caused by conformational changes in the chain, which lead to it being confined around the equatorial region of the core. This change arises from a strong coupling of internal molecular structure and the bulk structure of the phase itself. This shape change can be seen in figure 3.16, which shows a snapshot of a representation of a typical molecular conformation in the isotropic, microphase separated and smectic-A phases. The snapshot are taken from the configurations shown in figure 3.9. The shape changes of the type seen in figure 3.9 have been predicted by Vanakaras and Photinos using molecular theory.[117]

While the conformational changes seen in this system are extreme, a similar coupling of internal structure and molecular environment have been noted in other systems. In particular, in side chain liquid crystal polymers the formation of well-ordered smectic phases are accompanied by an elongation of the polymer backbone, as evidenced by changes in the radius of gyration of the polymer backbone, parallel and perpendicular to the director, measured by small angle neutron scattering (SANS).[118] Moreover, recent simulations have shown explicitly that a flexible polymer backbone is excluded from smectic layers and becomes stretched as it is confined between layers composed of mesogenic groups.[119]
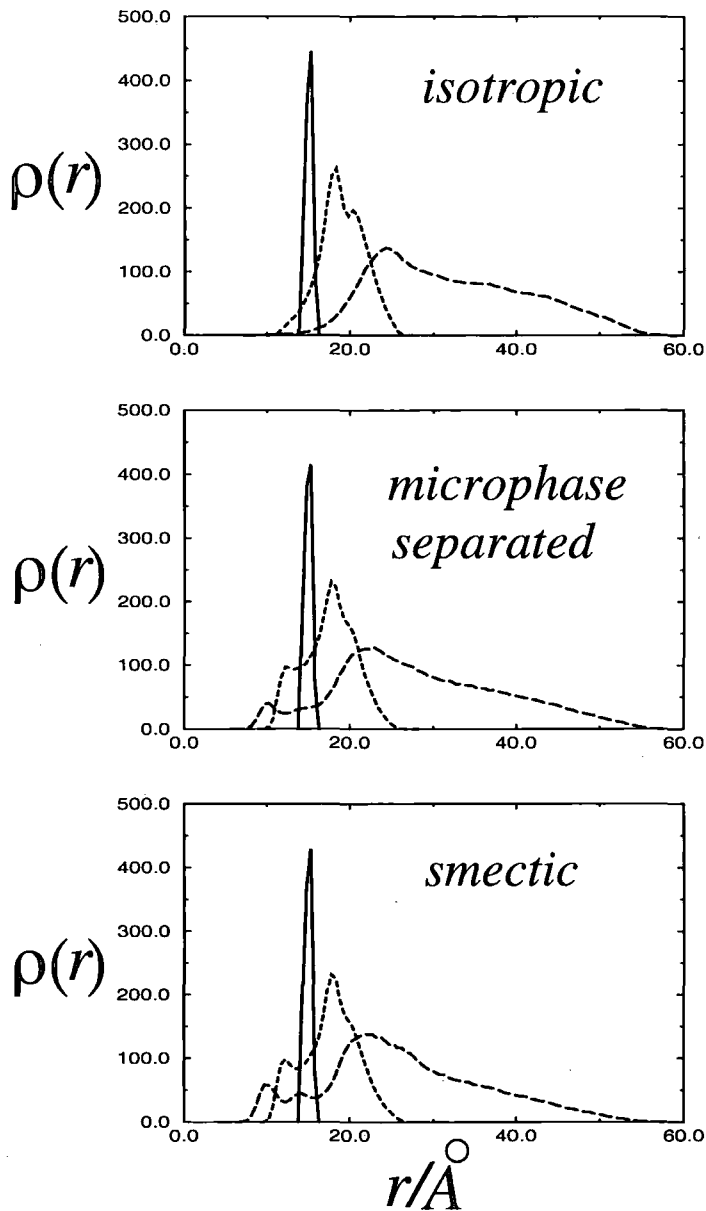
Figure 3.14: The distribution function, $\rho(r)$, in arbitrary units, for separate parts of the $L/D = 8$ dendrimer relative to the central core site. Bold line - medium sized sphere, dotted line - small spheres, dashed line - spherocylinders. (The spherocylinder has been treated as 5 sites to get a better picture of the spatial distribution for this site.) Top: (a) Isotropic phase at a density of 132.6 kg m^{-3}. Middle: (b) Microphase separated phase at a density of 891.3 kg m^{-3}. Bottom: (c) Smectic-A phase at a density of 1022.23 kg m^{-3}.
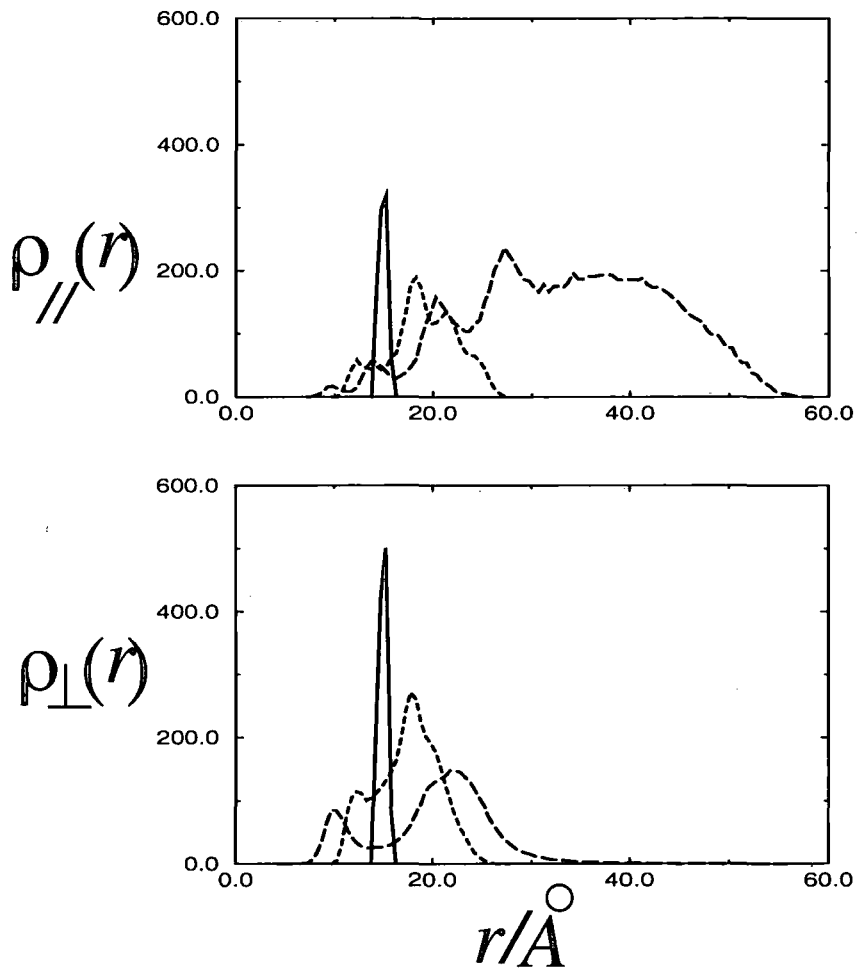
Figure 3.15: The distribution functions, $\rho_\parallel(r)$ and $\rho_\perp(r)$, in arbitrary units, for separate parts of the $L/D = 8$ dendrimer relative to the central core, plotted for the smectic-A phase at a density of 1022.23 kg m^{-3}. Bold line - medium sized sphere, dotted line - small spheres, dashed line - spherocylinders.
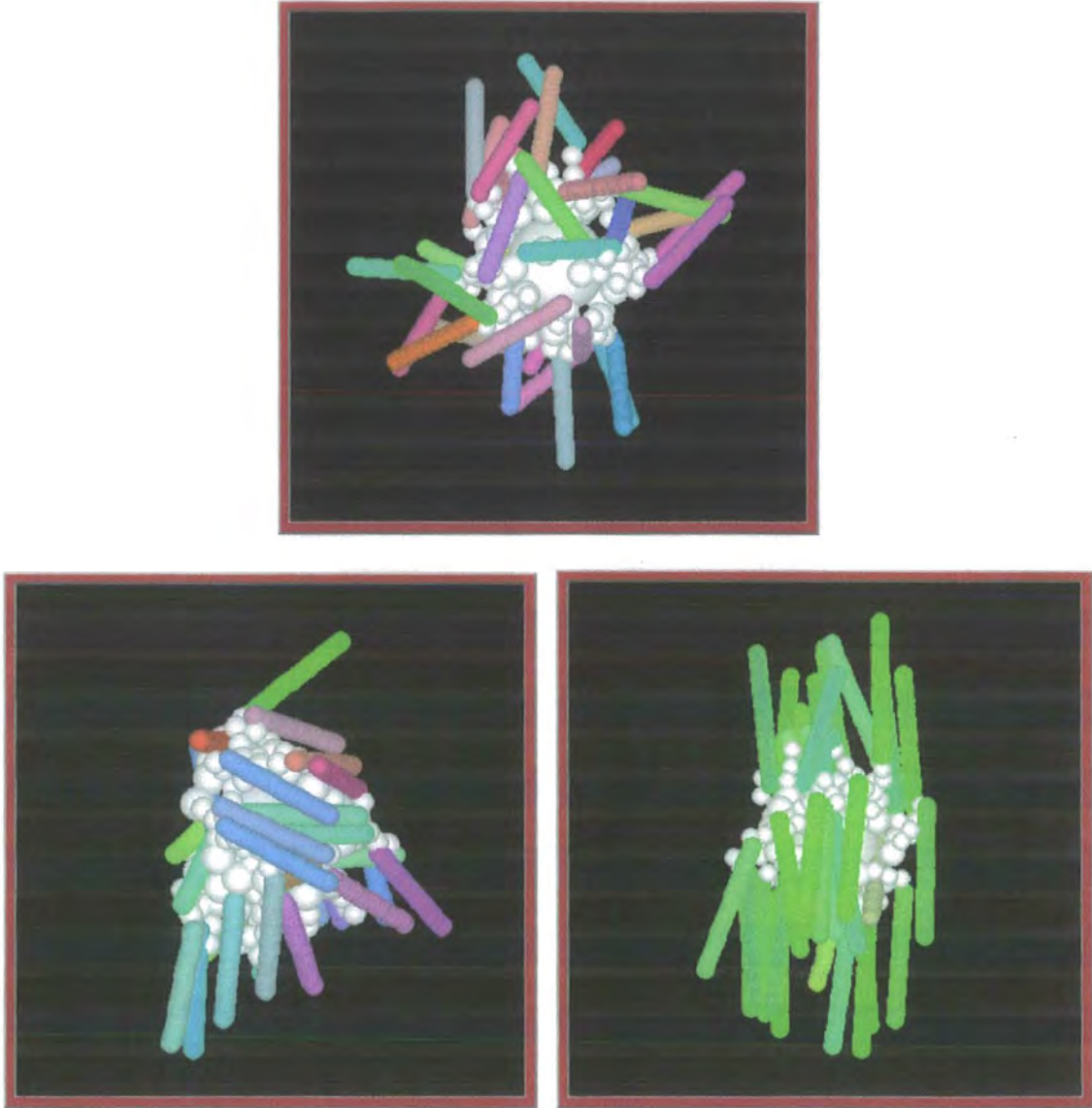
Figure 3.16: Snapshots showing the structure of a representative molecule from the different phases formed by the dendrimer. Top: (a) the $L/D = 6$ system in the isotropic phase at a density of 174.5 kg m^{-3}. Bottom left (b) the $L/D = 6$ system in the isotropic phase at a density of 1440.6 kg m^{-3}. Bottom right (c) the $L/D = 8$ system in the smectic-A phase at a density of 1022.23 kg m^{-3}.

3.5   Conclusions

A coarse-grained simulation study of a model carbosilane liquid crystal dendrimer in the bulk phase has been carried out. The simulations show the formation of a smectic liquid crystal phase in which individual layers of mesogens are separated by layers containing the dendrimer cores and the first part of the linker chains. Mesogens from a single dendrimer contribute to smectic layers above and below the dendrimer core. The simulations demonstrate a strong coupling between internal molecular structure and molecular environment. This leads to the mesogenic groups becoming aggregated at the two ends of the dendrimer. Consequently, the simulations show that individual dendrimer molecules change from being "spherical in the liquid phase" to "rod-shaped" in the liquid crystal phase.

The dendrimer studied here is part of a broader class of polyphilic mesomorphic materials, in which separate building blocks with different types of interaction site are combined (for example aliphatic, aromatic, fluoro, and siloxane-based segments).[21] In addition to dendritic molecules,[120] such systems include rod-coil molecules,[121] low molecular weight polyphilic molecules[21,122] and ternary block-copolymers.[123] Microphase separation in these materials opens up the opportunity to self-assemble well-defined nanostructures for potential molecular electronics, photonics or biomimetic applications.[124,125] The CG-simulation methodology presented here (possibly modified to include anisotropic attractive interactions) may provide a route towards the simulation of these systems. As such it could be a useful tool in helping design novel nanoscale structures for future applications.

Chapter 4

Parallel-Tempering Techniques

This chapter outlines a new simulation technique known as *parallel-tempering* that can be used to improve the sampling of phase space in molecular simulations. This technique was implemented in an in-house Monte Carlo program and was then used in the simulation of a variety of different systems to see how effective it was.

4.1 Introduction

As mentioned in section 1.6 one of the main problems with simulating macromolecular systems is that it is often difficult to sample phase space properly. Macromolecules can become stuck in potential energy (PE) wells easily and getting out of a local PE minimum is difficult as it may involve a major change in the configuration of the macromolecule. This is even true in gas phase Monte Carlo simulations for some molecules, and this poor sampling of phase space makes it harder to coarse-grain molecules accurately. In addition poor sampling means that systems must be run for a long time. If sampling can be improved, not only will the data gained be more accurate but the computer time needed to simulate systems will be reduced.

One method that can be used to improve sampling by allowing systems to move from one energy well to another more easily is parallel-tempering, also known as extended ensemble or the replica exchange method (REM).[126-131] At higher temperatures it is easier for the system to rearrange itself and move between various energy minima because the density of states is more widely distributed. Recognis-

ing this parallel-tempering works by having a series of ensembles (or replicas) of the same system running at different temperatures. Then at regular intervals a swap of the molecular coordinates of two ensembles will be attempted. These swaps are performed in the same way as a Monte Carlo move, thus ensuring that the correct Boltzmann distribution is maintained. The swap move is accepted or rejected based on the probability

$$\zeta \leq \min(1, \exp[(\beta_1 - \beta_2)(E_1 - E_2)]), \qquad (4.1)$$

where E_1 is the energy of the lower ensemble, E_2 the energy of the higher ensemble and β_1 and β_2 are equal to $1/k_B T$ for the respective ensembles.

The parallel-tempering technique was first applied in full by Geyer.[127] Previously, use had been made of replicas at different temperatures but there was only partial configurational exchange between replicas.[132] Since then parallel-tempering has been used in a wide range of areas including; statistical physics, the molecular simulations of proteins,[128–130,133] X-ray structure determination,[131,134,135] simulations of polymeric systems,[136–138] simulations of solid state systems[139,140] data analysis[141] and more.[126] Initial molecular simulations used Monte Carlo parallel-tempering but the method was adapted for use with molecular dynamics calculations. It should be noted, however, that the implementation of parallel-tempering into MD calculations will mean that "unphysical" moves will take place during the simulation. Thus parallel-tempering MD simulations cannot be used to draw conclusions about the dynamics of a system.

For the technique to work most effectively it is important to make sure that the rate of swapping between all ensembles is roughly the same. The rate of swapping between two neighbouring ensembles is determined by the overlap of their densities of states. Kofke[142–144] showed that for systems where the heat capacity at constant volume does not vary across the temperature range, assigning the temperatures of the ensembles based on

$$\frac{T_{n-1}}{T_{n-2}} = \frac{T_n}{T_{n-1}}, \qquad (4.2)$$

will mean that the overlap of the densities of neighbouring ensembles will stay approximately constant and thus so will the ensemble swapping move ratio. Figure

4.1 illustrates how parallel-tempering can be in practice with swaps between T_n and T_{n-1} being alternated with swaps between T_n and T_{n+1} so that ensembles should travel over a wide range of temperatures rather than just pairs of ensemble swapping back and forth. Parallel-tempering is most efficient when the acceptance ratio of ensemble swaps is approximately 20%[145,146] as this allows each replica to sample phase space at the new temperature. While parallel-tempering methods can be integrated into both Monte Carlo and molecular dynamics simulations here only MC parallel-tempering has been investigated.
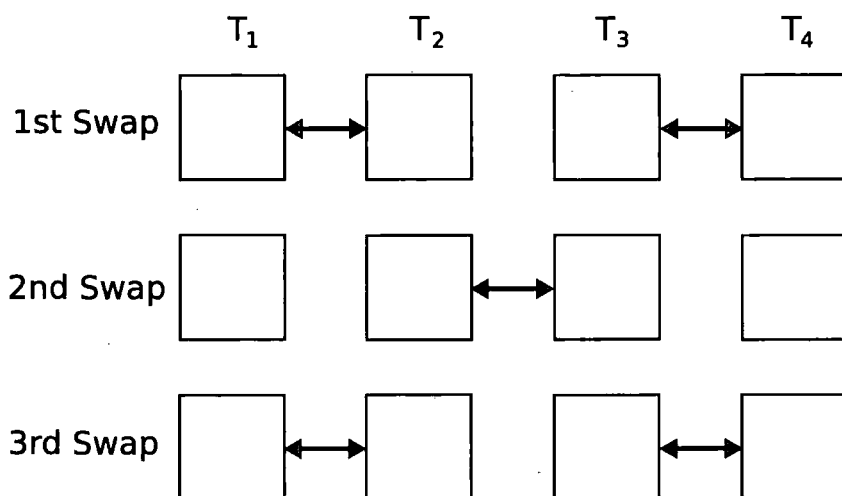
Figure 4.1: Schematic diagram showing how the swapping of ensembles occurs in parallel-tempering.

4.2 Parallel-Tempering Simulations

A variety of different systems were subjected to the temperature REM to determine how effective it is on different systems. The systems tested were; a single mesogenic molecule, a single silsesquioxane liquid crystal dendrimer and a system of 216 alkane chains. All of the Monte Carlo calculations carried out in in this chapter used an in-house program, which employed the internal coordinate approach, as described by Wilson.[147] This program was then modified to run a set of replicas in parallel and periodically perform swaps between replicas in the manner outlined in figure 4.1.

4.2.1 Mesogenic Molecule

The first test system was a relatively simple liquid crystal molecule shown in figure 4.2, a fully atomistic Monte Carlo simulation of the molecule in the gas phase was carried out. This system samples phase space quite well so the main objective with this molecule was to test the program and ensure that the ensembles were swapping properly. The simulation was run for 6×10^6 attempted MC moves. For this test system runs using both four ensembles and eight ensembles were carried out. The four ensemble run had ensembles at temperatures of 298.0K, 340.0K, 387.9K and 442.6K. For the eight run ensembles there were ensembles at these temperatures as well as at 505.0K, 576.1K, 657.3K and 750.0K. Ensemble swaps were attempted after every 1000 attempted MC moves.
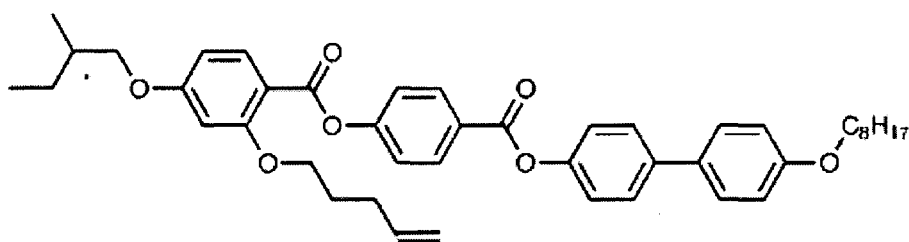
Figure 4.2: Molecular structure of the liquid crystal molecule that the parallel-tempering was tested on.

Results

The density of states for each temperature is shown in figure 4.3, as is the density of states for one of the replicas. For both the 4 and 8 replica cases it is clear that the ensemble has travelled over all of the temperatures and has sampled phase space at each of the temperatures nearly equally. This is confirmed by the data showing the path taken by an ensemble during the parallel-tempering simulation (figure 4.3 right), the replica is moving freely between all temperatures.

To see what effect parallel-tempering had on the system the distributions of different dihedral angles were calculated. The results for the biphenyl dihedral (CA-
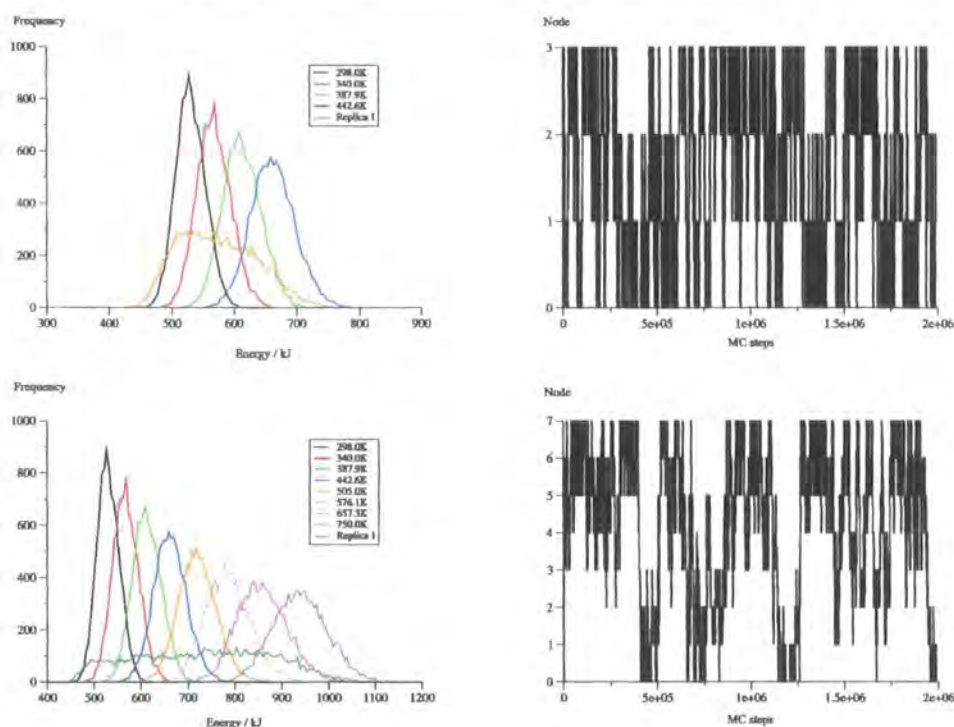
Figure 4.3: Data for the parallel-tempering of the mesogenic system.On the left are the density of states plots for the two systems. On the right is the path travelled by one replica during the simulation.

CP-CP-CA) are shown in figure 4.4.[1] The dihedrals for the extended ensemble simulations match those of the control run showing that the parallel-tempering does sample from the correct Boltzmann distribution.

4.2.2   Alkane Chains

The second system tested consisted of 216 undecane chains, the simulations used the united atom approximation, with each chain consisting of eleven sites. The chains were originally placed onto a lattice, with the chains fully elongated (i.e. set up such that all the dihedrals were in the trans conformation). The undecane molecules were then held in this all trans conformation while the positions of the chains randomised within the box. The system was then compressed so that the density was equivalent to that of undecane at atmospheric conditions ($\rho = 0.740$ g cm^{-3}). A normal MC

---

[1]Due to an incorrect value in the force field for biphenyl the dihedral distributions in figures 4.4, 4.9(a) and 4.16(a) are incorrect. However, this is irrelevant to whether the parallel-tempering method is working properly, and improving the sampling of phase space.
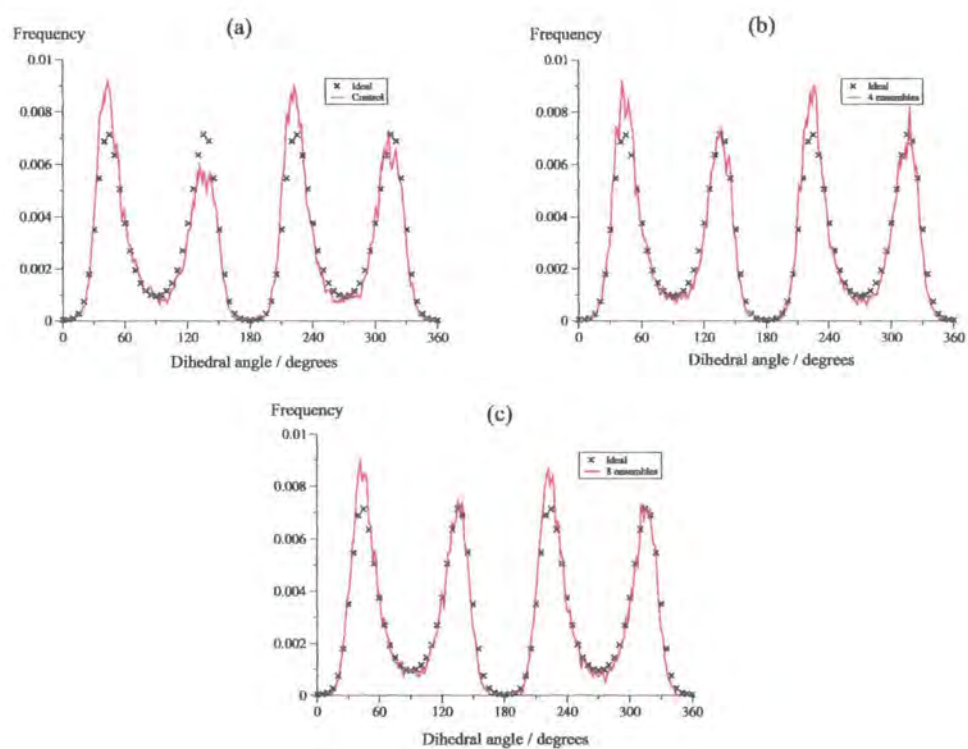
Figure 4.4: Dihedral distributions of the biphenyl dihedral in the mesogen, the crosses plot the ideal distribution and the lines the actual distribution of the: (a) normal MC simulation, (b) the parallel-tempering simulation using four ensembles and (c) the parallel-tempering simulation using eight ensembles.

simulation and a parallel-tempering MC simulation were then run for one million trial MC moves. The temperature of the lowest replica and the control run was 300.0 K and T_{n+1}/T_n was set at 1.03, a total of 28 replicas were used meaning that the upper temperature was 646.98 K.

Results

To see how effective the parallel-tempering was the decay of three different parameters was measured:

- the correlation function between the two ends of the chains, given by the expression

$$C(t) = \frac{\langle \mathbf{r}(t) \cdot \mathbf{r}(0) \rangle}{\langle \mathbf{r}(0) \cdot \mathbf{r}(0) \rangle}, \tag{4.3}$$

  where $\mathbf{r}(t)$ is the vector at time t and $\mathbf{r}(0)$ is the vector at the start of the simulation. Here time is measured in terms of MC steps.

- the radius of gyration, R_g (in Å), which gives an indication of the length of the chains, given by

$$R_g^2 = \frac{1}{N} \left\langle \sum_{i=1}^{N} S_i^2 \right\rangle, \tag{4.4}$$

  where S_i is the distance between site i and the centre of mass of the chain.

- the percentage of trans dihedrals in the system.

Parallel-tempering should increase the rate at which the system reaches an equilibrium state and cause the decay of the above parameters to occur more quickly.

The comparison between the measurements for the parallel-tempered system and the control system are shown in figure 4.5. For all three parameters parallel-tempering does have an effect in increasing the speed of decay, but only by a relatively small amount. The reason for the rather small parallel-tempering improvement is probably due to the fact that the decay happens at such a rate that parallel-tempering cannot really speed up the process a great deal. Indeed the greatest part of the decay occurs within the first one hundred thousand moves and there is very
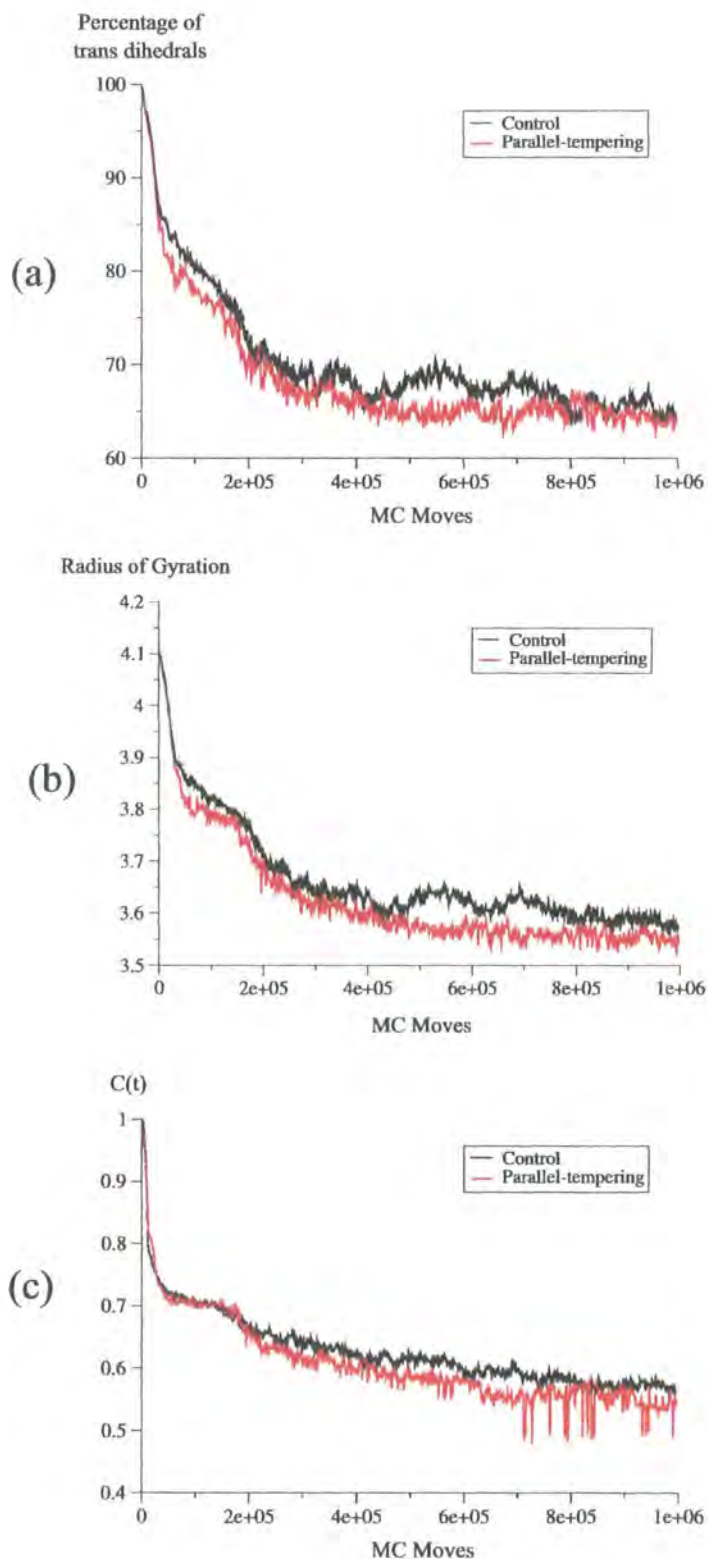
Figure 4.5: Results of parallel-tempering on the undecane chain system: (a) the percentage of trans dihedrals, (b) the radius of gyration and (c) the correlation function.

little difference here between the parallel-tempering simulation and the normal MC simulation. From this point onwards, however, parallel-tempering does have an effect and the rate at which the equilibrium system is reached is increased by ensemble exchange.

Unlike in the case of the mesogen the replicas are not moving up and down all the temperatures, instead a replica tends to move over a part of the temperature range (see figure 4.6). Despite this the replicas do seem to cross each other and the overall replica exchange rate was 20.61%, just slightly above the optimum swapping rate.
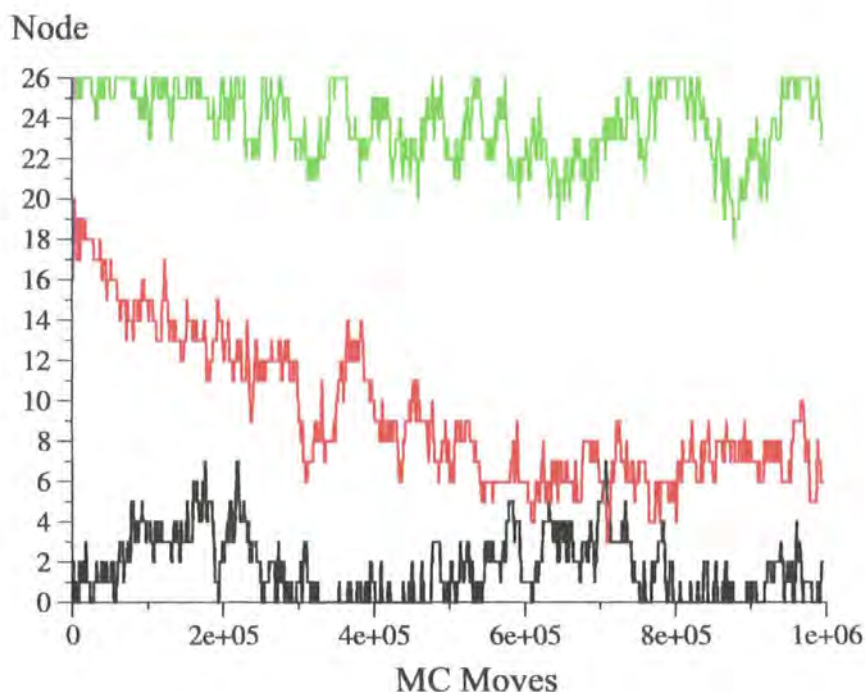
Figure 4.6: The path taken by three different replicas for the parallel-tempered simulation of undecane.

4.2.3 Silsesquioxane Liquid Crystal Dendrimer

This molecule consisted of the mesogen above combined with a silsesquioxane core, a cube built from silicon and oxygen atoms[17,18] (see figure 4.7). The relatively short flexible arms and the larger than average mesogen combine to make this molecule

very inflexible and mean that even in gas phase Monte Carlo simulations it has a tendency to get stuck in potential energy wells. This poor sampling of phase space means that this is just the type of system which should benefit from parallel-tempering techniques.

A Monte Carlo simulation of a single fully atomistic molecule in the gas phase was done, the simulation length was two million Monte Carlo moves. For the parallel-tempering simulation run 64 replicas were used, with the temperature ranging from 298.0 K up to 621.9 K ($T_{n+1} = T_n \times 1.01174$) and replica swap moves were attempted every 1000 MC moves.

Results

Figure 4.8 shows the path of three of the replicas. As with the undecane system replicas do not move over the full range of temperatures but tend to move about over a set of temperatures. The acceptance ratio of replica swaps was 23.54%, a little higher then the optimum range.

The effect of parallel-tempering on the system was measured by looking at the distributions of dihedrals within the molecule. Figure 4.9 shows the distribution of three different types of dihedrals, the Si-C-C-Si dihedral going from the corner of the silsesquioxane cube to the first branching point, the C-C-C-O dihedral of the linker connecting the core to the mesogenic groups and the dihedral of the biphenyl groups within the mesogenic groups. The distribution was averaged over all of the equivalent dihedrals within the molecule. These dihedral distributions show just how poorly phase space is sampled for this molecule, even the dihedral within the mesogenic groups is sampled very poorly. When parallel-tempering is applied there is a small but noticeable improvement in the dihedral distributions of the outer dihedral angles but the inner dihedral angle was unaffected.

4.2.4 Conclusions

Parallel-tempering does seem to improve the sampling of phase space of systems but the improvements are limited. As expected it has little effect on those systems that already sample phase space well. For those systems that do sample phase space
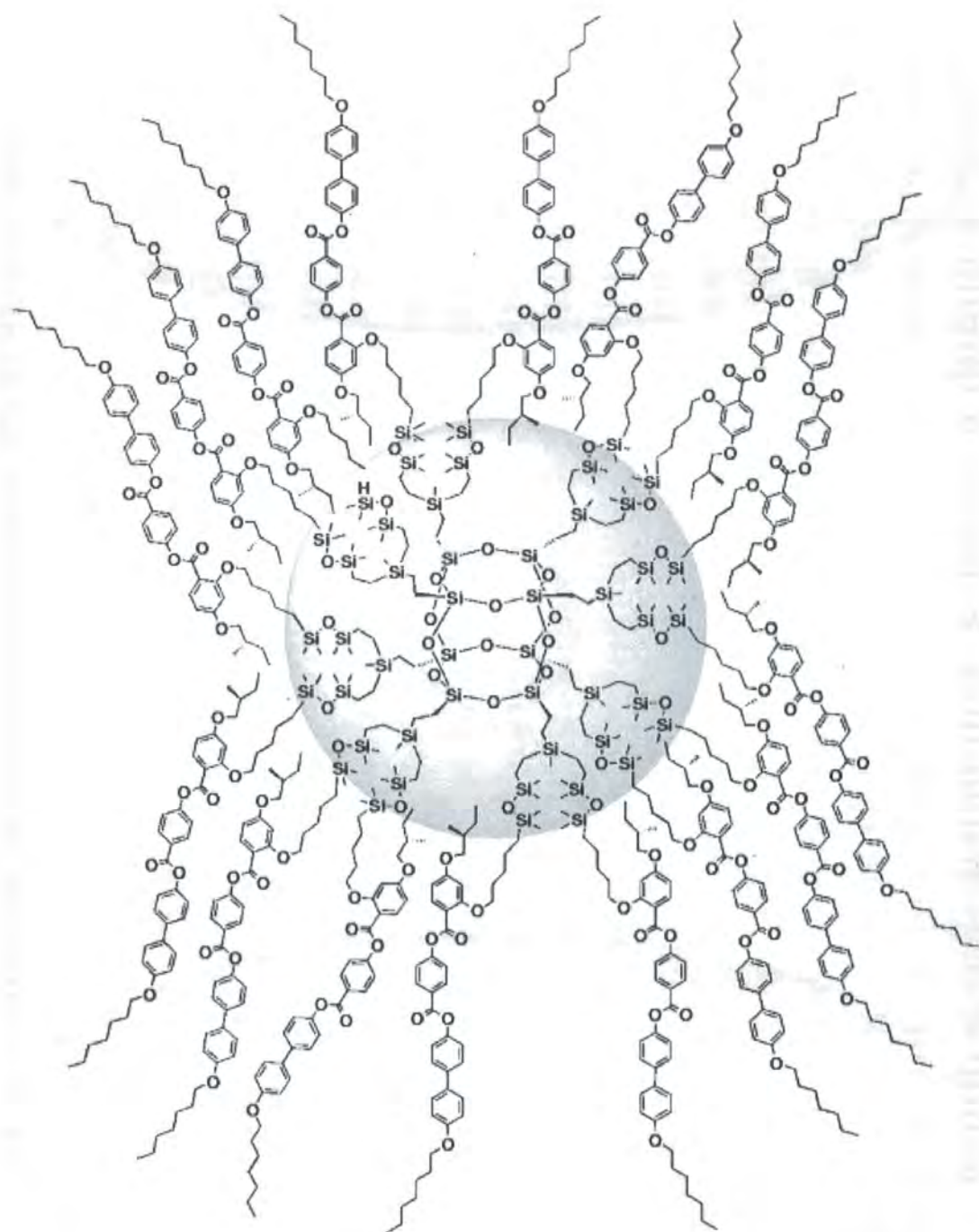
Figure 4.7: Molecular structure of the silsesquioxane dendrimer taken from reference 18.
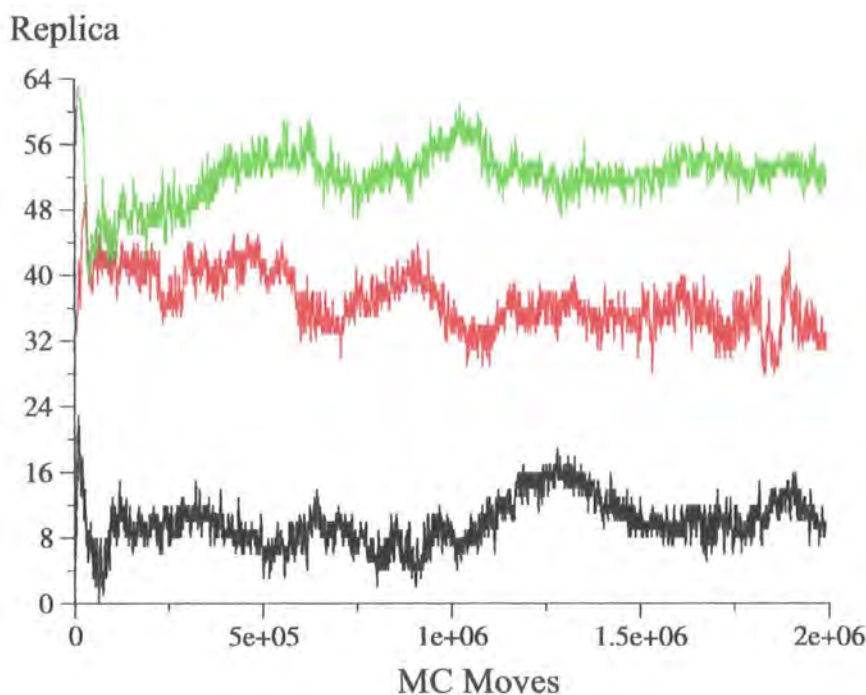
Replica

Figure 4.8: The path taken by three different replicas for the parallel-tempered simulation of the silsesquioxane dendrimer.

poorly it does improve the the sampling but the amount of benefit delivered seems to depend on the system studied. For the undecane system parallel-tempering did increase the speed at which the system reached equilibrium. For the silsesquioxane dendrimer parallel-tempering did improve the phase space sampling somewhat but as even at high temperatures the steric crowding of the dendrimer is such that the sampling of phase space is still very poor meaning the effect parallel-tempering can have is limited.

4.3   Potential Softening

The problems with the silsesquioxane dendrimer described above are often common to other dendrimer systems as well. There is little rotation about dihedrals in the inner parts of the dendrimer because this will cause one arm of the dendrimer to "crash" into another. These energy barriers are so high that such problems remain even at high temperatures.
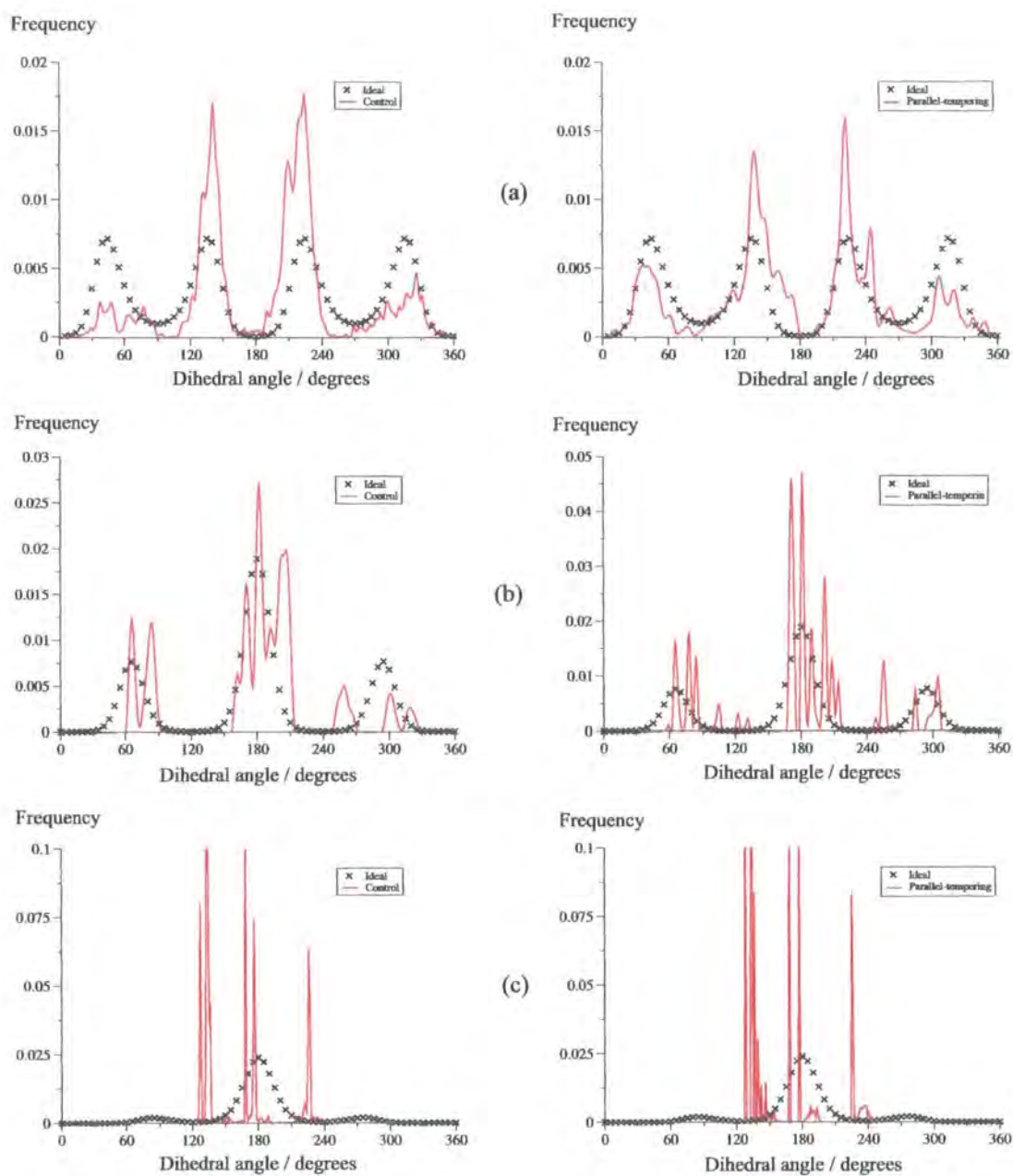
Figure 4.9: Dihedral distributions for three dihedrals in the dendrimer: (a) Si-C-C-Si dihedral between the central cage and the first branching point, (b) C-C-C-O dihedral of the linker connecting the mesogenic groups to the core and (c) the biphenyl dihedral in the mesogenic groups.

Potential softening is a method that works by reducing these energy barriers, it is an extension of the parallel-tempering technique using potentials.[136,148] Instead of having ensembles at different temperatures, different potentials are employed. The bottom ensembles has the hardest (usually the "normal") potential then the potentials of the ensembles gradually become softer. For the highest ensembles the interactions between atoms will hopefully be soft enough to allow parts of the system to pass through each other. Behaviour which would be totally unrealistic for the normal potential. So the arms of liquid crystal dendrimers should be able to move far more freely, meaning that macromolecules can rearrange with greater ease.

The precise manner of how the potential is softened can vary a great deal. Moreover, it is important to consider not only how interactions are softened but also what terms in the force field are softened. Bond stretching and bond bending terms are usually not softened, because they are not responsible for the major changes in the conformation of a molecule. In addition softening these terms too much might cause the shape of the molecules to change drastically. The aim of potential softening is to allow better configurational sampling while keeping the shape of different parts of the molecules approximately constant. For example, in the case of the silsesquioxane dendrimer the desire is that the arms of the dendrimer will be able to pass through each other but phenyl rings will not distort and bond lengths will not become ridiculously long.

Non-bonded interactions are softened as they are one of the main barriers to the poor sampling of phase space. Whether dihedrals are softened or not will depend on the system, for those molecules where dihedral rotations play an important role in determining the configurations of the molecule then it may be useful to soften them. In the case of the silsesquioxane dendrimer dihedrals do play an important role in the configuration of the molecule so it was decided that they should be softened. The softening potential used in this work was a generalised effective potential developed by Tsallis,[149] and which was first extended to MC simulations by Andricioaei and Straub.[150–152] Since then it has been used with molecular dynamics simulations as well as MC simulations.[153–155] The Tsallis potential softens both the dihedrals as

well as the non-bonded interactions, and rewrites the potential to

$$\bar{U}_q(\mathbf{r}^N, \epsilon) = \qquad U_{bond}(\mathbf{r}^N) + U_{angle}(\mathbf{r}^N) + \frac{q}{\beta(q-1)}$$
$$\ln\{1 + \beta(1-q)[U_{dihedral}(\mathbf{r}^N) + U_{nbond}(\mathbf{r}^N) + \epsilon]\} \tag{4.5}$$

where q is the softening parameter and ϵ is a arbitrary energy-shift parameter. $q = 1$ corresponds to the unsoftened potential and the larger q is, the greater the amount of softening occurs. Figure 4.10 shows how a dihedral angle is softened by the Tsallis potential. Here, although the position and depth of the potential minima are not altered the potential energy barriers are dramatically reduced. In potential softening a swap move will be accepted or rejected with the probability

$$\zeta \leq \max(1, \exp[-\beta(E_{12} - E_{11}) - \beta(E_{21} - E_{22})]) \tag{4.6}$$

where E_{11} is the current energy of ensemble one under potential one, E_{12} the energy of ensemble one under potential two and E_{21} and E_{22} the equivalents for ensemble two.
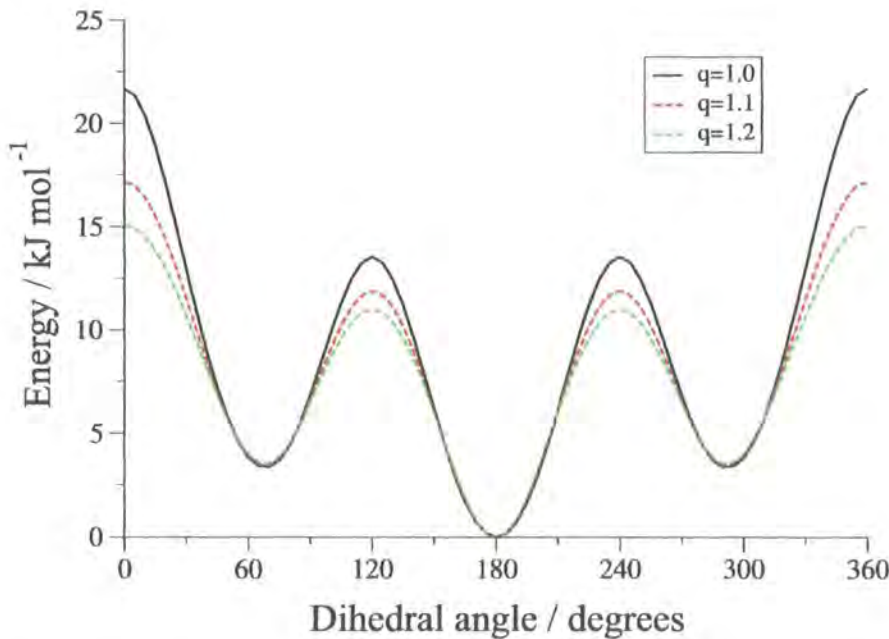
Figure 4.10: The effect of applying the Tsallis potential to a dihedral angle at $T = 298$ K.
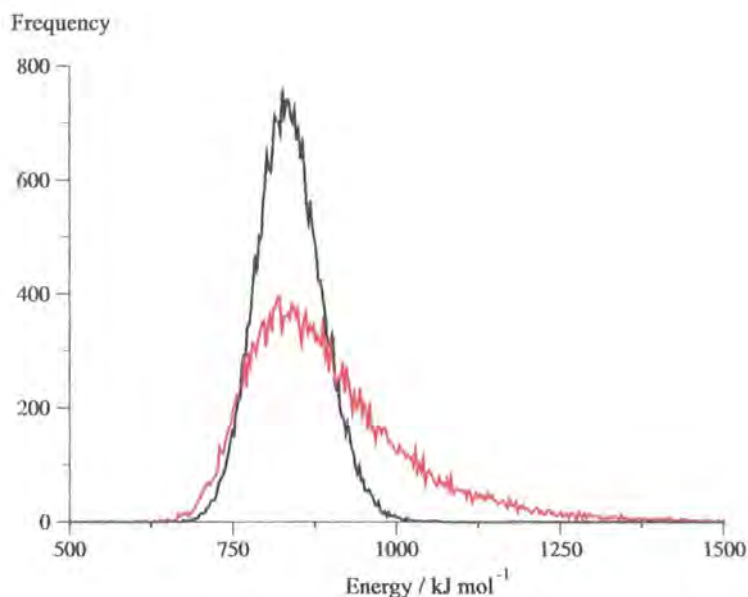
Figure 4.11: Comparison between the density of states of two systems: a system at $T = 657$ K (black line) and a system at $T = 298$ K (red line) but which has a soft potential with $q = 1.2$ applied.

As with temperature extended ensemble methods it is important to maintain an overlap between the densities of states of neighbouring ensembles. The advantage of the potential softening extended ensemble method is that the densities of states is extended to higher energies compared with the density of states of a normal potential, this feature becomes more apparent as the average energy of the system increases. This behaviour can be see in figure 4.11, here there are two systems, one which has the usual potential applied at a temperature of 657 K and one which has been simulated at 298 K but with a soft potential ($q = 1.2$) applied. The maximum peak height occurs at roughly the same point (≈ 840kJ mol^{-1}) but the softened potential is much broader, especially towards higher energies. This means that the high energy configurations are sampled much better by a soft potential than by a high temperature. Therefore potential softening should be more effective at allowing systems to cross energy barriers than temperature parallel-tempering.

As with parallel-tempering it is important to choose values of q such that the acceptance ratio of replica exchanges remains approximately 20%. In generalised

statistical mechanics appropriate values of q and ϵ can be calculated from[150,151,155]

$$\frac{1}{\beta'} = \frac{1}{\beta} + (q-1)\epsilon, \tag{4.7}$$

unfortunately such a relationship does not apply in MC or MD simulations. Instead a series of trial runs must be carried out in order so that appropriate values of q can be found.

4.4   Results for Potential Softening

4.4.1   Alkane Chains

The system described in section 4.4.1 was rerun using potential softening, again the simulations were run for one million Monte Carlo moves and replica swaps attempted every 1000 steps. Initially the potential softened simulation was run with 27 ensembles bridging between $q = 1.0$ and $q = 1.26$, the results for this simulation are show in figure 4.12. In comparison with the standard MC simulation there is a minor increase in the rate of decay of the percentage of trans dihedrals and the radius of gyration. However, this increase in the speed of the decay is less than that gained by using the parallel-tempering simulation. To see if the lack of increase in the rates of decay was due to the fact that the simulation did not reach sufficiently soft systems the simulation was rerun using 64 replicas. For this simulation $q = 3.142$ was reached for the highest ensemble.

Despite using more than twice as many replicas and reaching extremely soft systems there is very little change in the rates of decay from the first potential softened system (figure 4.13). This indicates that the lack of effect potential softening is having is not due to insufficiently soft potentials being reached but to some other reason. If we look at the acceptance ratios for replica swaps then part of the problem is apparent. For the 27 replica system the overall acceptance ratio for replica swaps is 58.17% while for the 64 replica system it is even higher at 74.96%. This high swapping ratio means that the ensembles do not have a chance to equilibrate properly at each temperature so instead the coordinates are simply passed back and
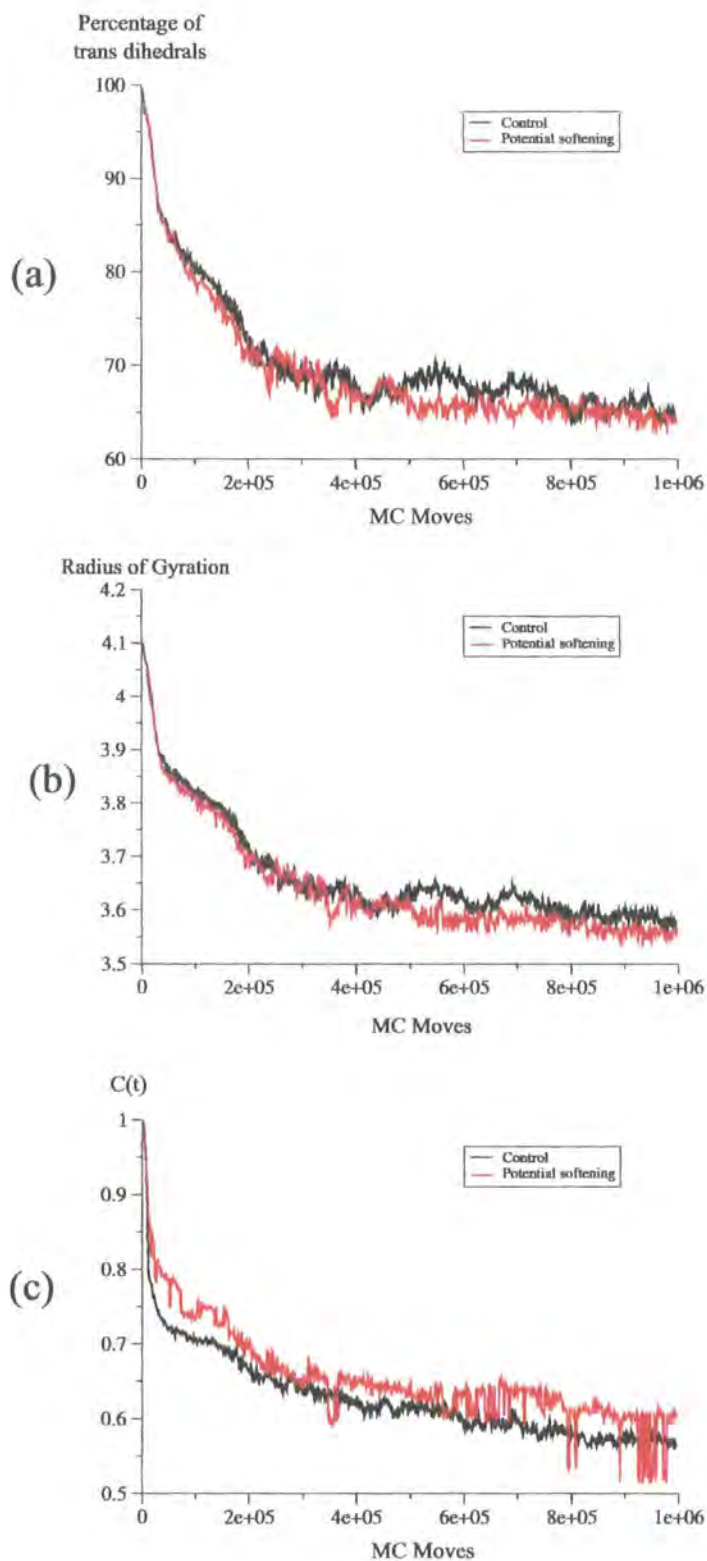
Figure 4.12: Results for the potential softening simulation of the undecane system with 27 replicas: (a) the percentage of trans dihedrals, (b) the radius of gyration and (c) the correlation function.
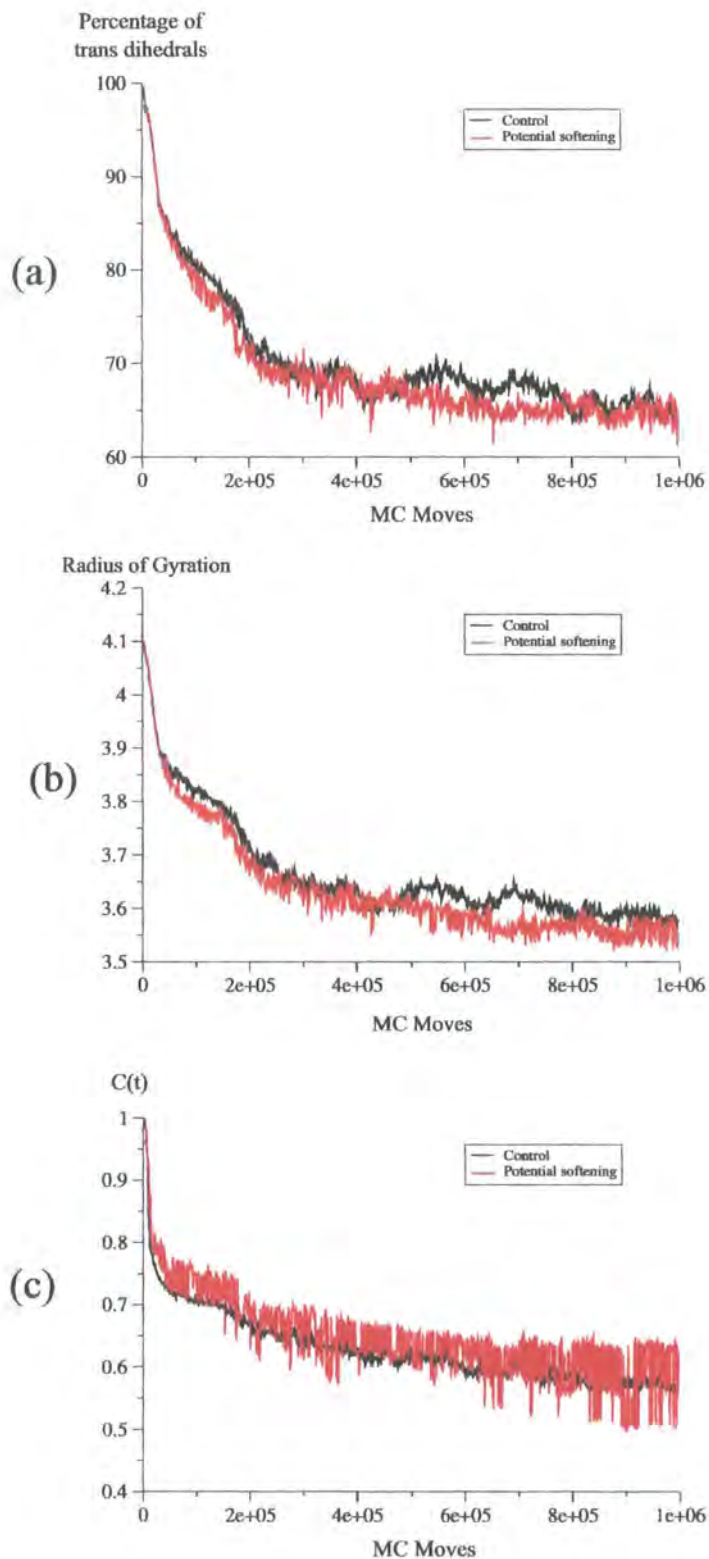
Figure 4.13: Results for the potential softening simulation of the undecane system with 64 replicas: (a) the percentage of trans dihedrals, (b) the radius of gyration and (c) the correlation function.
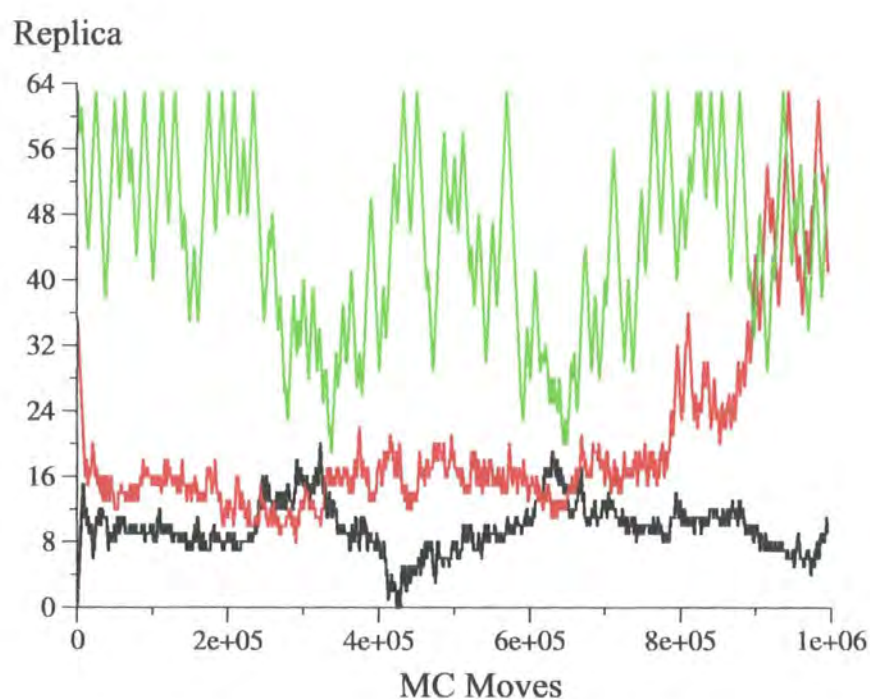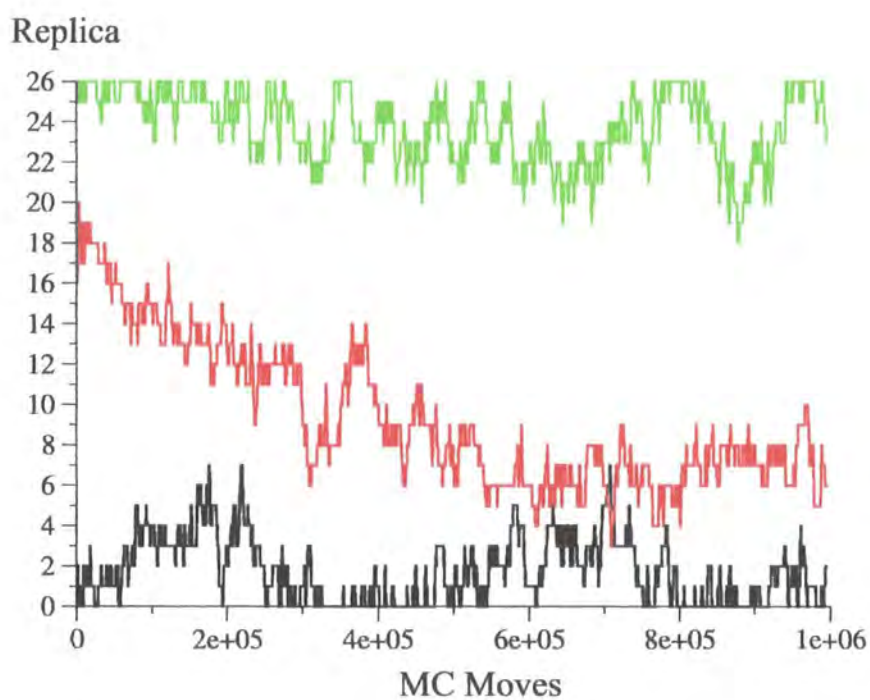
Replica

Replica

Figure 4.14: The path taken by three different replicas for the potential softening simulation of undecane: for a system with 27 replicas (top) and a system with 64 replicas (bottom).
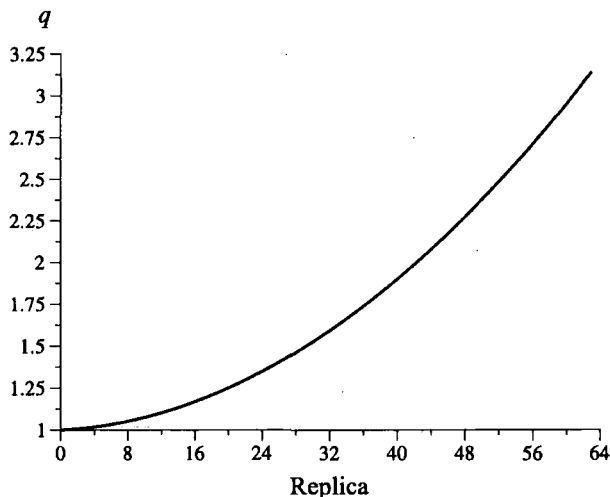
Figure 4.15: Diagram showing how q increases with respect to the 64 replica system.

forth. This is the reason for the extreme noise in the correlations functions.

Figure 4.14 shows the swapping of three replicas in both the 27 and 64 replica simulations, it shows quite clearly that the problem is that the ratio of swapping is much larger for systems with a high q value. Whereas for the parallel-tempered system each replica had swapped between a series of 10 or so temperatures, in the case of potential softening this behaviour remains true for the bottom replicas but the top replicas swap over a very large range. For the first two potentials in the 27 replica system, $q = 1.0$ and $q = 1.01$, the acceptance ratio is 18.46%, and for other potentials that had test runs done the ratio is also within the optimum 10-20% range. However, running test runs for all of the replicas defeats the one of primary purposes of extended ensembles methods in reducing the amount of computer time needed to run simulations. Figure 4.14 also shows that as q becomes larger the acceptance ratio between replicas increases as well, this is true despite the fact that for the 64 replica system q was chosen so that it increased exponentially (see figure 4.15).

4.4.2 Silsesquioxane Dendrimer

For the silsesquioxane dendrimer a 64 replica system was set up, however, the overlap between systems was so poor that the top replica was limited to $q = 1.09770$, still a
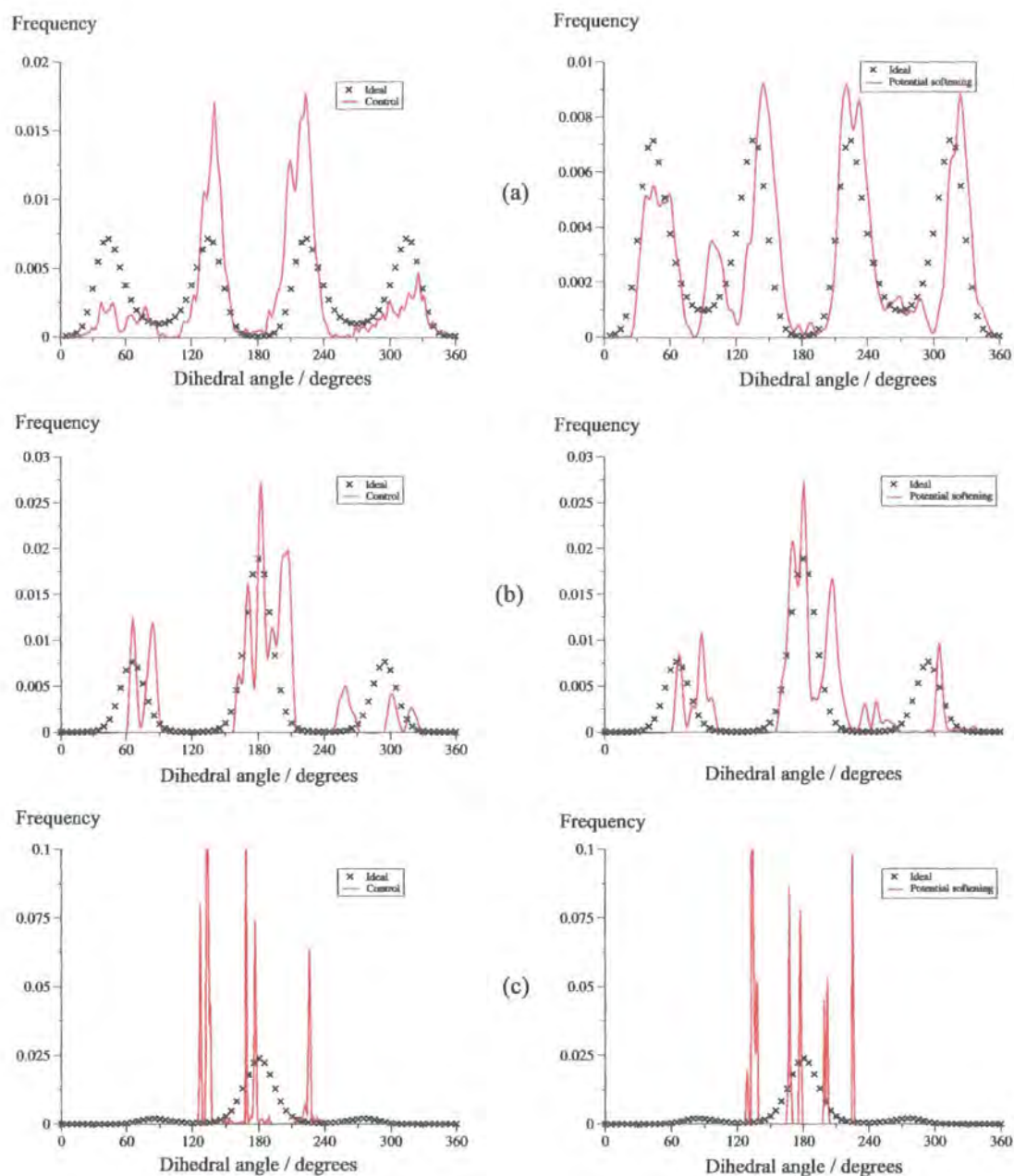
Figure 4.16: Dihedral distributions for three dihedrals in the dendrimer: (a) Si-C-C-Si dihedral between the central cage and the first branching point, (b) C-C-C-O dihedral of the linker connecting the mesogenic groups to core and (c) the biphenyl dihedral in the mesogenic groups. The crosses show the ideal distribution.
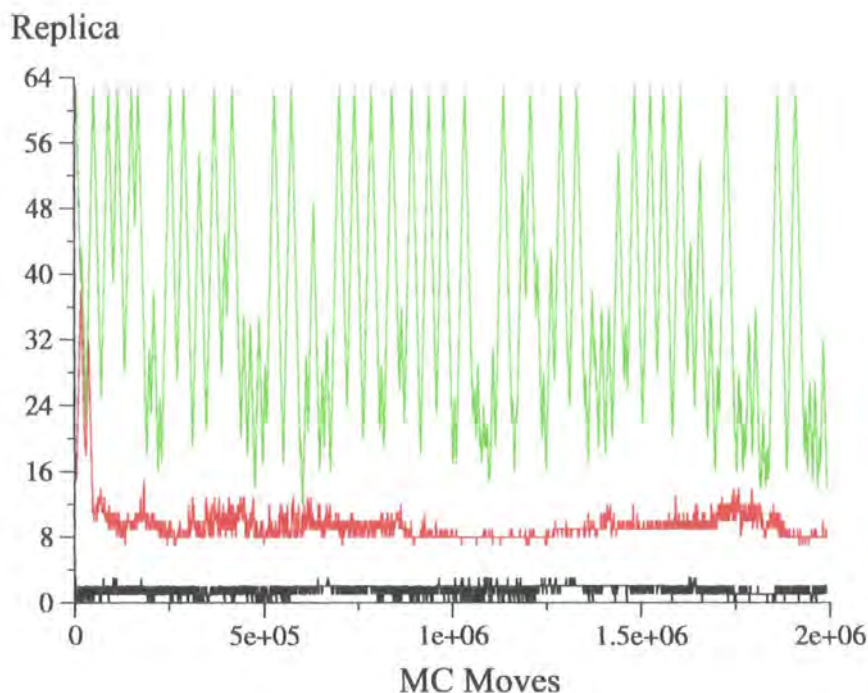
Replica

Figure 4.17: The path taken by three different replicas for the potential softening simulation of the silsesquioxane dendrimer.

relatively hard system. After a series of short test runs to give some initial estimates for the q values, the final values were chosen so that they increased exponentially. As with the parallel-tempered system the simulation was run for two million MC moves and replica swaps were attempted every 1000 MC moves.

Again dihedral distributions within the dendrimer were calculated in order to observe the effect potential softening had. Despite only reaching a top q value of 1.0977 the potential softening had a definite effect, and the effect of the potential softening seems to be greater than the effect of parallel-tempering. In particular potential softening does effect the inner dihedrals as well as the outer dihedrals.

While potential softening seems to have a greater effect on the dendrimer system than on the undecane chain system the major problem with swapping between the replicas remains. Figure 4.17 shows the same type of swapping behaviour that was seen for the undecane system. So while swapping between replicas at the bottom is appropriate, swapping between high replicas occurs far too often, meaning the overall acceptance ratio is 81.87%.

4.5 Conclusions

The results of extended ensemble simulations showed that sampling of phase space can be improved but that the effects of the method seem to be limited and there are a number of drawbacks to using the technique.

In the case of the alkane chain system the parallel-tempering did have an effect on the system. This effect was probably limited by the fact that the system reached equilibrium quickly simply using a normal Monte Carlo simulation. For a system which sampled phase space less efficiently, the effects of the parallel-tempering might have been increased. Running the same simulations with a series of longer alkane chains and observing how the effectiveness of parallel-tempering altered would give further valuable information about the usefulness of parallel-tempering. For the silsesquioxane system there was a minor improvement in the sampling of space phase when using parallel-tempering but the overall effect was limited.

The effectiveness of parallel-tempering is dependent on the system being simulated. For those systems that will reach an equilibrium state but the computational time required to reach such a state is too great (such as the coarse-grained dendrimer described in chapter 3 or a longer alkane chain) parallel-tempering could provide a valuable tool. However, for those systems, like the silsesquioxane dendrimer, where even at high temperatures the sampling of phase space remains quite poor, parallel-tempering is not an especially efficient use of computer time.

The potential softening method did not manage to achieve the desired effects. This is partly due to the problems with the excessive swapping between nodes described above. A greater number of test runs would enable a series of ensembles with a better swap ratio to be set up, but doing this by trial and error would require a large amount of computer time. A more efficient way would be to develop a program with a feedback loop that could alter the q values during a simulation so that the number of ensemble swaps made stayed close to 20% range. This would allow a short test run of the program to generate the correct q values that could be used in for the full simulation run.

Secondly the Tsallis potential may not be the best way to soften potentials for macromolecular systems, because even for the softest ensembles the non-bonded

interactions remained quite hard. Ways of softening the non-bonded forces are explored in the next chapter. Softening non-bonded interactions while at the same time using the Tsallis potential for the dihedrals may be a better approach for improving configurational sampling in simulations of macromolecules.

Chapter 5

Soft-Core Potentials

5.1 Introduction

One of the problems with the simulation of macromolecular liquid crystal systems is that the formation of mesophases can take place over very long timescales. For the coarse-grained dendrimer simulations in chapter 3 a uniformly aligned mesophase did not form spontaneously even after 35 ns of simulation. It would be helpful therefore if we could increase the speed at which mesophases form, reducing the amount of CPU time needed for simulations. This problem with timescales has prompted some recent work using dissipative particle dynamics (DPD) (section 2.3) to study liquid crystal phases.[107,108,156] In DPD models the nonbonded interaction force is a linear repulsive term, meaning that the potential has a quadratic form and a finite energy at zero separation, thus it it a *soft-core* potential. The nature of soft-core potentials allows considerably longer timesteps to be used in molecular dynamics simulations than those used for conventional models such as the Lennard-Jones potential. In addition the soft core nature of the potential reduces the time taken to move from one state point to the next. Allowing molecules to penetrate each other to a greater extent than with conventional potentials would address the problem we saw with the dendrimer in chapter 3, where the the high viscosity of the system meant that evolution of any mesophase could not take place on a realistic timescale. Liquid crystal systems have been studied using DPD potentials by using a series of spheres joined together by a classical spring force and the formation of

nematic and smectic-A mesophases was seen.[107] Mesophase formation has also been seen in a DPD simulations of di-block co-polymers.[156] However, it would be desirable to have a single site anisotropic soft-core model that could be used to model liquid crystals. Moreover, a better understanding of the nature of soft-core potentials would help identify a more effective way of softening the potentials themselves.

The work presented in this chapter consists of the development of three different soft-core potentials which are then tested on a series of spherocylinder systems in order to gain a better understanding of the advantages and disadvantages of the each model.

5.2 Soft-Core Potential Models

All three forms of soft-core potential used were modified versions of the SRS potential. The three different potentials are denoted as *tangential*, *perturbed* and *quadratic*.

For the tangential potential, U_{tan}, (Eqn. 5.1) a maximum energy value, U_{max}, is chosen and a straight line is draw to intersect with the SRS potential. The intersect, d_c, and the value of the potential at the intercept, U_c, are uniquely defined by matching the derivatives of the tangent and the SRS potential at the intercept. Therefore the tangential potential has the form

$$U_{\text{tan}} = \begin{cases} U_{\text{max}} - \frac{d_{ij}}{d_c}(U_{\text{max}} - U_c), & d_{ij} < d_c \\ 4\epsilon\left[\left(\frac{\sigma}{d_{ij}}\right)^{12} - \left(\frac{\sigma}{d_{ij}}\right)^6 + \frac{1}{4}\right], & d_c \leq d_{ij} < d_{cut} \\ 0, & d_{ij} \geq d_{cut} \end{cases} \quad (5.1)$$

The perturbed potential, U_{pert}, was derived from the work of van Gunsteren[94,157] and takes the form

$$U_{\text{pert}} = \begin{cases} 4\epsilon\left[\left(\frac{1}{c+\left(\frac{d_{ij}}{\sigma}\right)^6}\right)^2 - \frac{1}{c+\left(\frac{d_{ij}}{\sigma}\right)^6} + \frac{1}{4}\right], & d_{ij} < d_{cut} \\ 0, & d_{ij} \geq d_{cut} \end{cases} \quad (5.2)$$

the normal SRS potential is modified by adding a softening parameter c that causes

the potential to have a finite energy value of $U_{\max}/\varepsilon = 4/c^2 - 4/c + 1$. To ensure that the potential goes smoothly to zero the cutoff is modified from the SRS cutoff of $d_{cut} = 2^{\frac{1}{6}}\sigma$ to $d_{cut} = (2 - c)^{1/6}\sigma$.

The quadratic potential, U_{quad}, is equivalent to the types of potentials used in DPD simulations. Here a parameter, a, determines how soft the potential is, as shown in the expression below

$$U_{\text{quad}} = \begin{cases} \frac{a\varepsilon}{2}\left(1 - \frac{d_{ij}}{d_{cut}}\right)^2, & d_{ij} < d_{cut} \\ 0, & d_{ij} \geq d_{cut} \end{cases}, \tag{5.3}$$

for the quadratic potential the cutoff is set at $d_{cut} = \sigma$.

The different forms of the softened potentials, as well as the SRS potential, are shown in figure 5.1, here all the potentials have been given the same $U_{\max}$ so that they can be compared easily. All three models are continuous meaning that they can be used in molecular dynamics simulations as well as with Monte Carlo.

5.3 Spherocylinder With Aspect Ratio $L/D = 5$

5.3.1 Simulation Details

To test the different potentials and see which, if any, could be used to model liquid crystal systems, a series of simple Monte Carlo simulations of 1024 spherocylinders were run. The spherocylinders had an aspect ratio of $L/D = 5$ and the system was set to have $\sigma = D = \varepsilon = 1$. Simulation runs were carried out in the NpT ensemble and used cubic periodic boundary conditions. Simulation runs were carried out at three reduced temperatures, at $T^* = 1.0$, $T^* = 2.0$ and $T^* = 5.0$ ($T^* = kT/\varepsilon$).

For the $T^* = 1.0$ system a total of seven different potentials were used in addition to a run carried out with the normal SRS potential to act as a comparison. These can be summarised as;

1. the normal SRS potential,

2. a tangential potential with $U_{\max}^* = 10$,

3. a perturbed potential with $c = 2/3$ and $U_{\max}^* = 4$,
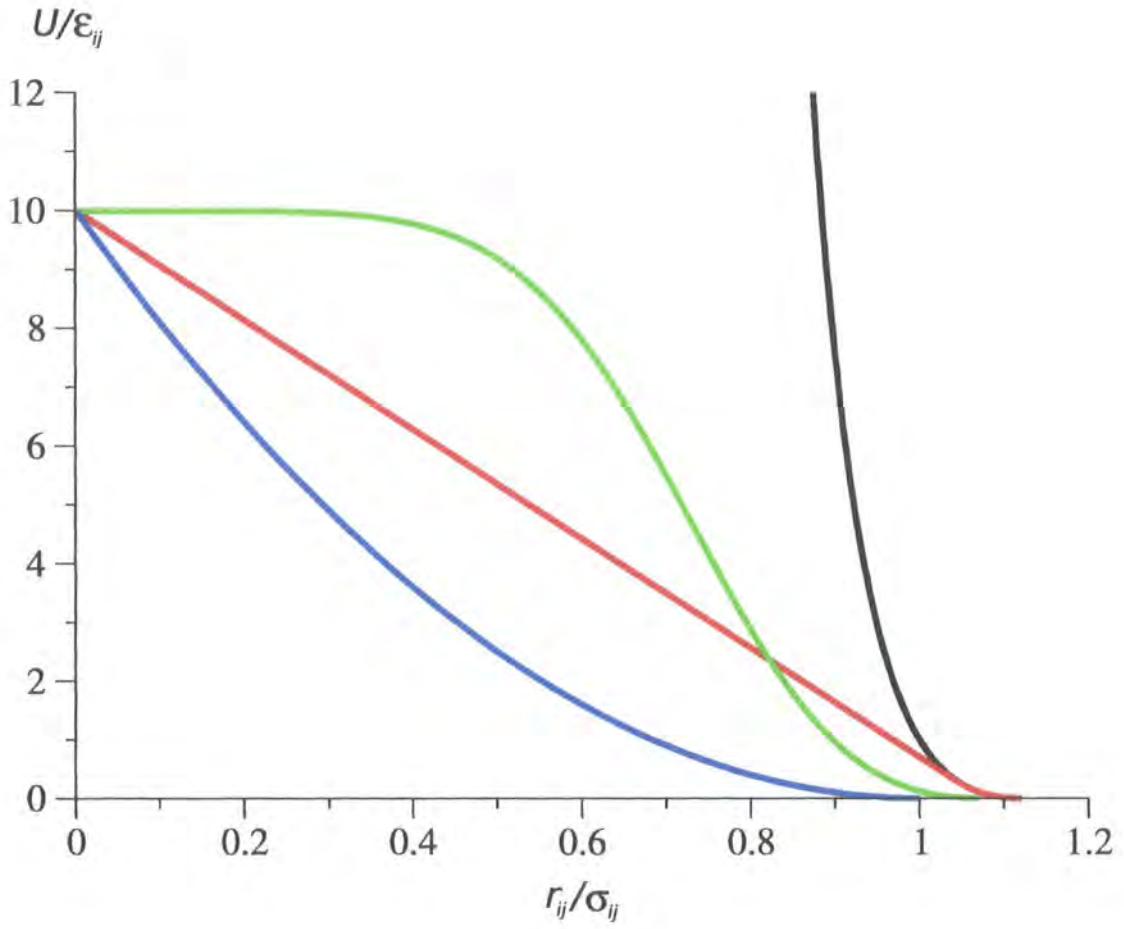
Figure 5.1: Potentials of the normal SRS potential (black), the tangential potential (red), the perturbed potential (green) and the quadratic potential (blue).

4. a perturbed potential with $c = 0.44096$ and $U^*_{\max} = 12.5$,

5. a quadratic potential with $a = 8$ and $U^*_{\max} = 4$,

6. a quadratic potential with $a = 11$ and $U^*_{\max} = 5.5$,

7. a quadratic potential with $a = 70$ and $U^*_{\max} = 35$,

where $U^*_{\max} = U_{\max}/\varepsilon$. For the runs at $T^* = 2.0$ and $T^* = 5.0$ only potentials 2, 3, and 7 were used. In addition a series of NVT runs at different densities were carried out using potential 2.

The simulation runs were 10240000 trial moves with a box move attempted (and data dumped) every 1024 trial moves. Results were averaged over the last 10000 cycles (10240000 MC moves).

5.3.2 Results and Discussion

The results for the runs are laid out in tables 5.1-5.12 and the phase diagrams for the different temperatures and potentials are given in figures 5.2-5.13. The results are presented using reduced units where the reduced density is $\rho^* = \rho\sigma^3$, the reduced pressure $P^* = P.\sigma^3/kT$ and the reduced energy is $U^* = U/\varepsilon N$.

For all of the soft-core potentials liquid crystalline phase behavior was seen, with a nematic LC phase forming in every simulation regardless of the temperature and potential used. The nematic phases formed by the soft-core potentials resemble those formed by the SRS potential quite closely, though the phase changes are shifted to higher densities (as one would expect for softer systems). With respect to smectic phases the picture is more complicated, as at the densities that the "smectic" phases form the overlap of particles is now quite large. It is apparent from the pressure-density phase diagrams, however, that there are phases changes for a number of systems and snapshots of the systems (figures 5.15c and 5.17c) show layered phases. From the snapshot, the layered phase formed by the quadratic model, figure 5.17c, appears to a smectic-C phase, however, this is probably due to the fact that the system was compressed isotropically. If the box sides were allowed to move independently then the system will most likely relax to a smectic-A phase.

P^*	$\langle\rho^*\rangle$	$\langle U^*\rangle$	$\langle S_2\rangle$	Phase
0.100	0.0327 ± 0.0005	0.12 ± 0.01	0.029 ± 0.011	I
0.150	0.0397 ± 0.0006	0.17 ± 0.01	0.032 ± 0.014	I
0.200	0.0452 ± 0.0006	0.21 ± 0.01	0.026 ± 0.009	I
0.250	0.0498 ± 0.0006	0.25 ± 0.02	0.28 ± 0.011	I
0.500	0.0650 ± 0.0011	0.43 ± 0.02	0.035 ± 0.013	I
0.750	0.0751 ± 0.0009	0.59 ± 0.03	0.032 ± 0.006	I
1.000	0.0829 ± 0.0008	0.74 ± 0.03	0.037 ± 0.005	I
1.125	0.0865 ± 0.0006	0.82 ± 0.03	0.109 ± 0.036	I
1.250	0.0928 ± 0.0004	0.89 ± 0.03	0.545 ± 0.013	N
1.375	0.0969 ± 0.0004	0.96 ± 0.03	0.711 ± 0.006	N
1.500	0.0999 ± 0.0004	1.03 ± 0.03	0.768 ± 0.009	N
1.750	0.1063 ± 0.0004	1.18 ± 0.04	0.840 ± 0.005	N
2.000	0.1100 ± 0.0004	1.33 ± 0.04	0.866 ± 0.007	N
2.250	0.1143 ± 0.0004	1.49 ± 0.04	0.878 ± 0.004	N
2.500	0.1176 ± 0.0005	1.62 ± 0.04	0.910 ± 0.001	N
2.750	0.1205 ± 0.0004	1.78 ± 0.04	0.908 ± 0.004	N
3.000	0.1234 ± 0.0004	1.92 ± 0.05	0.920 ± 0.001	N

Table 5.1: Results for the simulation run with SRS potential at $T^* = 1.0$.

P^*	$\langle\rho^*\rangle$	$\langle U^*\rangle$	$\langle S_2\rangle$	Phase
0.100	0.0340 ± 0.0006	0.34 ± 0.02	0.029 ± 0.010	I
0.150	0.0416 ± 0.0006	0.49 ± 0.02	0.029 ± 0.010	I
0.200	0.477 ± 0.0004	0.62 ± 0.03	0.028 ± 0.009	I
0.250	0.0527 ± 0.0005	$0.75\pm0.0.04$	0.030 ± 0.011	I
0.500	0.0710 ± 0.0005	1.41 ± 0.05	0.038 ± 0.011	I
0.750	0.0845 ± 0.0006	2.12 ± 0.06	0.039 ± 0.015	I
1.000	0.0993 ± 0.0009	2.90 ± 0.07	0.140 ± 0.041	I
1.125	0.1112 ± 0.0008	3.34 ± 0.07	0.659 ± 0.020	N
1.250	0.1210 ± 0.0009	3.75 ± 0.07	0.798 ± 0.010	N
1.375	0.1292 ± 0.0010	4.14 ± 0.07	0.813 ± 0.013	N
1.500	0.1372 ± 0.0012	4.49 ± 0.08	0.855 ± 0.016	N
1.750	0.1534 ± 0.0013	5.11 ± 0.08	0.896 ± 0.005	N
2.000	0.1762 ± 0.0016	5.57 ± 0.07	0.951 ± 0.005	SmA
2.250	0.1925 ± 0.0014	5.95 ± 0.07	0.968 ± 0.005	SmA
2.500	0.2058 ± 0.0013	6.37 ± 0.07	0.971 ± 0.004	SmA
2.750	0.2180 ± 0.0018	6.77 ± 0.08	0.979 ± 0.003	SmA
3.000	0.2301 ± 0.0020	7.23 ± 0.08	0.980 ± 0.004	SmA

Table 5.2: Results for the simulation run with the tangential potential, $U^*_{\max} = 10$, at $T^* = 1.0$.

P^*	$\langle \rho^* \rangle$	$\langle U^* \rangle$	$\langle S_2 \rangle$	Phase
0.125	0.0423 ± 0.0006	1.41 ± 0.07	0.029 ± 0.011	I
0.250	0.0602 ± 0.0006	2.50 ± 0.12	0.031 ± 0.011	I
0.375	0.0738 ± 0.0007	3.54 ± 0.10	0.033 ± 0.011	I
0.500	0.0851 ± 0.0007	4.47 ± 0.11	0.040 ± 0.013	I
0.625	0.0953 ± 0.0008	5.36 ± 0.12	0.045 ± 0.015	I
0.750	0.1050 ± 0.0009	6.17 ± 0.12	0.044 ± 0.018	I
0.875	0.1145 ± 0.0010	6.89 ± 0.13	0.058 ± 0.020	I
1.000	0.1241 ± 0.0011	7.55 ± 0.13	0.104 ± 0.031	I
1.125	0.1410 ± 0.0013	7.99 ± 0.13	0.639 ± 0.027	N
1.250	0.1539 ± 0.0014	8.49 ± 0.13	0.751 ± 0.022	N
1.375	0.1652 ± 0.0017	8.99 ± 0.13	0.797 ± 0.020	N
1.500	0.1760 ± 0.016	9.44 ± 0.14	0.841 ± 0.011	N
1.625	0.1867 ± 0.0015	9.87 ± 0.13	0.877 ± 0.010	N
1.750	0.1983 ± 0.0017	10.20 ± 0.14	0.902 ± 0.008	N
1.875	0.2152 ± 0.0019	10.33 ± 0.13	0.930 ± 0.006	SmA
2.000	0.2281 ± 0.0021	10.59 ± 0.14	0.946 ± 0.005	SmA
2.125	0.2381 ± 0.0022	10.91 ± 0.13	0.952 ± 0.005	SmA
2.250	0.2485 ± 0.0023	11.19 ± 0.14	0.957 ± 0.005	SmA
2.375	0.2589 ± 0.0022	11.49 ± 0.15	0.961 ± 0.005	SmA
2.500	0.2683 ± 0.0022	12.10 ± 0.13	0.966 ± 0.006	SmA
2.625	0.2760 ± 0.0022	12.11 ± 0.14	0.970 ± 0.002	SmA
2.750	0.2847 ± 0.0022	12.42 ± 0.13	0.969 ± 0.004	SmA

Table 5.3: Results for the simulation run with the tangential potential, $U^*_{\mathrm{max}} = 10$, at $T^* = 2.0$.

P^*	$\langle \rho^* \rangle$	$\langle U^* \rangle$	$\langle S_2 \rangle$	Phase
0.6	0.1287±0.0014	13.22±0.22	0.035±0.013	I
0.7	0.1399±0.0014	14.63±0.23	0.037±0.014	I
0.8	0.1508±0.0015	16.03±0.25	0.039±0.014	I
0.9	0.1602±0.0015	17.16±0.25	0.042±0.015	I
1.0	0.1695±0.0016	18.33±0.27	0.045±0.017	I
1.1	0.1786±0.0017	19.41±0.28	0.047±0.017	I
1.2	0.1873±0.0017	10.46±0.28	0.053±0.019	I
1.3	0.1960±0.0018	21.41±0.29	0.062±0.021	I
1.4	0.2043±0.0019	22.31±0.30	0.069±0.026	I
1.5	0.2131±0.0020	23.13±0.31	0.085±0.035	I
1.6	0.2361±0.0033	22.57±0.36	0.616±0.056	N
1.7	0.2517±0.0029	22.76±0.31	0.724±0.023	N
1.8	0.2646±0.0028	23.15±0.31	0.777±0.016	N
1.9	0.2752±0.0030	23.68±0.31	0.797±0.017	N
2.0	0.2861±0.0029	24.15±0.30	0.826±0.014	N
2.1	0.2971±0.0029	24.63±0.31	0.847±0.011	N
2.2	0.3072±0.0031	25.13±0.31	0.858±0.010	N
2.3	0.3159±0.0030	25.66±0.31	0.869±0.009	N
2.4	0.3259±0.0032	26.14±0.30	0.881±0.009	N
2.5	0.3354±0.0031	26.57±0.31	0.893±0.008	N
2.6	0.3459±0.0034	26.97±0.32	0.900±0.009	N
2.8	0.3644±0.0035	27.81±0.32	0.916±0.008	N
3.0	0.3837±0.0037	28.53±0.34	0.928±0.006	N
3.2	0.4034±0.0038	29.04±0.33	0.941±0.005	N
3.4	0.4214±0.0040	29.56±0.33	0.949±0.004	N

Table 5.4: Results for the simulation run with the tangential potential, $U^*_{\max} = 10$, at $T^* = 5.0$.

P^*	$\langle \rho^* \rangle$	$\langle U^* \rangle$	$\langle S_2 \rangle$	Phase
0.100	0.0378±0.0007	0.40 ± 0.03	0.029 ± 0.010	I
0.150	0.0473±0.0007	0.57±0.03	0.029±0.011	I
0.200	0.0546±0.0007	0.73±0.04	0.028±0.009	I
0.250	0.0609±0.0007	0.89±0.04	0.032±0.010	I
0.500	0.0850±0.0013	1.69±0.06	0.037±0.012	I
0.750	0.1049±0.0011	2.42±0.06	0.059±0.017	I
1.000	0.1247±0.0012	3.05±0.07	0.057±0.017	I
1.125	0.1357±0.0012	3.30±0.06	0.103±0.030	I
1.250	0.1541±0.0014	3.51±0.06	0.679±0.015	N
1.375	0.1664±0.0016	3.70±0.06	0.760±0.015	N
1.500	0.1798±0.0015	3.90±0.07	0.829±0.015	N
1.750	0.2028±0.0019	4.23±0.07	0.880±0.010	N
2.000	0.2307±0.0021	4.50±0.07	0.916±0.009	N
2.250	0.2544±0.0023	4.75±0.07	0.940±0.002	N
2.500	0.2784±0.0024	4.97±0.06	0.957±0.005	N
2.750	0.2981±0.0023	5.25±0.06	0.960±0.004	N
3.000	0.3246±0.0029	5.58 ± 0.06	0.970±0.004	N
3.500	0.3741±0.0017	5.55±0.05	0.990±0.000	K
4.000	0.3951±0.0024	5.69±0.05	0.990±0.000	K
4.500	0.4115±0.0024	5.71±0.05	0.990±0.000	K

Table 5.5: Results for the simulation run with the perturbed potential, $U^*_{\max} = 4$, $c = (2/3)$, at $T^* = 1.0$.

P^*	$\langle \rho^* \rangle$	$\langle U^* \rangle$	$\langle S_2 \rangle$	Phase
0.125	0.0423±0.0007	1.55 ± 0.06	0.028 ± 0.010	I
0.250	0.0723 ± 0.0009	2.67±0.08	0.031±0.011	I
0.375	0.0904±0.0010	3.62±0.09	0.033±0.012	I
0.500	0.1053±0.0011	4.46±0.09	0.033±0.012	I
0.625	0.1186±0.0012	5.23±0.10	0.037±0.015	I
0.750	0.1301±0.0012	5.92 ± 0.11	0.043±0.016	I
0.875	0.1420±0.0013	6.56±0.11	0.042±0.016	I
1.000	0.1528±0.0014	7.13±0.12	0.056±0.019	I
1.125	0.1634±0.0015	7.65±0.12	0.058±0.022	I
1.250	0.1741±0.0016	8.10±0.13	0.073±0.025	I
1.300	0.1788±0.0016	8.25±0.13	0.071±0.030	I
1.3375	0.1825±0.0016	8.33±0.13	0.114±0.034	I
1.350	0.1838±0.0017	8.38±0.13	0.127±0.034	I
1.375	0.1866±0.0017	8.43±0.14	0.120±0.041	I
1.500	0.2135±0.0023	8.31±0.13	0.734±0.021	N
1.625	0.2273±0.0025	8.58±0.13	0.788±0.018	N
1.750	0.2408±0.0024	8.84±0.13	0.819±0.013	N
1.875	0.2536±0.0027	9.09±0.14	0.851±0.012	N
2.000	0.2663±0.0027	9.33±0.13	0.869±0.010	N
2.125	0.2783±0.0024	9.56±0.13	0.886±0.008	N
2.250	0.2917±0.0029	9.75±0.13	0.895±0.008	N
2.375	0.3077±0.0032	9.92±0.14	0.916±0.007	N
2.500	0.3255±0.0038	10.03±0.14	0.929±0.007	N
2.625	0.3433±0.0037	9.90±0.14	0.940±0.008	N
2.750	0.3620±0.0042	10.11±0.14	0.953±0.006	N

Table 5.6: Results for the simulation run with the perturbed potential, $U^*_{\max} = 4$, $c = (2/3)$, at $T^* = 2.0$.

P^*	$\langle \rho^* \rangle$	$\langle U^* \rangle$	$\langle S_2 \rangle$	Phase
0.6	0.1621 ± 0.0019	10.94 ± 0.18	0.032 ± 0.011	I
0.7	0.1768 ± 0.0021	12.06 ± 0.20	0.033 ± 0.012	I
0.8	0.1904 ± 0.0021	13.12 ± 0.20	0.034 ± 0.012	I
0.9	0.2033 ± 0.0022	14.11 ± 0.21	0.034 ± 0.013	I
1.0	0.2153 ± 0.0024	15.05 ± 0.22	0.036 ± 0.013	I
1.1	0.2270 ± 0.0024	15.95 ± 0.22	0.037 ± 0.014	I
1.2	0.2381 ± 0.0025	16.81 ± 0.24	0.039 ± 0.014	I
1.3	0.2487 ± 0.0025	17.64 ± 0.23	0.040 ± 0.015	I
1.4	0.2591 ± 0.0025	18.43 ± 0.24	0.042 ± 0.016	I
1.5	0.2689 ± 0.0027	19.18 ± 0.25	0.043 ± 0.016	I
1.6	0.2785 ± 0.0027	19.92 ± 0.25	0.046 ± 0.017	I
1.7	0.2880 ± 0.0028	20.62 ± 0.26	0.049 ± 0.019	I
1.8	0.2972 ± 0.0028	21.31 ± 0.26	0.052 ± 0.019	I
1.9	0.3063 ± 0.0028	21.98 ± 0.26	0.053 ± 0.020	I
2.0	0.3149 ± 0.0029	22.61 ± 0.27	0.059 ± 0.023	I
2.1	0.3236 ± 0.0030	23.25 ± 0.28	0.060 ± 0.023	I
2.2	0.3320 ± 0.0030	23.84 ± 0.28	0.067 ± 0.027	I
2.3	0.3407 ± 0.0032	24.40 ± 0.30	0.078 ± 0.031	I
2.4	0.3492 ± 0.0033	24.91 ± 0.30	0.096 ± 0.043	I
2.5	0.3896 ± 0.0046	23.20 ± 0.33	0.672 ± 0.027	N
2.6	0.4047 ± 0.0044	23.32 ± 0.32	0.724 ± 0.019	N
2.8	0.4310 ± 0.0048	23.65 ± 0.34	0.788 ± 0.016	N
3.0	0.4543 ± 0.0047	24.28 ± 0.34	0.815 ± 0.013	N
3.2	0.4746 ± 0.0049	25.23 ± 0.36	0.842 ± 0.013	N

Table 5.7: Results for the simulation run with the perturbed potential, $U^*_{\text{max}} = 4$, $c = (2/3)$, at $T^* = 5.0$.

P^*	$\langle\rho^*\rangle$	$\langle U^*\rangle$	$\langle S_2\rangle$	Phase
0.100	0.0350±0.0006	0.19 ± 0.02	0.031 ± 0.011	I
0.150	0.0432±0.0007	0.27±0.02	0.030±0.010	I
0.200	0.0494±0.0006	0.33±0.02	0.029±0.011	I
0.250	0.0546±0.0006	0.40±0.02	0.030±0.011	I
0.500	0.0728±0.0010	0.69±0.03	0.030±0.010	I
0.750	0.0850±0.0008	0.97±0.04	0.036±0.008	I
1.000	0.0951±0.0007	1.23±0.04	0.036±0.012	I
1.125	0.1002±0.0006	1.38±0.05	0.122±0.020	I
1.250	0.1084±0.0006	1.51±0.05	0.622±0.010	N
1.375	0.1134±0.0007	1.68±0.05	0.703±0.008	N
1.500	0.1190±0.0007	1.87±0.06	0.797±0.008	N
1.750	0.1290±0.0007	2.35±0.07	0.867±0.008	N
2.000	0.1410±0.0010	3.07±0.12	0.908±0.007	N
2.250	0.1563±0.0010	3.95±0.09	0.941±0.004	N
2.500	0.1694±0.0010	4.81±0.09	0.941±0.005	N
2.750	0.1890±0.0018	5.94±0.11	0.936±0.005	N
3.000	0.2097 ± 0.0011	6.74±0.05	0.949±0.004	K
3.500	0.2313±0.017	7.37±0.05	0.955±0.005	K

Table 5.8: Results for the simulation run with the perturbed potential, $U^*_{\max} = 12.5$, $c = (0.44096)$, at $T^* = 1.0$.

P^*	$\langle\rho^*\rangle$	$\langle U^*\rangle$	$\langle S_2\rangle$	Phase
0.100	0.0484 ± 0.0011	0.49 ± 0.02	0.030 ± 0.012	I
0.150	0.0631±0.0011	0.68±0.03	0.029±0.011	I
0.200	0.0746±0.0011	0.84±0.03	0.029±0.010	I
0.250	0.0846±0.0012	1.00±0.03	0.030±0.011	I
0.500	0.1232±0.0020	1.66±0.05	0.030±0.011	I
0.750	0.1526±0.0015	2.23±0.05	0.040±0.014	I
1.000	0.1774±0.0017	2.72±0.05	0.044±0.014	I
1.125	0.1888±0.0018	2.94±0.05	0.044±0.016	I
1.250	0.2001±0.0018	3.15±0.05	0.057±0.016	I
1.375	0.2111±0.0020	3.34±0.06	0.064±0.027	I
1.500	0.2225±0.0021	3.51±0.06	0.096±0.034	I
1.750	0.2748±0.0029	3.54±0.06	0.775±0.015	N
2.000	0.3047±0.0034	3.77±0.06	0.829±0.014	N
2.250	0.3317±0.0033	4.01±0.06	0.874±0.009	N
2.500	0.3568±0.0036	4.24±0.06	0.897±0.007	N
2.750	0.3804±0.0035	4.45±0.06	0.915±0.006	N
3.000	0.4045±0.0037	4.65±0.06	0.929±0.006	N

Table 5.9: Results for the simulation run with the quadratic potential, $a = 8$, $U^*_{\max} = 4$, at $T^* = 1.0$.

P^*	$\langle \rho^* \rangle$	$\langle U^* \rangle$	$\langle S_2 \rangle$	Phase
0.100	0.0463 ± 0.0011	0.46 ± 0.02	0.029 ± 0.011	I
0.150	0.0590 ± 0.0011	0.63 ± 0.03	0.028 ± 0.10	I
0.200	0.0694 ± 0.0009	0.79 ± 0.03	0.028 ± 0.010	I
0.250	0.0784 ± 0.0010	0.94 ± 0.03	0.030 ± 0.011	I
0.500	0.1125 ± 0.0016	1.60 ± 0.05	0.035 ± 0.012	I
0.750	0.1382 ± 0.0015	2.16 ± 0.05	0.037 ± 0.011	I
1.000	0.1601 ± 0.0014	2.67 ± 0.05	0.054 ± 0.016	I
1.125	0.1707 ± 0.0015	2.89 ± 0.06	0.054 ± 0.018	I
1.250	0.1818 ± 0.0016	3.10 ± 0.05	0.088 ± 0.023	I
1.375	0.1930 ± 0.0019	3.28 ± 0.06	0.192 ± 0.022	I
1.500	0.2235 ± 0.0023	3.29 ± 0.06	0.746 ± 0.17	N
1.750	0.2513 ± 0.0025	3.59 ± 0.06	0.817 ± 0.015	N
2.000	0.2760 ± 0.0026	3.88 ± 0.06	0.860 ± 0.012	N
2.250	0.2997 ± 0.0029	4.16 ± 0.06	0.897 ± 0.008	N
2.500	0.3215 ± 0.0029	4.41 ± 0.06	0.915 ± 0.008	N
2.750	0.3450 ± 0.0031	4.65 ± 0.06	0.932 ± 0.006	N
3.000	0.3673 ± 0.0034	4.86 ± 0.06	0.943 ± 0.005	N

Table 5.10: Results for the simulation run with the quadratic potential, $a = 11$, $U^*_{\text{max}} = 5.5$, at $T^* = 1.0$.

Neither of the perturbed potentials formed a smectic phase but there is another phase change at very high densities to a system that is best described as crystalline (K) due to the extremely high order and lack of motion present in the system, It is still possible, however, to compress these crystalline systems further, usually by increasing particle energy.

From comparison of the different potentials from the results of the simulations carried out at $T^* = 1.0$ it is clear (figure 5.3) that the quadratic potential leads to a much softer potential with the I-N phase change occurring at much larger densities than for a perturbed potential with the same U^*_{max} value (potentials 3 and 5). Also interesting is that at $T^* = 1.0$ potential 7 is softer than potential 2 (figure 5.3), at $T^* = 2.0$ the two systems order-density plots overlay each other, while at $T^* = 5.0$ the quadratic potential is the softer one.   Thus as the temperature increases the softness of the two systems swaps. Despite this the shape of the phase diagrams for the soft-core potentials are remarkably similar to those given by the SRS potential. One noticeable difference is that even in systems at a high density a small increase in pressure will give quite a large increase in density leading to a long tail in the

P^*	$\langle \rho^* \rangle$	$\langle U^* \rangle$	$\langle S_2 \rangle$	Phase
0.100	0.0377 ± 0.0005	0.22 ± 0.03	0.027 ± 0.010	I
0.150	0.0456 ± 0.0006	0.35 ± 0.04	0.039 ± 0.013	I
0.200	0.0535 ± 0.0006	0.39 ± 0.03	0.029 ± 0.011	I
0.250	0.0594 ± 0.0006	0.47 ± 0.03	0.030 ± 0.011	I
0.500	0.0804 ± 0.0007	0.81 ± 0.03	0.035 ± 0.013	I
0.750	0.0948 ± 0.0007	1.13 ± 0.04	0.051 ± 0.013	I
1.000	0.1072 ± 0.0007	1.14 ± 0.04	0.091 ± 0.014	I
1.125	0.1131 ± 0.0007	1.59 ± 0.05	0.101 ± 0.022	I
1.250	0.1218 ± 0.0009	1.74 ± 0.05	0.523 ± 0.027	N
1.375	0.1300 ± 0.0008	1.90 ± 0.05	0.695 ± 0.025	N
1.500	0.1366 ± 0.0009	2.06 ± 0.06	0.792 ± 0.010	N
1.750	0.1476 ± 0.0009	2.38 ± 0.06	0.871 ± 0.007	N
2.000	0.1576 ± 0.0009	2.72 ± 0.06	0.905 ± 0.005	N
2.250	0.1669 ± 0.0011	3.03 ± 0.07	0.926 ± 0.006	N
2.500	0.1759 ± 0.0009	3.31 ± 0.07	0.944 ± 0.006	N
2.750	0.1824 ± 0.0009	3.58 ± 0.07	0.951 ± 0.002	N
3.000	0.1929 ± 0.0012	4.03 ± 0.07	0.959 ± 0.003	N
3.500	0.2019 ± 0.0011	4.36 ± 0.08	0.970 ± 0.001	N
4.000	0.2094 ± 0.0010	4.65 ± 0.08	0.977 ± 0.004	N
4.500	0.2166 ± 0.0020	4.92 ± 0.09	0.978 ± 0.004	N

Table 5.11: Results for the simulation run with the quadratic potential, $a = 70$, $U^*_{\max} = 35$, at $T^* = 1.0$.

P^*	$\langle \rho^* \rangle$	$\langle U^* \rangle$	$\langle S_2 \rangle$	Phase
0.125	0.0451±0.0006	0.72 ± 0.04	0.028 ± 0.011	I
0.250	0.0640±0.0007	1.26±0.06	0.031±0.012	I
0.375	0.0773±0.0008	1.74±0.07	0.033±0.012	I
0.500	0.0880±0.0008	2.19±0.08	0.037±0.011	I
0.625	0.0971±0.0008	2.62±0.08	0.040±0.012	I
0.750	0.1051±0.0008	3.06±0.10	0.053±0.019	I
0.875	0.1127±0.0008	3.47±0.09	0.040±0.016	I
1.000	0.1200±0.0009	3.89±0.10	0.050±0.014	I
1.125	0.1273±0.0009	4.29±0.11	0.095±0.026	I
1.250	0.1410±0.0011	4.66±0.11	0.610±0.022	N
1.300	0.1450±0.0011	4.83±0.11	0.657±0.018	N
1.375	0.1511±0.0012	5.08±0.11	0.743±0.017	N
1.500	0.1592±0.0012	5.50±0.12	0.785±0.011	N
1.625	0.1667±0.0013	5.90±0.12	0.823±0.018	N
1.750	0.1740±0.0012	6.34±0.12	0.847±0.010	N
1.875	0.1812±0.0013	6.73±0.13	0.874±0.010	N
2.000	0.1881±0.0013	7.14±0.13	0.888±0.008	N
2.125	0.1949±0.0015	7.53±0.13	0.903±0.007	N
2.250	0.2018±0.0015	7.95±0.14	0.913±0.007	N
2.375	0.2085±0.0016	8.35±0.15	0.909±0.007	N
2.500	0.2145±0.0018	8.71±0.14	0.932±0.005	N
2.625	0.2214±0.0016	9.10±0.15	0.938±0.004	N
2.750	0.2299±0.0016	9.46±0.15	0.946±0.006	N
3.000	0.2566±0.0018	9.84±0.14	0.971±0.003	SmA
3.250	0.2692±0.0018	10.50±0.14	0.977±0.004	SmA

Table 5.12: Results for the simulation run with the quadratic potential, $a = 70$, $U_{\text{max}}^* = 35$, at $T^* = 2.0$.

P^*	$\langle \rho^* \rangle$	$\langle U^* \rangle$	$\langle S_2 \rangle$	Phase
0.6	0.1157 ± 0.0011	8.70 ± 0.23	0.031 ± 0.011	I
0.7	0.1249 ± 0.0012	9.82 ± 0.24	0.038 ± 0.015	I
0.8	0.1335 ± 0.0012	10.86 ± 0.25	0.039 ± 0.014	I
0.9	0.1417 ± 0.0013	11.88 ± 0.25	0.041 ± 0.014	I
1.0	0.1494 ± 0.0012	12.82 ± 0.27	0.052 ± 0.016	I
1.1	0.1575 ± 0.0014	13.77 ± 0.27	0.047 ± 0.014	I
1.2	0.1655 ± 0.0014	14.62 ± 0.29	0.055 ± 0.015	I
1.3	0.1743 ± 0.0016	15.40 ± 0.29	0.097 ± 0.022	I
1.4	0.1961 ± 0.0021	15.67 ± 0.28	0.676 ± 0.023	N
1.5	0.2090 ± 0.0021	16.32 ± 0.29	0.773 ± 0.017	N
1.6	0.2187 ± 0.0023	17.01 ± 0.28	0.786 ± 0.017	N
1.7	0.2288 ± 0.0022	17.66 ± 0.29	0.828 ± 0.013	N
1.8	0.2379 ± 0.0024	18.36 ± 0.31	0.841 ± 0.015	N
1.9	0.2469 ± 0.0022	19.00 ± 0.29	0.863 ± 0.011	N
2.0	0.2561 ± 0.0023	19.63 ± 0.31	0.883 ± 0.008	N
2.1	0.2646 ± 0.0024	20.86 ± 0.31	0.897 ± 0.008	N
2.2	0.2729 ± 0.0023	21.48 ± 0.31	0.903 ± 0.007	N
2.3	0.2808 ± 0.0026	21.48 ± 0.31	0.910 ± 0.009	N
2.4	0.2891 ± 0.0026	22.01 ± 0.31	0.920 ± 0.006	N
2.5	0.2970 ± 0.0027	22.59 ± 0.31	0.924 ± 0.006	N
2.6	0.3055 ± 0.0026	23.20 ± 0.32	0.932 ± 0.006	N
2.8	0.3238 ± 0.0030	23.99 ± 0.32	0.943 ± 0.006	N
3.0	0.3438 ± 0.0031	24.70 ± 0.31	0.958 ± 0.004	N

Table 5.13: Results for the simulation run with the quadratic potential, $a = 70$, $U^*_{\max} = 35$, at $T^* = 5.0$.
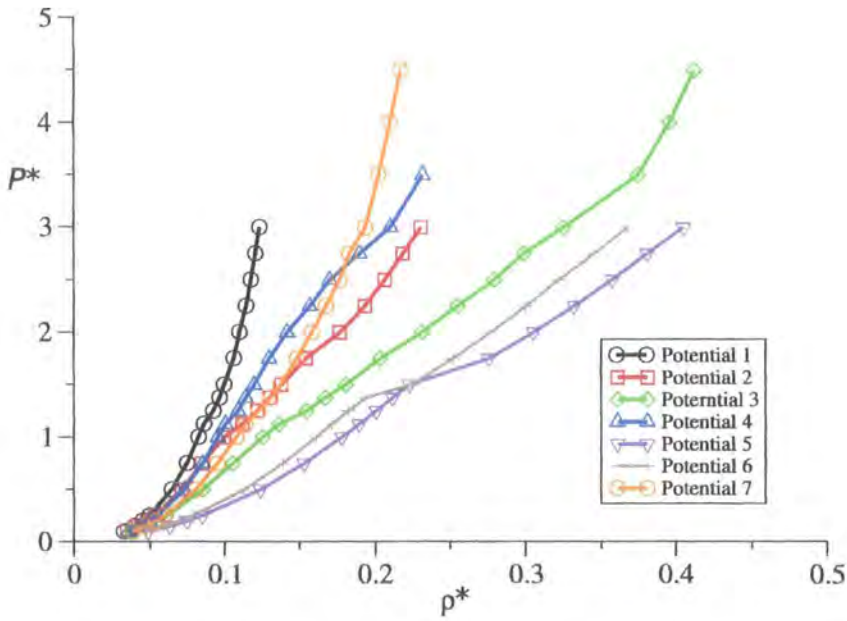
Figure 5.2: P^* as a function of ρ^* for different potentials at a temperature of $T^* = 1.0$.
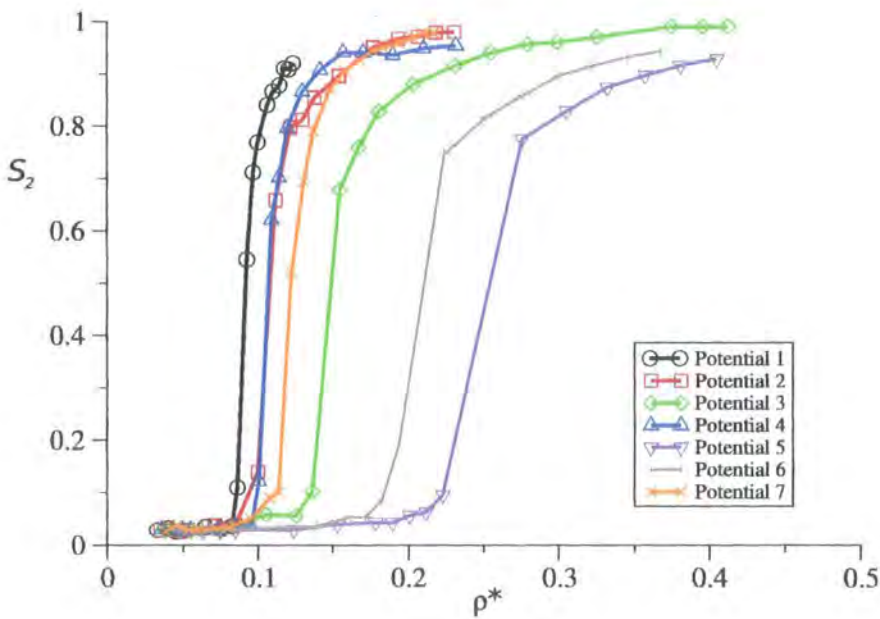
Figure 5.3: S_2 as a function of ρ^* for different potentials at a temperature of $T^* = 1.0$.
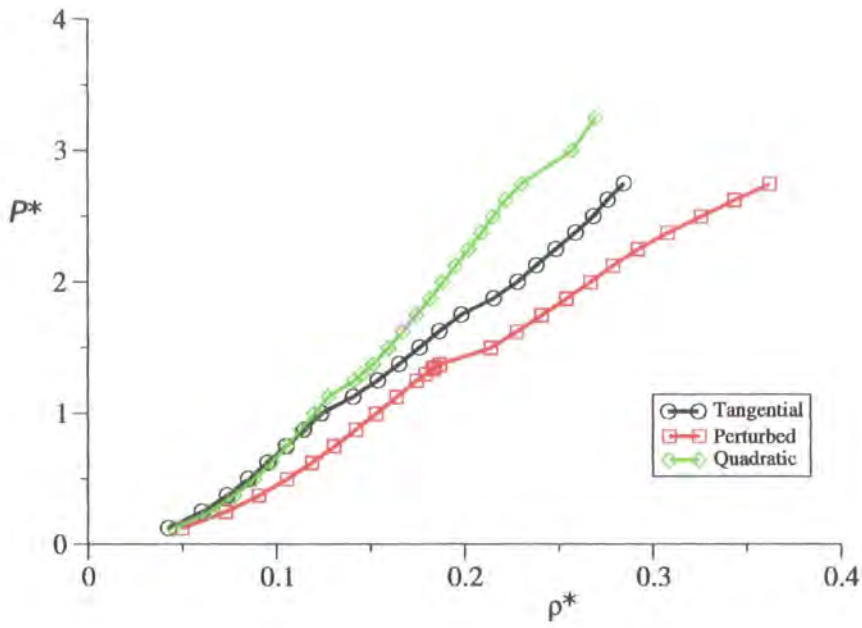
Figure 5.4: P^* as a function of ρ^* for different potentials at a temperature of $T^* = 2.0$.
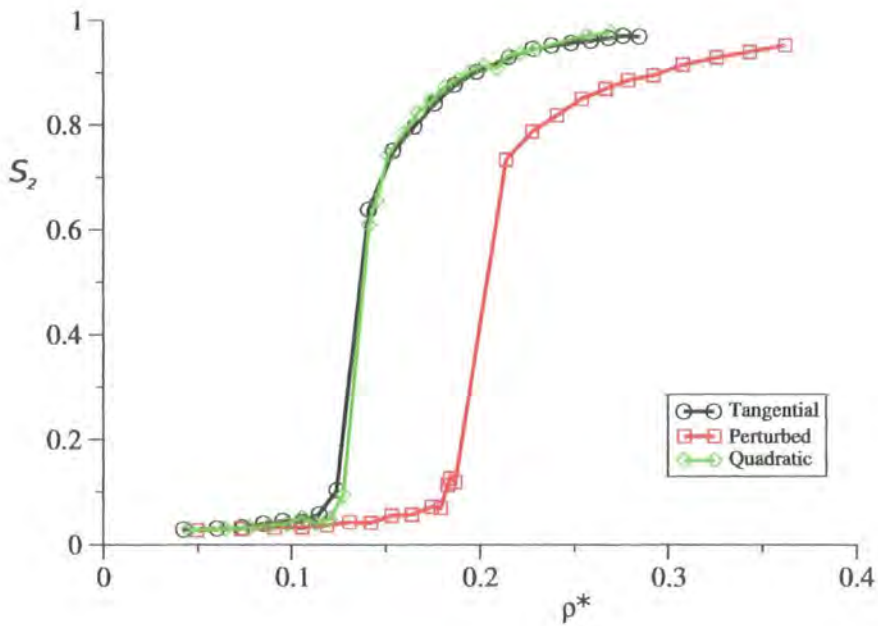
Figure 5.5: S_2 as a function of ρ^* for different potentials at a temperature of $T^* = 2.0$.
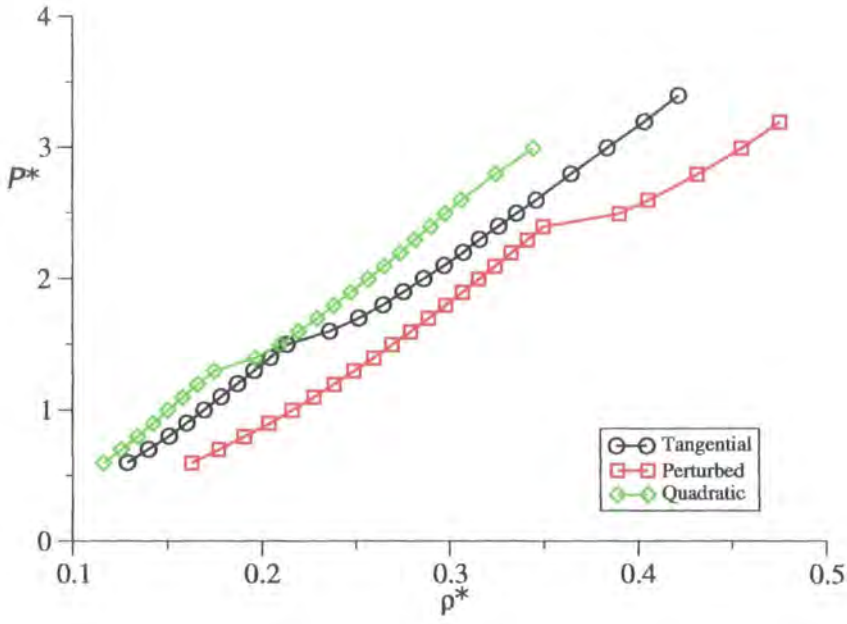
Figure 5.6: P^* as a function of ρ^* for different potentials at a temperature of $T^* = 5.0$.
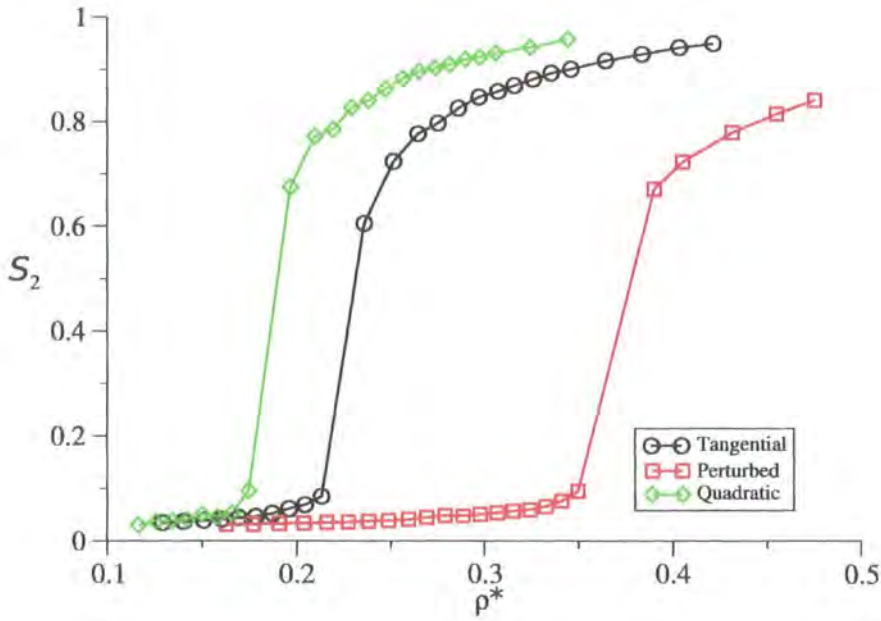
Figure 5.7: S_2 as a function of ρ^* for different potentials at a temperature of $T^* = 5.0$.
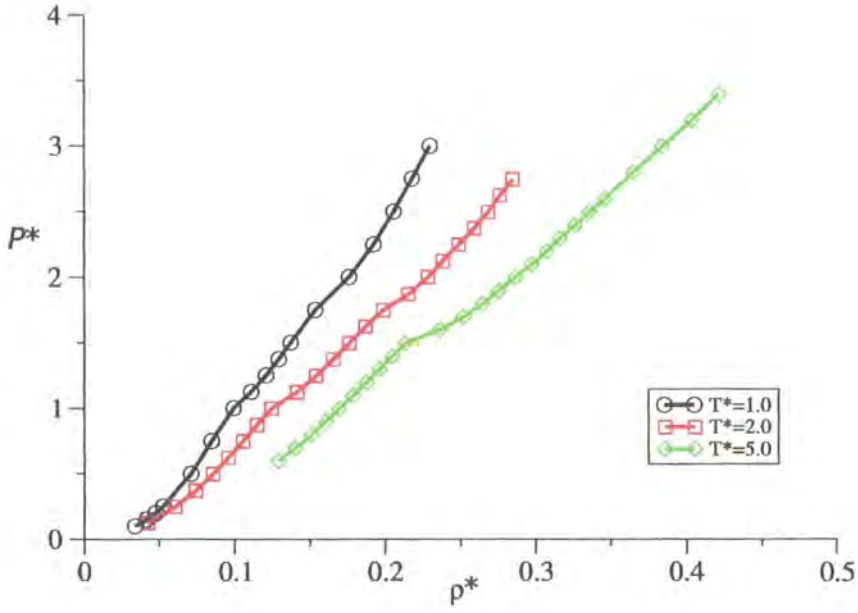
Figure 5.8: P^* as a function of ρ^* for the tangential potential ($U^*_{max} = 10$) at different temperatures.

Figure 5.9: S_2 as a function of ρ^* for the tangential potential ($U^*_{max} = 10$) at different temperatures.

Figure 5.10: P^* as a function of ρ^* for the perturbed potential ($U_{\max}^* = 4$) at different temperatures.
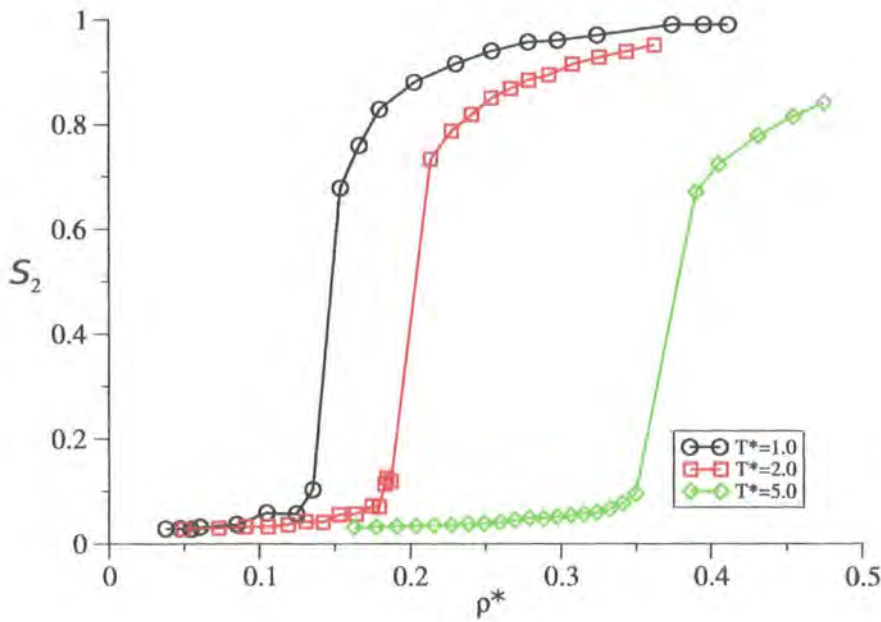
Figure 5.11: S_2 as a function of ρ^* for the perturbed potential ($U_{\max}^* = 10$) at different temperatures.
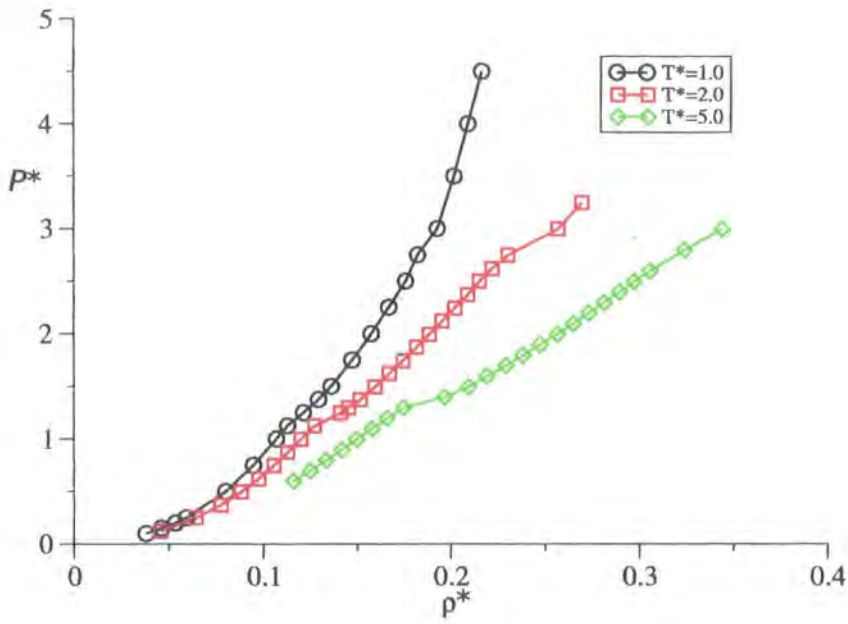
Figure 5.12: P^* as a function of ρ^* for the quadratic potential ($U^*_{\max} = 35$) at different temperatures.
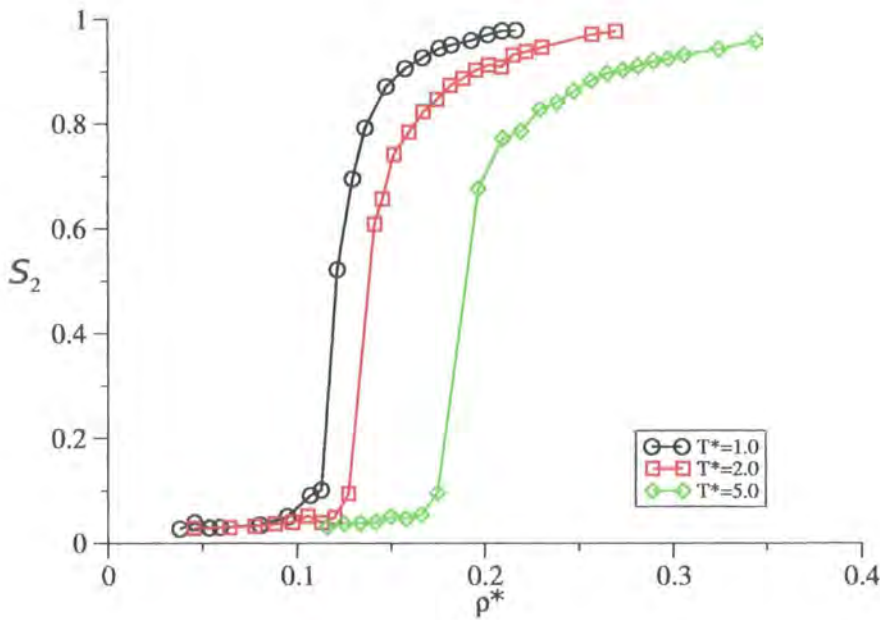
Figure 5.13: S_2 as a function of ρ^* for the quadratic potential ($U^*_{\max} = 35$) at different temperatures.

order-density plots. Figure 5.14 shows the evolution of the order parameter during the isotropic-nematic transition for three soft core potentials and the SRS potential. The time needed for the nematic phase to form does seem to be reduced for all three of the soft core potentials. This is especially true for the tangential potential where formation of the nematic phase occurs in approximately a third of the time of the SRS I-N transition.
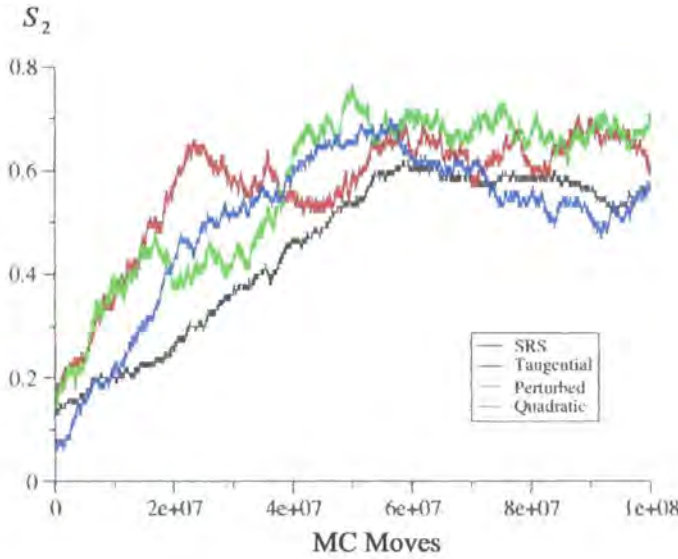
Figure 5.14: Plot showing evolution of order parameter for the SRS potential, the tangential potential ($U^*_{max} = 10$), the perturbed potential ($U^*_{max} = 4$, $c = 2/3$) and the quadratic potential ($U^*_{max} = 35$, $a = 70$).

The potentials vary as would be expected with temperature with the phase changes being forced to higher densities.

The radial distribution functions of potentials 1, 2, 3 and 7 in the different phases are shown in figures 5.18. It is immediately obvious that the perturbed potential has particularly unrealistic radial distribution functions with a large peak at $r = 0$. The reason for this is probably due to the plateau shape of the potential, once a particle is a certain distance apart (at about $r = 0.4$ in figure 5.1) then it costs only a very small amount of energy to get any closer. Meaning that the overlap between particles is especially large for this potential. Figure 5.19 shows $g_{\parallel}(r)$ and $g_{\perp}(r)$
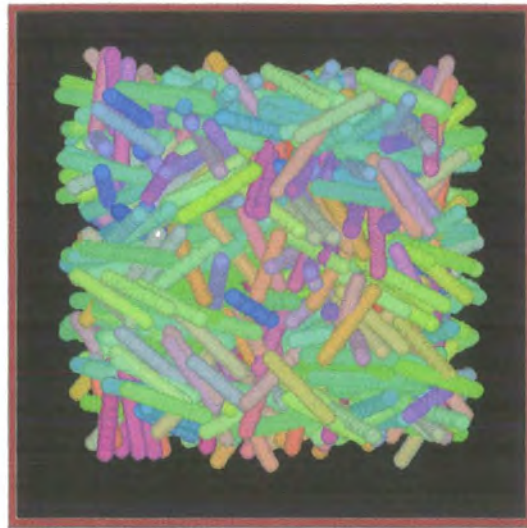
Figure 5.15: Snapshots of phases formed by the tangential soft-core potential, $U^*_{\max} = 10$: (a) isotropic phase, $\rho^* = 0.0845$, $T^* = 1.0$, (b) nematic phase, $\rho^* = 0.1372$, $T^* = 1.0$ and (c) smectic-A phase, $\rho^* = 0.1762$, $T^* = 1.0$.
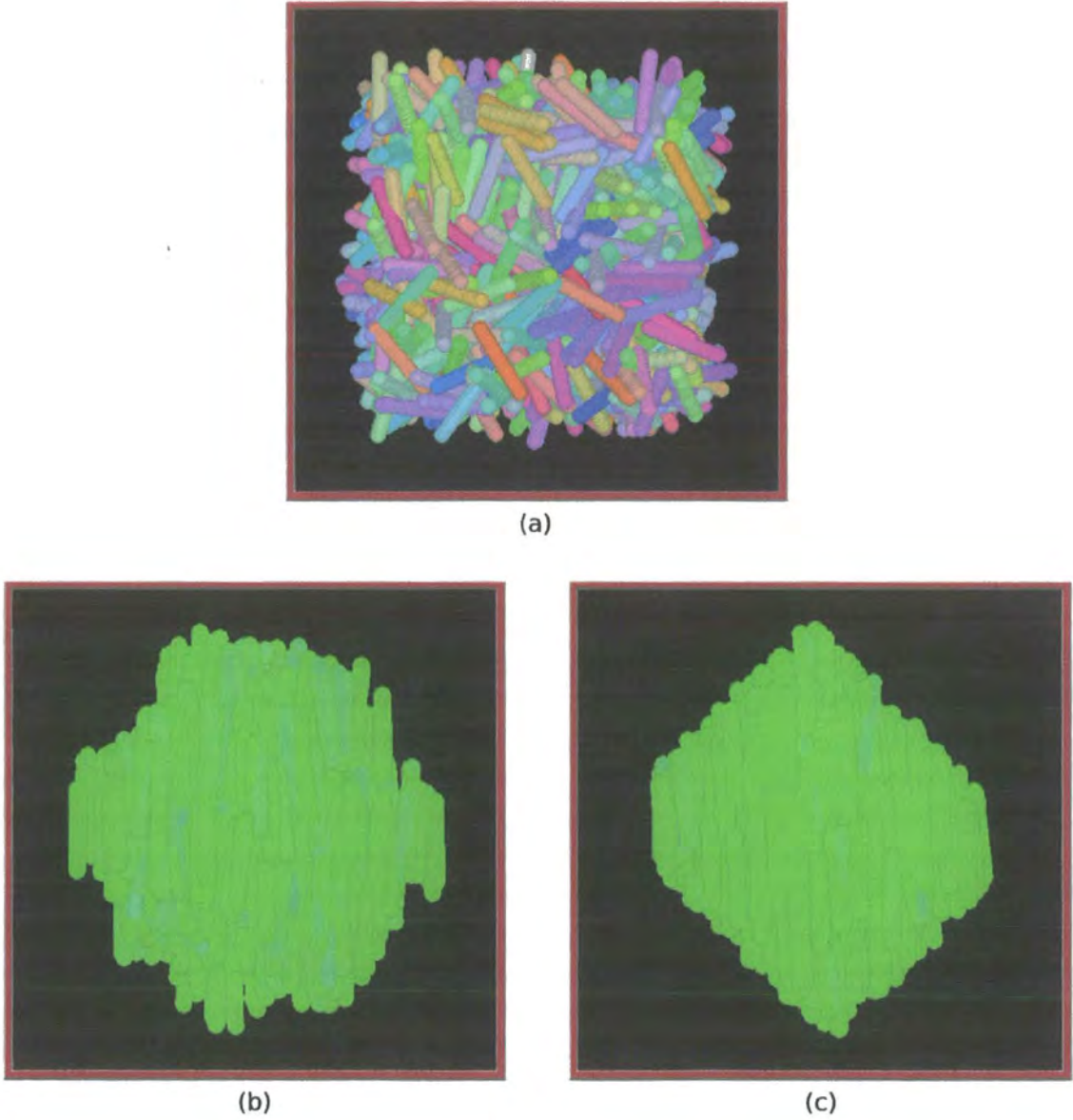
Figure 5.16: Snapshots of phases formed by the perturbed soft-core potential, $U^*_{\max} = 4$, $c = 2/3$: (a) isotropic phase, $\rho^* = 0.1247$, $T^* = 1.0$, (b) nematic phase, $\rho^* = 0.2028$, $T^* = 1.0$ and (c) smectic-A phase, $\rho^* = 0.3951$, $T^* = 1.0$.
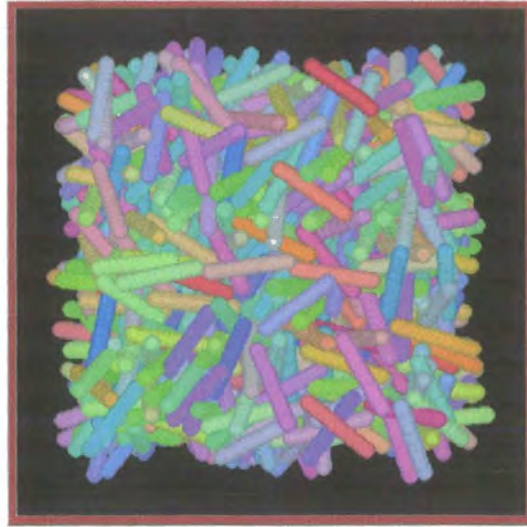
Figure 5.17: Snapshots of phases formed by the quadratic soft-core potential, $U^*_{\max} = 35$, $a = 70$: (a) isotropic phase, $\rho^* = 0.1601$, $T^* = 1.0$, (b) nematic phase, $\rho^* = 0.2760$, $T^* = 1.0$ and (c) smectic phase, $\rho^* = 0.2692$, $T^* = 2.0$.
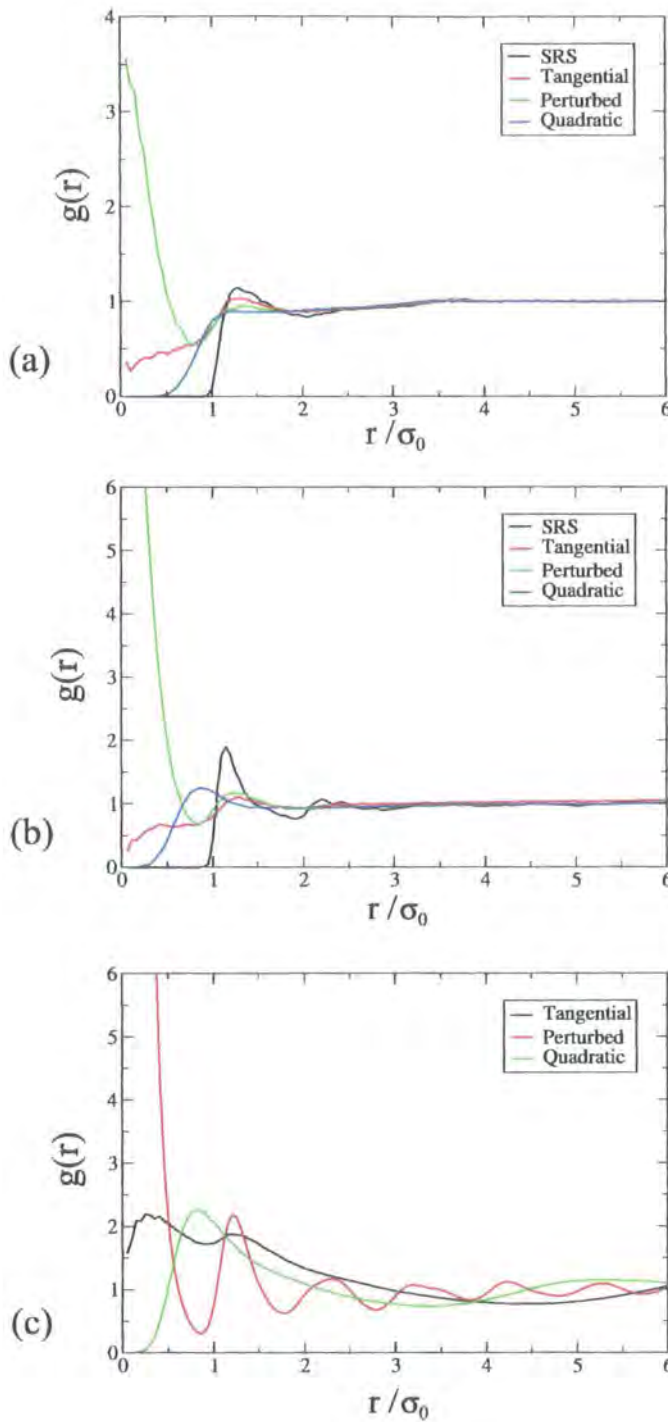
Figure 5.18: The radial distribution functions for potentials 1, 2, 3 and 7 in the: (a) isotropic, SRS $\rho^* = 0.0829$, $T^* = 1.0$, tangential $\rho^* = 0.0845$, $T^* = 1.0$, perturbed $\rho^* = 0.1247$, $T^* = 1.0$, quadratic $\rho^* = 0.1601$, $T^* = 1.0$ (b) nematic, SRS $\rho^* = 0.1100$, $T^* = 1.0$, tangential $\rho^* = 0.1372$, $T^* = 1.0$, perturbed $\rho^* = 0.2028$, $T^* = 1.0$, quadratic $\rho^* = 0.2760$, $T^* = 1.0$, (c) smectic (or crystal), tangential $\rho^* = 0.1762$, $T^* = 1.0$, perturbed $\rho^* = 0.3951$, $T^* = 1.0$, quadratic $\rho^* = 0.2692$, $T^* = 2.0$.
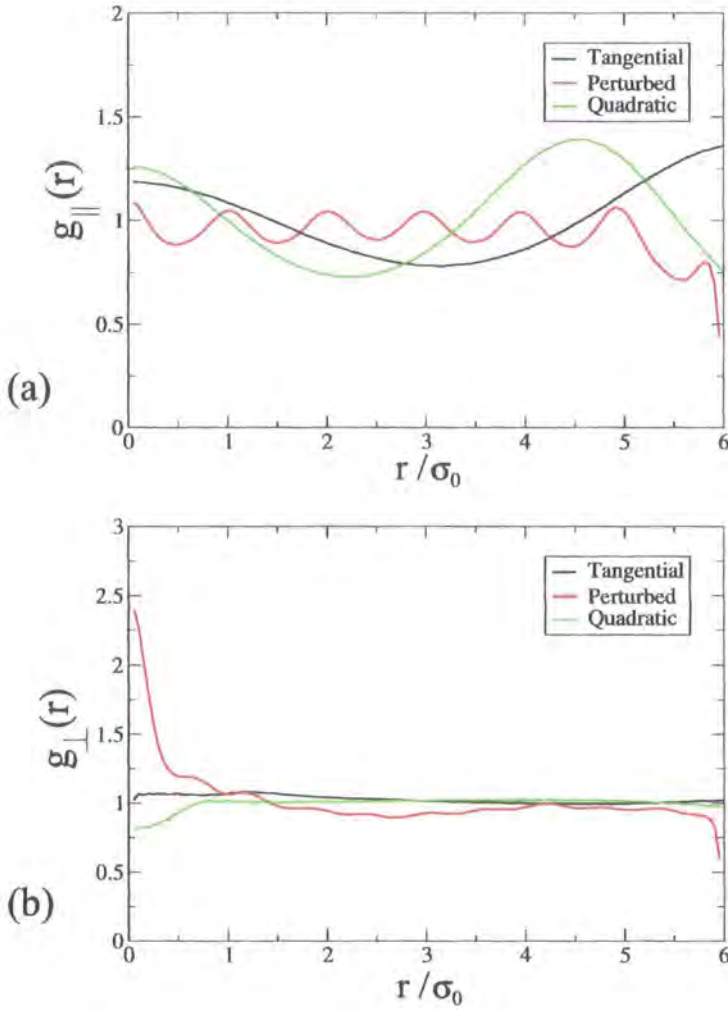
Figure 5.19: The parallel and perpendicular radial distribution functions for the smectic-A (and crystalline) phases. Tangential model $\rho^* = 0.1762$, $T^* = 1.0$, perturbed model $\rho^* = 0.3951$, $T^* = 1.0$, quadratic model $\rho^* = 0.2692$, $T^* = 2.0$: (a) parallel radial distribution function and (b) perpendicular radial distribution function.

ρ^*	T^*	$\langle U^* \rangle$	$\langle S_2 \rangle$	Phase
0.1042	5.0	10.17 ± 0.13	0.032 ± 0.012	I
0.1042	4.0	9.26 ± 0.12	0.034 ± 0.012	I
0.1042	3.5	8.69 ± 0.12	0.034 ± 0.012	I
0.1042	3.0	8.01 ± 0.11	0.035 ± 0.013	I
0.1042	2.5	7.16 ± 0.11	0.040 ± 0.015	I
0.1042	2.0	6.12 ± 0.09	0.046 ± 0.012	I
0.1042	1.5	4.77 ± 0.08	0.062 ± 0.024	I
0.1042	1.0	3.08 ± 0.06	0.426 ± 0.039	I/N
0.1042	0.5	1.14 ± 0.03	0.825 ± 0.011	N
0.1753	6.0	20.18 ± 0.17	0.039 ± 0.015	I
0.1753	5.0	19.03 ± 0.17	0.046 ± 0.017	I
0.1753	4.0	17.24 ± 0.20	0.070 ± 0.025	I
0.1753	3.5	15.67 ± 0.23	0.150 ± 0.073	I
0.1753	3.0	12.90 ± 0.20	0.642 ± 0.032	N
0.1753	2.5	11.08 ± 0.13	0.776 ± 0.015	N
0.1753	2.0	9.44 ± 0.11	0.844 ± 0.013	N
0.1753	1.5	7.57 ± 0.09	0.898 ± 0.007	SmA
0.1753	1.0	5.38 ± 0.06	0.958 ± 0.004	SmA
0.1753	0.5	3.58 ± 0.04	0.989 ± 0.003	SmA
0.2058	8.0	25.96 ± 0.20	0.038 ± 0.014	I
0.2058	6.0	24.11 ± 0.21	0.048 ± 0.018	I
0.2058	5.0	22.43 ± 0.24	0.078 ± 0.033	I
0.2058	4.5	20.98 ± 0.29	0.117 ± 0.049	I
0.2058	4.0	17.70 ± 0.29	0.632 ± 0.035	N
0.2058	3.5	15.70 ± 0.19	0.754 ± 0.017	N
0.2058	3.0	14.11 ± 0.16	0.820 ± 0.012	N
0.2058	2.5	12.45 ± 0.15	0.872 ± 0.009	N
0.2058	2.0	10.37 ± 0.14	0.913 ± 0.009	N
0.2494	8.0	32.07 ± 0.23	0.047 ± 0.018	I
0.2494	7.0	30.94 ± 0.25	0.060 ± 0.023	I
0.2494	6.0	29.03 ± 0.29	0.108 ± 0.046	I
0.2494	5.0	22.61 ± 0.31	0.715 ± 0.020	N
0.2494	4.0	19.25 ± 0.21	0.833 ± 0.011	N
0.2494	3.0	15.98 ± 0.18	0.902 ± 0.007	N
0.2494	2.0	11.23 ± 0.12	0.958 ± 0.005	SmA

Table 5.14: Results of NVT ensemble simulations for the tangential potential, $U^*_{\text{max}} = 10$.
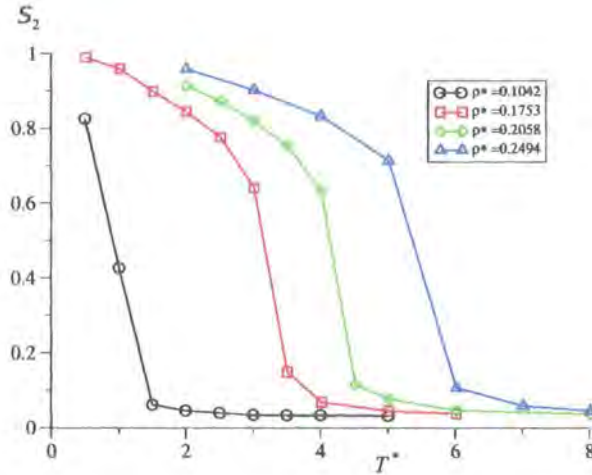
Figure 5.20: Plot of T^* vs S_2 for the tangential potential at different densities

for the smectic phases and, in the case of the perturbed potential, the crystalline phase. For the tangential and quadratic models $g_\parallel(r)$ clearly shows that the layered phases are smectic. However, the flat $g_\perp(r)$ function shows that both of these phases have no ordering within a layer. For the perturbed potential $g_\parallel(r)$ shows a regularly repeating structure parallel to the director but as before there is no ordering at all perpendicular to the director.

For the tangential potential a series of NVT simulations was also carried out at different densities. Figure 5.20 shows a plot of the order parameter as a function of reduced temperature. These simulations show that smectic phases seem to have little difficulty in forming for the tangential potential.

5.4   Spherocylinders with aspect ratio, $L/D = 7$

A series of Monte Carlo NpT simulations at $T^* = 1.0$ were also carried out using spherocylinders of aspect ratio $L/D = 7$, and $\sigma = D = \varepsilon = 1$. For this system three different soft-core potentials were used:

1. a tangential potential with $U^*_{max} = 10$,

2. a perturbed potential with $c = 2/3$ and $U^*_{max} = 4$,

3. a quadratic potential with $a = 70$ and $U^*_{max} = 35$.

As with the $L/D = 5$ spherocylinder simulations, these simulation runs involved at least 102.4×10^6 trial moves and box moves were attempted every 1024 trial moves.

5.4.1 Results

The results for the simulations using the longer spherocylinders are shown in tables 5.15-5.17 and figures 5.21 and 5.22. Again, all three of the different potentials form stable nematic phases, (see figure 5.23 for snapshots). This time no smectic phases were found, but this may be due to the fact that the maximum pressures used in the simulations were too low and with further compression of the systems smectic phases may be found.

P^*	$\langle \rho^* \rangle$	$\langle U^* \rangle$	$\langle S_2 \rangle$	Phase
0.100	0.0267 ± 0.0003	0.47 ± 0.03	0.029 ± 0.009	I
0.150	0.0328±0.0003	0.66±0.03	0.032±0.010	I
0.200	0.0374±0.0004	0.84±0.04	0.045±0.016	I
0.250	0.0413±0.0003	1.01±0.04	0.051±0.018	I
0.300	0.0447±0.0004	1.19±0.05	0.049±0.016	I
0.350	0.0481±0.0004	1.37±0.05	0.053 ± 0.013	I
0.375	0.0494±0.0004	1.46±0.05	0.066±0.016	I
0.380	0.0496±0.004	1.48±0.05	0.051±0.015	I
0.400	0.0510±0.0004	1.55±0.05	0.065±0.014	I
0.425	0.0523±0.0004	1.65±0.05	0.067±0.017	I
0.450	0.0542±0.0004	1.74±0.06	0.131±0.013	I
0.475	0.0562±0.0004	1.83±0.06	0.272±0.021	I
0.500	0.0601±0.0005	1.92±0.06	0.547±0.011	N
0.525	0.0629±0.0005	2.03±0.06	0.684±0.013	N
0.550	0.0653±0.0006	2.13±0.06	0.777±0.015	N
0.575	0.0671±0.0005	2.23±0.06	0.790±0.010	N
0.600	0.0691±0.0005	2.34±0.07	0.820±0.012	N
0.650	0.0722 ± 0.0006	2.55 ± 0.07	0.842±0.010	N
0.700	0.0758 ± 0.0006	2.77±0.07	0.871±0.009	N
0.750	0.0791±0.0007	3.00±0.07	0.867±0.012	N
0.800	0.0829 ± 0.0007	3.23±0.07	0.901±0.010	N

Table 5.15: Results for the simulation run with the tangential potential with $U^*_{\text{max}} = 10$, for a system of spherocylinders of length $L/D = 7$, at $T^* = 1.0$.

The plot of the radial distribution functions, however, shows that there are some differences between the $L/D = 5$ systems and the $L/D = 7$ systems. For the longer spherocylinders the radial distribution functions more closely resemble those of a

P^*	$\langle \rho^* \rangle$	$\langle U^* \rangle$	$\langle S_2 \rangle$	Phase
0.100	0.0305 ± 0.0004	0.56 ± 0.03	0.030 ± 0.010	I
0.150	0.0374 ± 0.0004	0.79 ± 0.04	0.032 ± 0.012	I
0.200	0.0431 ± 0.0005	1.02 ± 0.04	0.035 ± 0.013	I
0.250	0.0479 ± 0.0005	1.24 ± 0.05	0.033 ± 0.009	I
0.300	0.0525 ± 0.0005	1.46 ± 0.06	0.048 ± 0.014	I
0.325	0.0545 ± 0.0005	1.57 ± 0.05	0.036 ± 0.014	I
0.350	0.0566 ± 0.0005	1.67 ± 0.06	0.048 ± 0.015	I
0.375	0.0586 ± 0.0005	1.78 ± 0.06	0.048 ± 0.019	I
0.400	0.0607 ± 0.0005	1.88 ± 0.05	0.046 ± 0.013	I
0.450	0.0646 ± 0.0006	2.09 ± 0.06	0.045 ± 0.019	I
0.500	0.0689 ± 0.0006	2.28 ± 0.06	0.095 ± 0.029	I
0.550	0.0797 ± 0.0009	2.39 ± 0.06	0.690 ± 0.017	N
0.600	0.0854 ± 0.0007	2.58 ± 0.06	0.764 ± 0.013	N
0.650	0.0908 ± 0.0008	2.72 ± 0.06	0.810 ± 0.012	N
0.700	0.0957 ± 0.0009	2.88 ± 0.06	0.817 ± 0.014	N

Table 5.16: Results for perturbed potential with $c = 2/3$, $U^*_{max} = 4$, for a system of spherocylinders of length $L/D = 7$, at $T^* = 1.0$.

P^*	$\langle \rho^* \rangle$	$\langle U^* \rangle$	$\langle S_2 \rangle$	Phase
0.100	0.0301 ± 0.004	0.30 ± 0.02	0.029 ± 0.010	I
0.150	0.0366 ± 0.0004	0.41 ± 0.02	0.031 ± 0.013	I
0.200	0.0419 ± 0.0004	0.52 ± 0.03	0.033 ± 0.010	I
0.250	0.0463 ± 0.0004	0.62 ± 0.03	0.028 ± 0.010	I
0.275	0.0483 ± 0.0004	0.66 ± 0.03	0.039 ± 0.011	I
0.300	0.0502 ± 0.0004	0.71 ± 0.03	0.035 ± 0.009	I
0.325	0.0521 ± 0.0005	0.76 ± 0.03	0.049 ± 0.012	I
0.350	0.0538 ± 0.0004	0.80 ± 0.03	0.047 ± 0.014	I
0.400	0.0570 ± 0.0005	0.89 ± 0.03	0.140 ± 0.012	I
0.450	0.0604 ± 0.0004	0.98 ± 0.04	0.216 ± 0.017	I
0.500	0.0638 ± 0.0005	1.06 ± 0.04	0.256 ± 0.016	I
0.550	0.0703 ± 0.0006	1.11 ± 0.04	0.635 ± 0.013	N
0.600	0.0726 ± 0.0006	1.17 ± 0.05	0.724 ± 0.012	N

Table 5.17: Results for quadratic potential with $a = 70$, $U^*_{max} = 35$, for a system of spherocylinders of length $L/D = 7$, at $T^* = 1.0$.
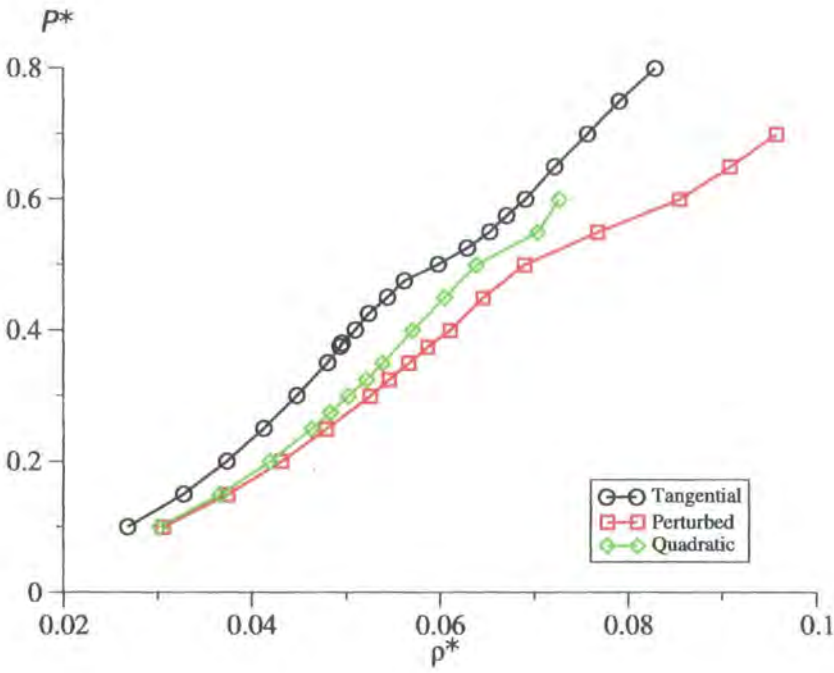
Figure 5.21: Phase diagram for the $L/D = 7$ spherocylinder systems.
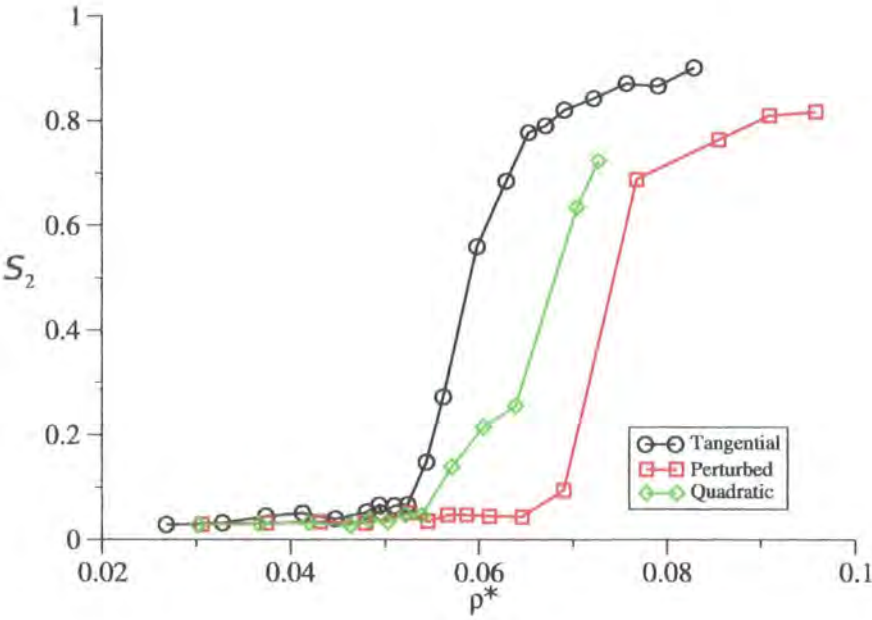
Figure 5.22: S_2 as a function of ρ^* for the $L/D = 7$ spherocylinder systems.

SRS potential, with $g(r)$ dropping to zero faster than for the $L/D = 5$ systems. Even in the case of the perturbed potential the peaks at zero separation are much smaller than for the equivalent phase of the smaller spherocylinders. This due to the longer aspect ratio of the spherocylinders causing the formation of the nematic phase at lower density, thus the overlap of molecules in the soft-core system is reduced.

5.5   Conclusions

The work in this chapter has shown that all three soft-core potentials used do form stable mesophases, with nematic phases forming for all potentials and over a range of temperatures. The formation of smectic phases proved to be more difficult but such phases did form for some of the potentials at lower temperatures. In addition, the soft-core potentials did succeed with respect to their main aims; i.e. the formation of mesophases was quicker in the case of the soft-core potentials than for the SRS potential. The general shape of the phase diagrams follow that of the SRS potential quite closely, with phase changes clearly visible as discontinuities in the pressure-density phase diagram. While plots of the order parameter as a function of density recreated the typical S-curve previously seen for liquid crystals.

The difference between the radial distribution function of the soft-core models and the SRS model is far more pronounced. The radial distribution functions for the shorter spherocylinders are quite unrealistic, particularly for the perturbed potential. However, the longer spherocylinders have radial distribution functions that are much more like those of an SRS potential due to the formation of liquid crystal phases at lower densities.

Each of the potentials had their advantages and disadvantages. The tangential had the greatest ease in forming smectic phases, mesophase transitions were particularly quick for it and the radial distribution functions while not as good as those of the quadratic potential are a great improvement on the perturbed model. While the perturbed model formed nematic liquid crystal phases quickly it had great difficulty in forming anything resembling a conventional smectic phase, in addition the large peak in the radial distribution functions at short separations means that it is par-
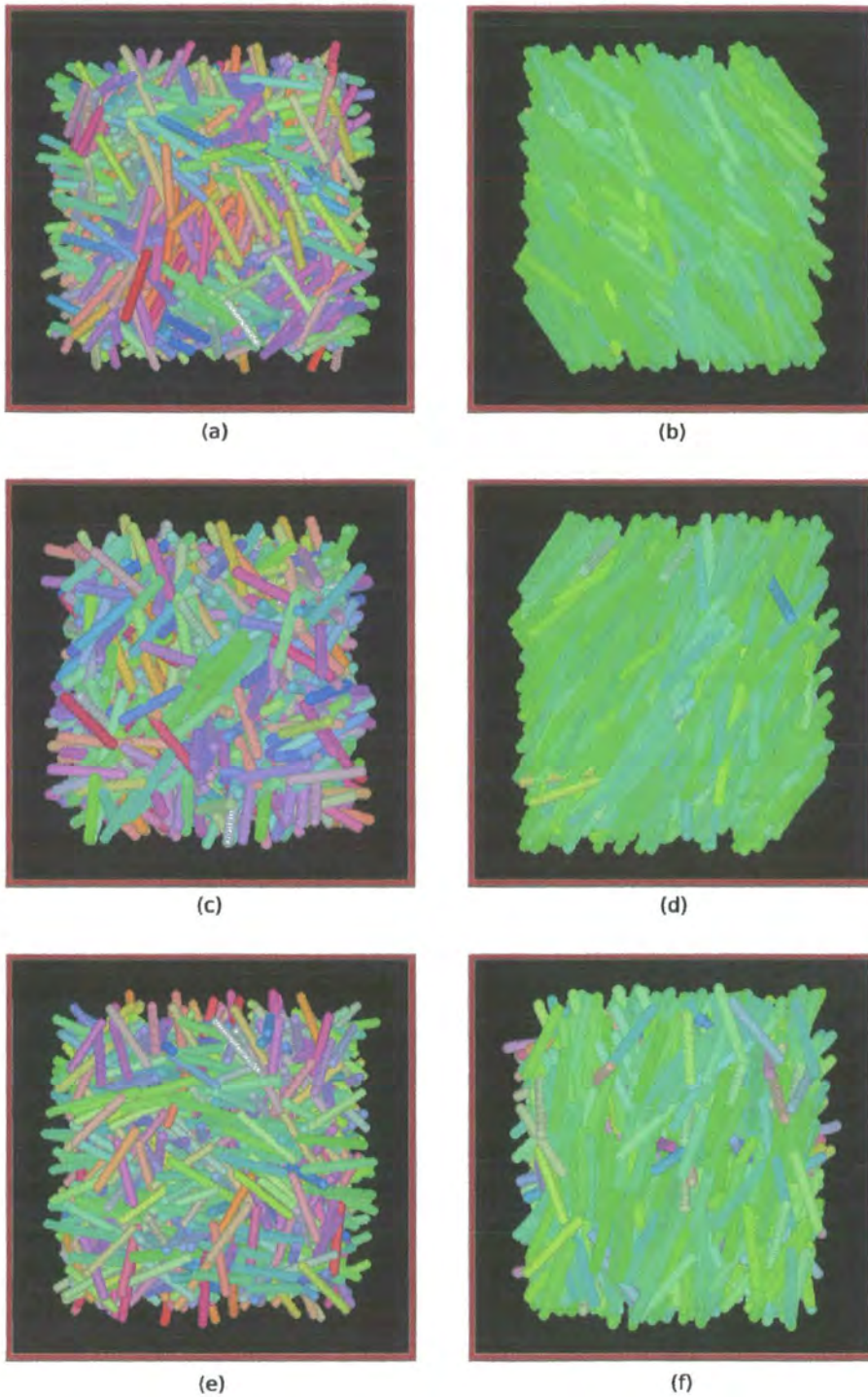
Figure 5.23: Snapshots of phases formed by the $L/D = 7$ spherocylinders: (a) isotropic phase formed by the tangential potential, $U^*_{\max} = 10$, $\rho^* = 0.0481$, $T^* = 1.0$; (b) nematic phase formed by the tangential potential, $U^*_{\max} = 10$, $\rho^* = 0.0653$, $T^* = 1.0$; (c) isotropic phase formed by the perturbed potential potential, $U^*_{\max} = 4$, $\rho^* = 0.0646$, $T^* = 1.0$; (d) nematic phase formed by the perturbed potential, $U^*_{\max} = 4$, $\rho^* = 0.0854$, $T^* = 1.0$;(e) isotropic phase formed by the quadratic potential, $U^*_{\max} = 35$, $\rho^* = 0.0538$, $T^* = 1.0$,;and (f) nematic phase formed by the quadratic potential, $U^*_{\max} = 35$, $\rho^* = 0.0703$, $T^* = 1.0$.
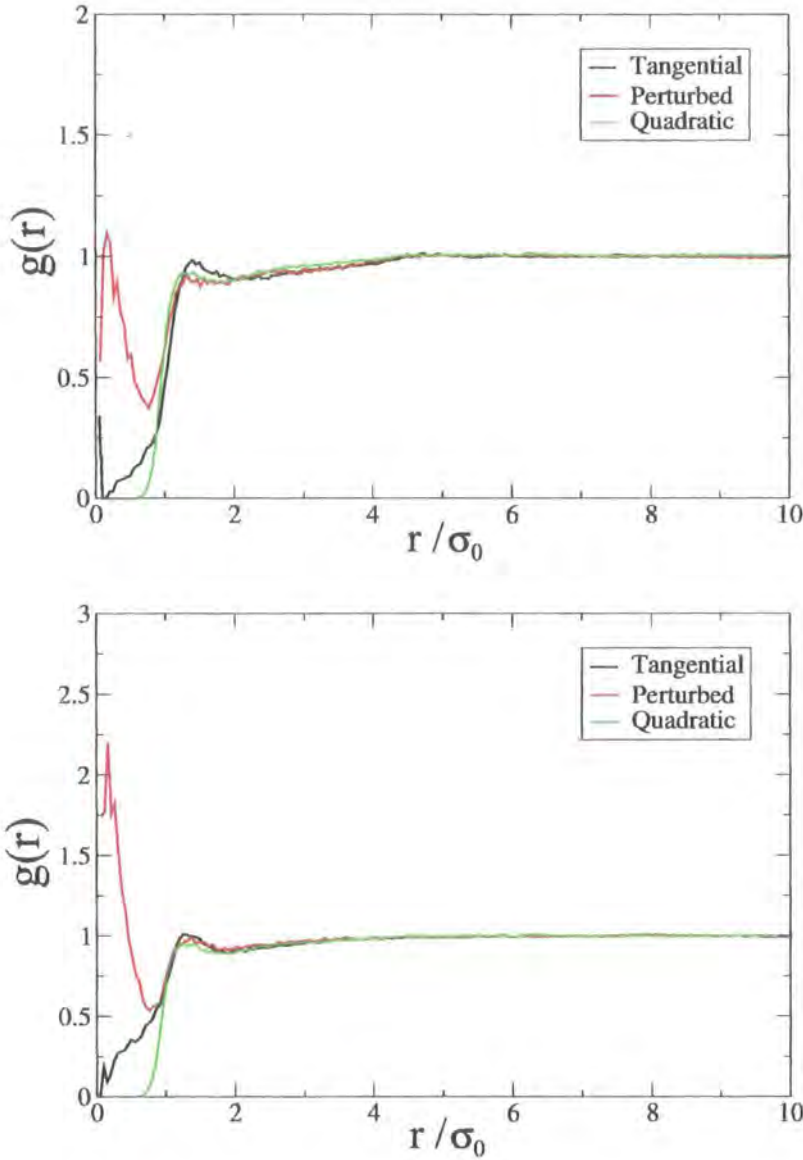
Figure 5.24: Radial distribution functions for the $L/D = 7$ spherocylinder system. Top: the isotropic phase, the tangential potential $\rho^* = 0.0653$, the perturbed potential $\rho^* = 0.0481$ and the quadratic potential $\rho^* = 0.0538$. Bottom: the nematic phase, the tangential potential $\rho^* = 0.0653$, the perturbed potential $\rho^* = 0.0854$ and the quadratic potential $\rho^* = 0.0703$.

ticularly unrealistic. The radial distribution functions for the quadratic potential are the most realistic and this potential did show the formation of a smectic phase. However, the transitions between state points was slower than for the other two models. The final choice of which potential to use will of course depend upon the system being simulated. If the radial distribution functions are particularly important then the quadratic potential is probably the most appropriate model. If not, then the tangential potential is probably the most efficient model to use.

It would be relatively easy to use any of the soft-core potentials developed in this chapter with the potential softening technique discussed in section 4.3. A series of replicas with gradually lower U_{max} values might be more effective than the Tsallis potential used in the previous chapter. Use of these models with the potential softening technique would be a interesting new area for research.

Chapter 6

Coarse-Grained Soft-Core Systems

The previous chapter showed that anisotropic soft-core potentials will not only form a variety of different liquid crystal phases but will do so much faster than the SRS potential. However, the single site potentials described in chapter 5 already form liquid crystal phases quite easily, it is for macromolecular systems that the computer time needed to see mesophase formation becomes prohibitive. This chapter contains some preliminary work on the application of soft-core models to multi-site molecules. The systems simulated were: a coarse-grained liquid crystal with twin alkyl chain groups attached terminally; and two coarse-grained side-chain liquid crystal polymers/oligomers.

Based on the work carried previously for spherocylinders (in chapter 5), the tangential soft-core potential seemed to be the most promising of the three soft-core potentials tried so this was the potential used to model the more complex systems.

6.1   Liquid Crystals With Twin Alkyl Chains

A simple extension of the previous soft-core potential work involved modelling a liquid crystal with alkyl chains attached to each end. The chemical structure for such a molecule is shown in figure 6.1. A coarse-grained model for this type of molecule was built by representing the biphenyl group as a spherocylinder and adding a set of spheres to each end to model the alkyl chains. Both Monte Carlo and molecular dynamics methods were used to simulate the system, but used slightly different

models.

A tangential soft-core potential (Eqn 5.1) was used to model both the sphero-cylinder and spheres. An additional advantage of soft-core potentials is that it is possible to make the interactions between different parts of the molecule more or less repulsive. For this system the like-like interactions were made less repulsive than the like-unlike interactions. For the spherocylinder-spherocylinder and sphere-sphere interactions a tangential potential with $U^*_{max} = 10$ was used. However, the sphere-spherocylinder potential was set as $U^*_{max} = 20$.
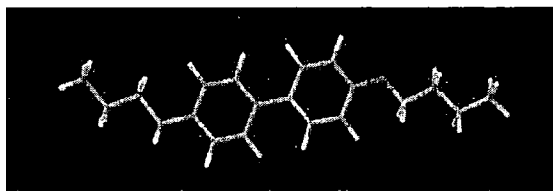
Figure 6.1: Liquid crystal molecule with an alkyl chain attached to each end.

6.1.1 Monte Carlo Runs for a Twin Alkyl Chains

For the Monte Carlo calculations a spherocylinder with aspect ratio of $L/D = 5$ and $\sigma = D = \varepsilon = 1$ (model A) was used, three spheres of diameter σ were added to each end of the spherocylinder. The bond distance between the centres of two spheres was set at σ while the bond distance between the centres of a spherocylinder and a sphere was 2.5σ. The bond angles and dihedral angles were set at 180°, meaning that the sites in the molecule were just touching each other while being aligned to the long axis of the spherocylinder. For this system no intramolecular moves were permitted, only intermolecular translations and rotations were allowed. Figure 6.2 shows a schematic diagram of model A.

The systems simulated consisted of 1331 of these molecules (a total of 9317 sites). Runs were carried out for at least 133100000 trial moves (more for the highest density systems), with box moves being attempted every 1331 MC moves. The simulations used an NpT ensemble and took place at a temperature of $T^* = 1.0$.
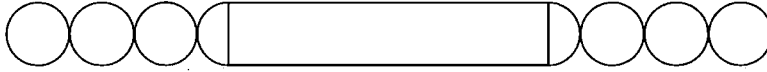
Figure 6.2: Schematic illustration of the twin alkyl chain molecule simulated in the Monte Carlo calculations (model A).

Results

Table 6.1 shows the results for MC simulations of model A in reduced units, and the phase diagram of the system is shown in figure 6.3.

It is clear from figure 6.3 that the system undergoes two phase changes. The isotropic-nematic transition which takes place at $\rho^* = 0.0320$, figure 6.5(b) shows a snapshot of the nematic phase. A second phase change takes place at $\rho^* = 0.0434$ to the phase formed in figure 6.5(c). As this is clearly not a smectic phase it is probably best described as a solid phase due to the high order, the fact that there is very little motion in the system and that compression of the system gives a linear increase in the pressure and energy.

P^*	$\langle \rho^* \rangle$	$\langle U^* \rangle$	$\langle S_2 \rangle$	Phase
0.050	0.0138 ± 0.0001	0.28 ± 0.02	0.026 ± 0.012	I
0.060	0.0150 ± 0.0001	0.32 ± 0.02	0.023 ± 0.007	I
0.075	0.0168 ± 0.0002	0.38 ± 0.02	0.043 ± 0.031	I
0.100	0.0192 ± 0.0002	0.46 ± 0.02	0.028 ± 0.009	I
0.125	0.0212 ± 0.0002	0.54 ± 0.03	0.071 ± 0.011	I
0.150	0.0229 ± 0.0001	0.63 ± 0.03	0.054 ± 0.013	I
0.200	0.0263 ± 0.0002	0.76 ± 0.03	0.231 ± 0.008	I
0.250	0.0320 ± 0.0002	0.72 ± 0.03	0.798 ± 0.008	N
0.300	0.0353 ± 0.0002	0.77 ± 0.03	0.865 ± 0.005	N
0.350	0.0378 ± 0.0002	0.94 ± 0.03	0.890 ± 0.001	N
0.400	0.0396 ± 0.002	0.94 ± 0.03	0.890 ± 0.001	N
0.450	0.0413 ± 0.0003	1.02 ± 0.03	0.899 ± 0.004	N
0.500	0.0434 ± 0.0002	1.07 ± 0.04	0.930 ± 0.001	K
0.600	0.0450 ± 0.0002	1.17 ± 0.04	0.933 ± 0.001	K
0.650	0.0458 ± 0.0002	1.25 ± 0.05	0.940 ± 0.001	K

Table 6.1: Results of NpT MC simulations on the twin alkyl chain liquid crystal system (model A).
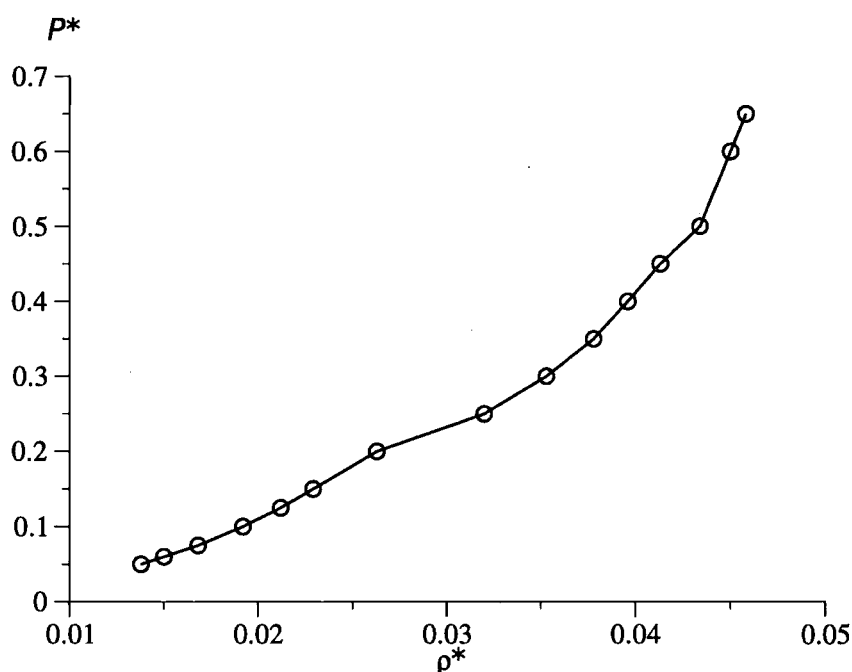
Figure 6.3: P^* as a function of ρ^* for the Monte Carlo simulations of the twin chain molecule A.

6.1.2 Molecular Dynamics Runs

For the MD simulations an aspect ratio of $L/D = 7$ and $\sigma = D = \varepsilon = 1$ was used (model B). Again three spheres of diameter σ were attached to each end. However, for this model the sites were not fixed in respect of each other. The bonds and angle terms where included in the force field but dihedral terms were ignored. The spheres were bonded together at their centres, and bonded to the spherocylinders at the end of the long axis of the cylinder (as shown in figure 6.6). A spherocylinder angle term was added to the force field[1], this is the angle between the centre of the spherocylinder, the bonding point of the spherocylinder and the centre of the sphere. The bond, angles and SC angles were all harmonic potentials.

The constants used for the bonds and angles are shown in table 6.2. The bond

---

[1]Deviation from the equilibrium angle gives rise to forces on the centres of the spherocylinder and sphere, plus a gorque (force perpendicular to the long axis) on the spherocylinder.
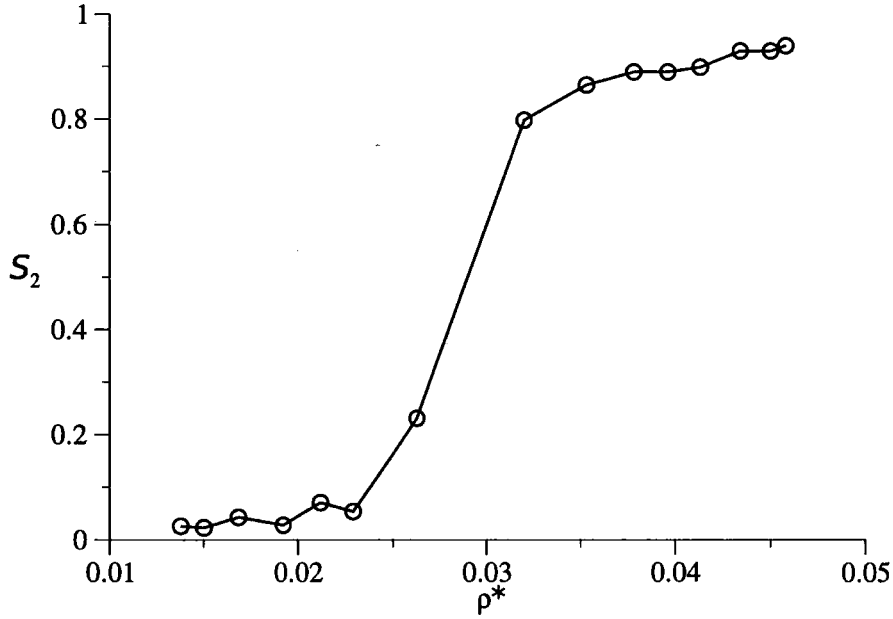
Figure 6.4: S_2 as a function of ρ^* for the Monte Carlo simulations of the twin chain molecule A.

Bond	r_0/σ	$k_{bond}/\varepsilon\,\sigma^{-2}$
sphere-sphere	1	50.0
sphere-spherocylinder	4.5	50.0

Angle	$\theta_0/^\circ$	$k_{angle}/\varepsilon\,\mathrm{rad}^{-2}$
sphere-sphere-sphere	180	50.0
sphere-sphere-SC	180	50.0
sphere-SC-sphere	180	50.0
SC-sphere	180	50.0

Table 6.2: Parameters used in the force field for the twin chain molecule B.
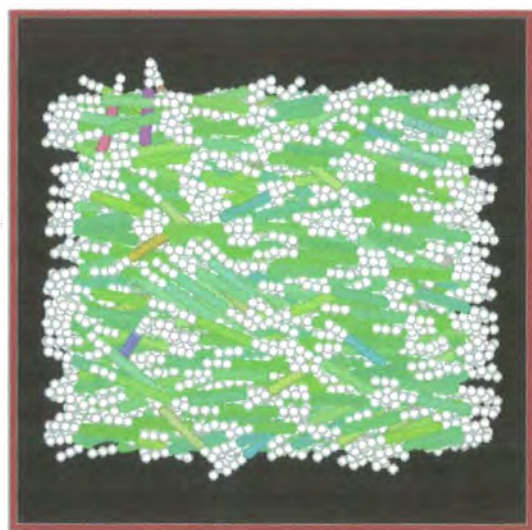
Figure 6.5: Snapshots of phases formed by the the twin chain molecule A in the Monte Carlo simulations: (a) isotropic phase, $\rho^* = 0.0192$, (b) nematic phase, $\rho^* = 0.0353$, and (c) solid phase, $\rho^* = 0.0458$.
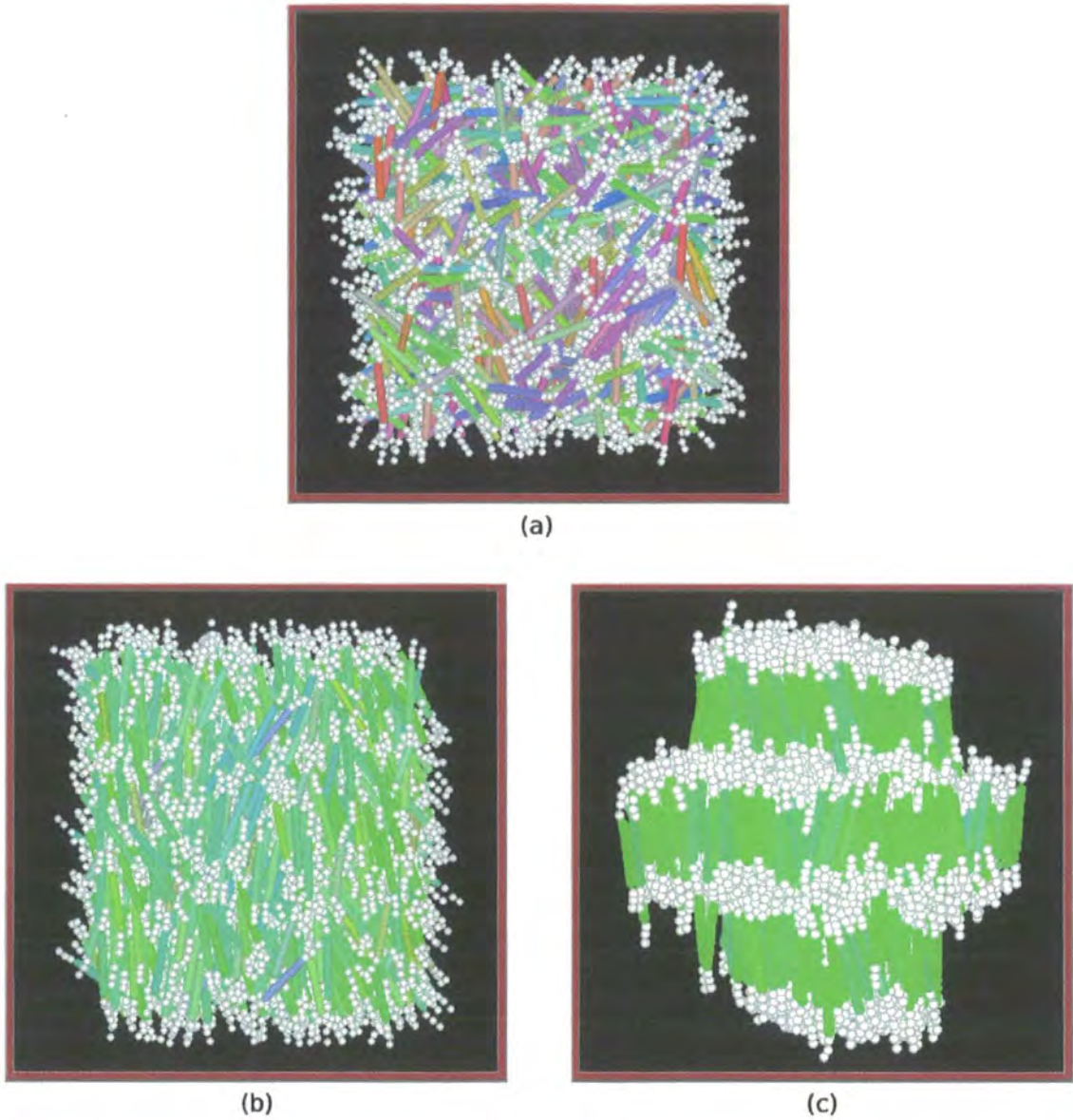
Figure 6.10: Snapshots of the phases formed during the molecular dynamics simulations of the liquid crystals with twin alkyl chains (model B): (a) isotropic phase, $\rho = 0.0396/\sigma^{-3}$, (b) nematic phase $\rho = 0.0524/\sigma^{-3}$ and (c) smectic-A phase, $\rho = 0.0905/\sigma^{-3}$.
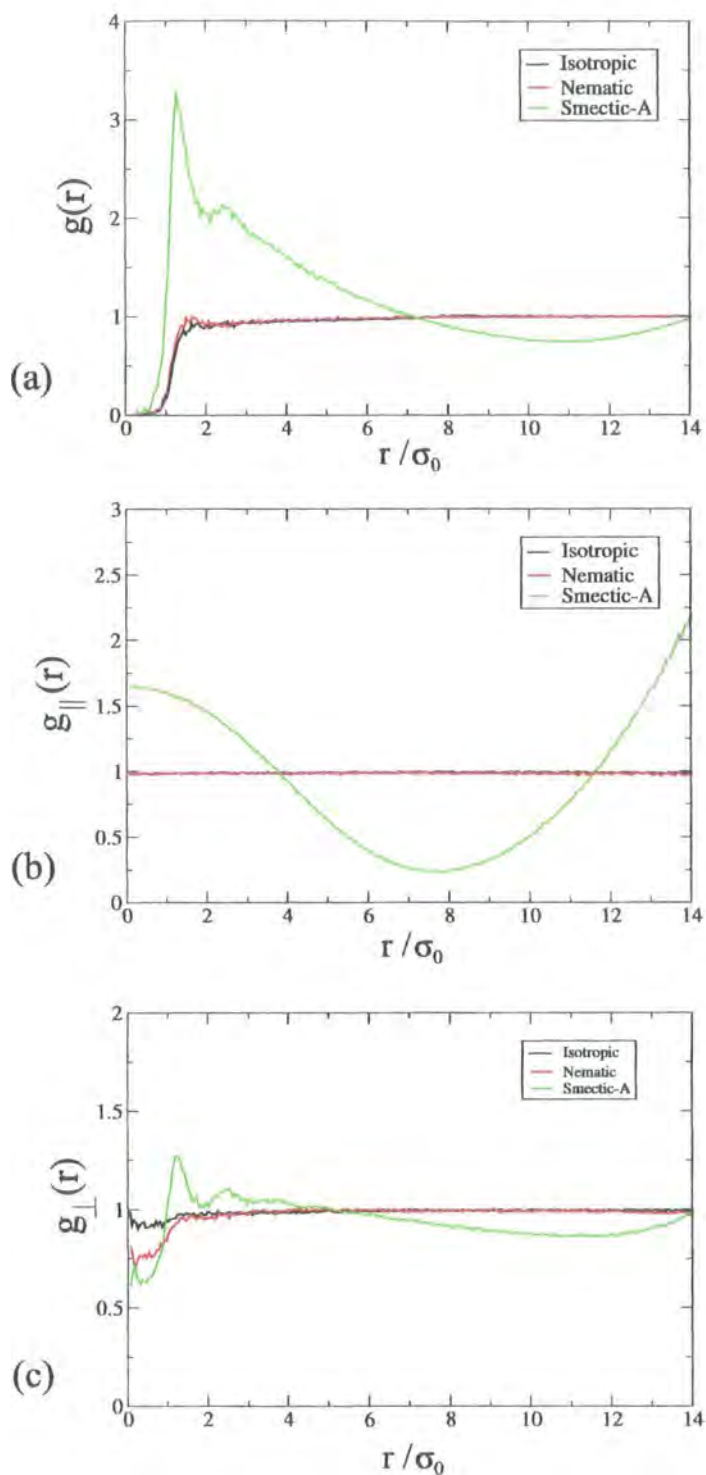
Figure 6.11: The radial distribution functions of the spherocylinders for the MD simulations of the mesogens with twin alkyl chains: (a) $g(r)$, (b) $g_{\parallel}(r)$ and (c) $g_{\perp}(r)$ in the isotropic phase, $\rho = 0.0396/\sigma^{-3}$, nematic phase $\rho = 0.0524/\sigma^{-3}$ and the smectic-A phase $\rho = 0.0905/\sigma^{-3}$.

the mesogens are attached terminally or laterally. In order to see if such differences could be observed with soft-core potentials two polymer systems were built and simulated with molecular dynamics.

6.2.1 The Polymer Models

The polymers were twenty repeat units long consisting of spheres of diameter σ and spherocylinders of length $L/D = 7$, where $\sigma = D = \varepsilon = 1$. Each repeat unit consisted of a backbone of five spheres bonded together, with a side chain, consisting of two spheres and a spherocylinder, bonded to the central sphere (see figure 6.12). Therefore the overall polymer molecules were one hundred spheres long and had twenty mesogenic side groups. Figure 6.13 shows a single terminal and lateral polymer molecule. As with the twin alkyl chain mesogens the sphere-sphere and spherocylinder-spherocylinder interactions were both set at $U^*_{\mathrm{max}} = 10$, while the sphere-spherocylinder interactions were set at $U^*_{\mathrm{max}} = 20$.

For these systems the spheres were bonded to the centre of the spherocylinders, and a spherocylinder angle term was formed by the centre of the sphere, the centre of the spherocylinder and the end point of the central axis of the spherocylinder (see figure 6.12).

Bond	terminal r_0/σ	lateral r_0/σ	$k_{bond}/\varepsilon\,\sigma^{-2}$
R_1	4.5	1.0	50.0
R_2	1.0	1.0	50.0

Angle	terminal $\theta_0/°$	lateral $\theta_0/°$	$k_{angle}/\varepsilon\,\mathrm{rad}^{-2}$
θ_1	180	180	50.0
θ_2	90	90	50.0
θ_{SC}	180	90	50.0

Table 6.3: Force field parameters used in the liquid crystal polymer simulations.

Table 6.3 gives the intramolecular constants used in the simulation, the bond and angle terms used the standard harmonic potentials, bonded sites were excluded from the sum of the nonbonding terms.

Each system consisted of sixty four polymers, originally the polymers were set up on a lattice in the gas phase. Several short NpT runs at high pressure compressed the
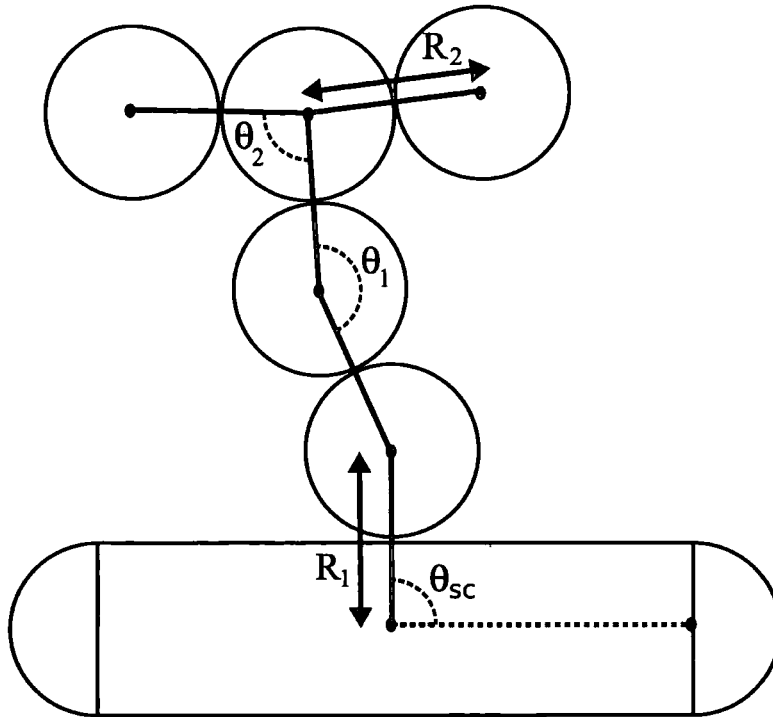
Figure 6.12: Schematic diagram of a repeat unit in the polymer systems, showing the different bonds and angles in the molecule.

system in stages, with the system being allowed to equilibrate in a NVT simulation after each increase in density. The simulations were carried out using a Andersen thermostat, at a reduced temperature of $T^* = 1.0$, and MC box moves were used to keep the pressure constant. Once a liquid phase was reached simulations were carried out using NpT molecular dynamics. A reduced timestep of $0.003 < \delta t^* < 0.004$ was used with simulations lasting for up to 500,000 timesteps.

6.2.2 Results and Discussion

Figure 6.14 shows the phase diagram for the polymer simulations. Disappointingly no liquid crystal phases were seen for either the terminal or lateral polymers. It might simply be that more simulation time is needed before a mesophase will form, however, this differs strongly from the alkyl chain mesogens discussed in section 6.1.2 where mesophases formed quite quickly.

There are a number of reasons why the polymers might not form mesophases (or
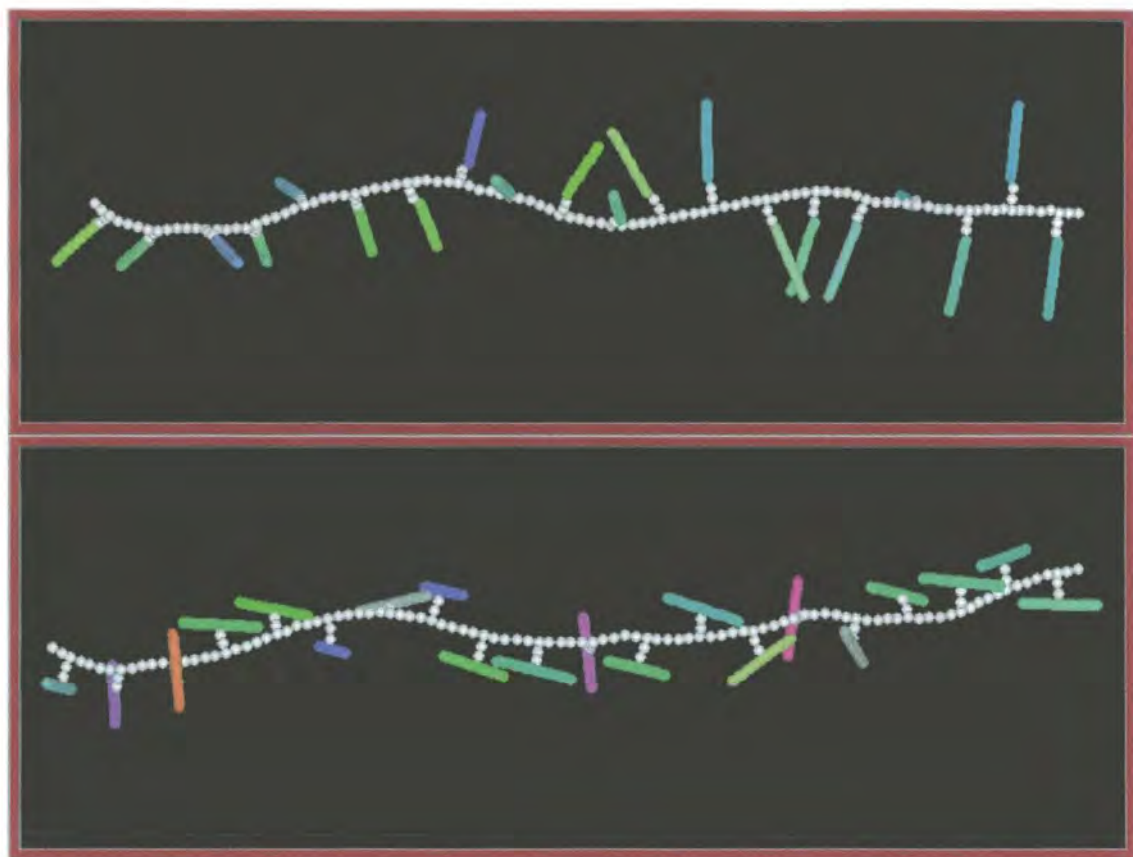
Figure 6.13: Snapshot showing a single coarse-grained polymer molecule: the terminal polymer (top) and the lateral polymer (bottom).
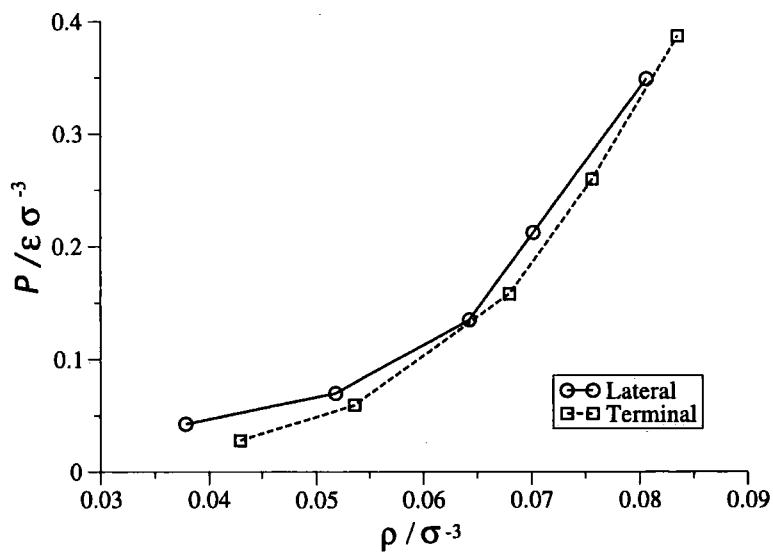
Figure 6.14: Phase diagram of the side-chain liquid crystal polymers. The bold line is for the lateral polymer system the dashed line for the terminal polymer system.
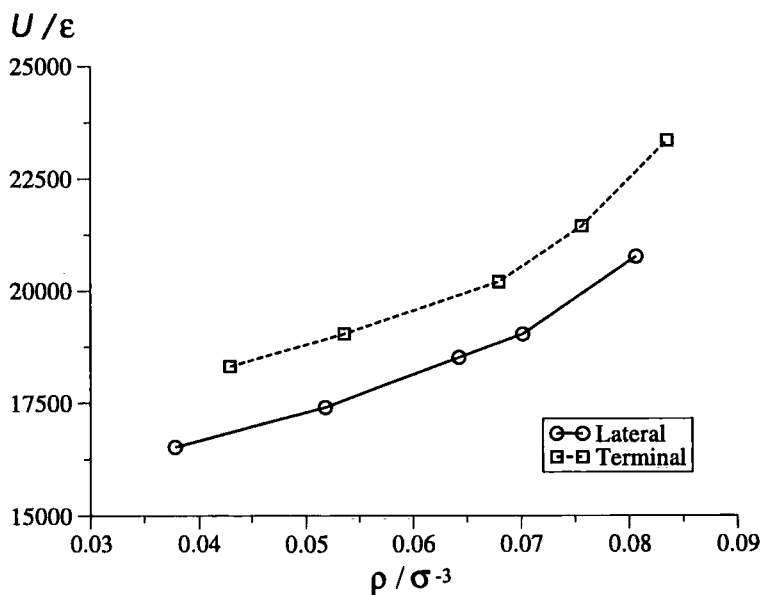
Figure 6.15: Energy as a function of density for the side-chain liquid crystal polymer systems. The bold line is for the lateral polymer system and the dashed line is for the terminal polymer system.

<div align="center">(a)   (b)</div>
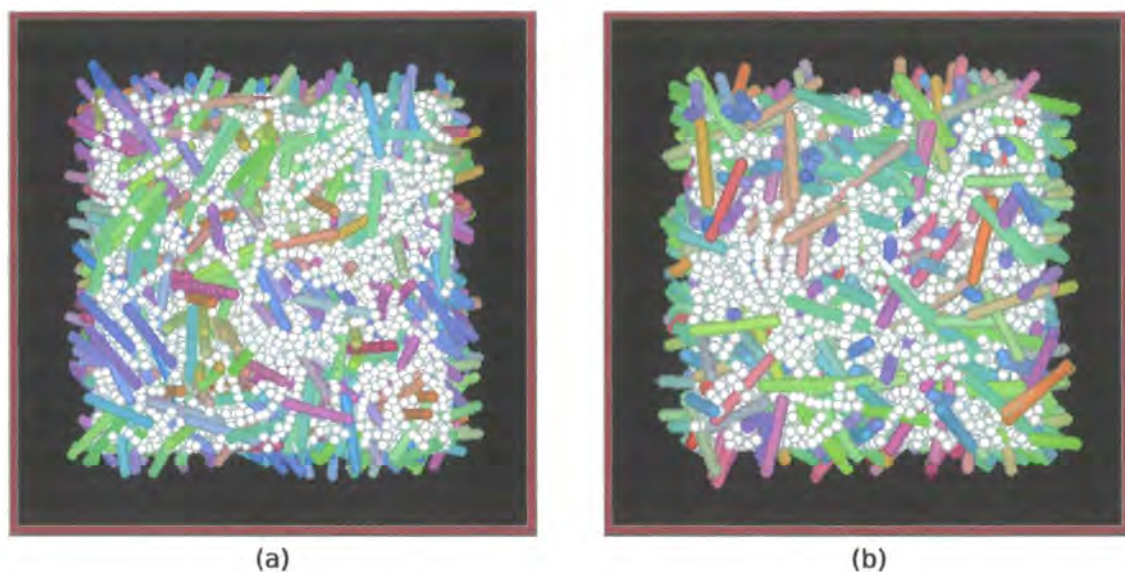
Figure 6.16: Snapshots of the polymer systems: (a) lateral polymer at $\rho = 0.0702/\sigma^{-3}$ and (b) terminal polymer at $\rho = 0.0835/\sigma^{-3}$.

at least form mesophases at a far slower rate than the alkyl chain mesogens). Obviously the polymer backbone will limit the freedom of movement of the mesogens and so the time evolution of any mesophase would be slowed down. In addition, compared with the twin chain mesogens there is a small reduction in the volume of spherocylinders in the system. In the case of the twin chain mesogens the spherocylinders account for 65.71% of the molecular volume of the system, in the polymer systems they account for 62.16% of the molecular volume. While this is only a slight reduction, combined with the greater inflexibility of the polymers it could retard mesophase formation. Another possible explanation could be that the compression of the system from the gas phase might have been carried out too quickly, freezing the system at high densities. Another reason for the lack of mesophase formation might be that the polymer backbone is too long and the molecules are becoming entangled, hence forming a polymer glass. A problem that is compounded by the relatively favourable value of the sphere-sphere potential. Obviously these reason are not mutually exclusive and it is quite possible that the lack of liquid crystal phases may be due to a combination of them all.

While there is little difference in the phase diagrams of the terminal and lateral systems, the terminal system is of higher energy than the lateral system (see figure

6.15). This difference in energy is not related to any particular term but is due to an increase in energy for all the interactions.

6.3 Coarse-grained Soft-Core Systems

The preliminary results of the extension of anisotropic soft-core models to more complex systems are mixed. For the twin alkyl chain mesogens the results look very promising, even for the simple rigid Monte Carlo model a nematic liquid crystal phase was seen. The more realistic molecular dynamics model, where sites could move in relation to each other, worked even better. Not only were both the nematic and smectic-A liquid crystal phases seen but the radial distribution functions dropped off to zero at close separations. Moreover, the use of a considerably longer timestep than would be possible with hard-core models allowed mesophases to form extremely rapidly.

These MD simulations could be expanded in a number of ways. As already mentioned it is possible to change the softness of the potentials, both in absolute terms and for different sites relative to each other. However, a more interesting area would be to alter the angles at which the chains connect to the spherocylinder in order to see if a smectic-C phase would be formed.

The soft-core potentials do not seemed to have worked effectively for the polymer systems. However, longer runs may see liquid crystal phases forming and a larger survey of the phase diagram at different temperatures might discover mesophases. Additionally making the nonbonded forces of the sphere-sphere interactions more repulsive might stop polymer backbones being "frozen" together. If the major problem is the entanglement of the polymer backbones then simulating a system of shorter polymers (ten rather than twenty repeat units long) might help liquid crystal phases to form.

Chapter 7

Conclusions

The work presented in this thesis aims to develop and apply some new simulation methods in order to improve upon the molecular simulation of macromolecular liquid crystals. The major barriers to the effective simulation of these liquid crystal macromolecules are the number of sites in the system and the long time and length scales needed for the formation of liquid crystal phases.

Coarse-graining, aims to tackle the first of these problems. Chapter 3 showed how a coarse-grained model of a liquid crystal dendrimer could be built from data obtained from more detailed simulations. The coarse-grained model represented the dendrimer using a series of spheres and spherocylinders, retaining the most important features of the dendrimer whilst reducing the number of sites greatly. This model could then be used for bulk phase simulations of the dendrimer using domain decomposition molecular dynamics, something that would be impossible using an atomistic model. In the bulk phase microphase separation of the dendrimer cores and the mesogens occurred spontaneously, but the viscosity of the system meant that the annealing of the domains was unlikely to happen on a realistic timescale. Applying a magnetic field to the system allowed the domains to anneal and a mesophase to form. For the system using spherocylinders of length $L/D = 6$, this phase was unstable without the presence of a magnetic field. However, for longer spherocylinders of $L/D = 8$ no decay in the order of the phase was seen. Analysis of the radial distribution functions determined that this layered phase was an interdigitated smectic-A phase.

In chapter 4 a simulation technique known as parallel-tempering was outlined. This method was applied to two test systems; a liquid crystal silsesquioxane dendrimer and a non-equilibrium state of 216 alkane chains. Both systems showed an improvement in the sampling of phase space by using parallel-tempering. The parallel-tempering method was then extended to work with ensembles at different potentials rather than different temperatures. The Tsallis potential was applied to the system and a sequence of increasingly soft replicas was created. For the alkane chains system there was only minor improvement in the speed at which the equilibrium state was reached. For the dendrimer system there was a noticeable improvement in the dihedral angle distributions of the system. Neither system, however, felt the full benefit of the potential softening method as the method proved difficult to optimise.

The problem of the long-time needed for the formation of mesophases in liquid crystal macromolecules was addressed in chapters 5 and 6 through the use of soft-core potentials. In chapter 5 three anisotropic single site soft-core model potentials that could be used to simulate liquid crystals were developed. Previous soft-core simulations of liquid crystals have used a series of linked spheres an approach that is more computationally demanding than using a single site model. These different soft-core potentials were then tested using a series of Monte Carlo simulations of spherocylinders. The softness of the potentials, the temperature and the length of the spherocylinders was all varied. For all the soft-core models a nematic liquid crystal phase formed, and in some simulations the formation of a smectic phase was also seen. The phase diagrams of the soft-core systems resembled those produced by the SRS potential. The different soft-core models each gave rise to a different radial distribution function, the degree at which these radial distribution functions differed from that of the SRS potential varied widely. However, increasing the length of the spherocylinders will cause $g(r)$ to become more like that of the SRS potential as the liquid crystal phases will form at lower densities, reducing the problem of particle overlap that causes the peaks in $g(r)$ at short separations.

Chapter 6 explored how soft-core potentials would behave in more complex systems, consisting of molecules made from multiple sites. A model of a liquid crystal

with terminal alkyl chains attached was simulated using both MC and MD calculations. The MD simulations made use of the soft-core nature and weak bonds of the system to apply a larger timestep than would be possible for hard-core models. Formation of liquid crystal phases was seen for both the MC and MD methods, with the liquid crystal phases forming particularly quickly in the case of the molecular dynamics simulations. MD simulations of two side chain liquid crystal polymers were also undertaken, here unfortunately no liquid crystal phase was observed to form.

There are several areas where it would be interesting to extend the work conducted in this thesis. Firstly, the investigation of multi-site systems using soft-core models could be extended much further. Initially, a more extensive investigation of the polymer systems could be carried out to see if they really are incapable of forming liquid crystal phases, and if so why? Also a greater range of systems could be tested, to determine which systems gain the greatest benefit from soft-core models.

Secondly, there are a wide range of macromolecular liquid crystal systems that could be coarse-grained, not only polymers and dendrimers but also liquid crystal fullerene macromolecules and Janus compounds.[33,34] The coarse-graining of liquid crystal Janus compounds, where the bulk phase would have domains of two different liquid crystal phases might be particularly challenging but would be a huge achievement. Utilising the ability of soft-core models to make some interactions preferential to others, might provide one path to systems containing multiple liquid crystal phases.

In addition, the coarse-graining procedure could be refined, by using radial distribution functions to improve the nonbonded interactions. This process would work by carrying out atomistic simulations of the different parts of the macromolecule to obtain the radial distribution functions. The nonbonded parameters of the coarse-grained sites could then be fitted so that they reproduced the radial distribution functions of the atomistic simulations.

In terms of the parallel-tempering technique replacing the Tsallis potential with one of the soft-core potentials for the nonbonded interactions might overcome some of the optimisation problems of the method. The development of a program that

could alter the potential of each replica automatically to ensure that the replica exchange ratio remained at about 20% would allow the full benefit of the method to be felt.

Ultimately the techniques implemented in this thesis, used either separately, or in combination, provide the tools needed to take forward the simulation of macro-molecular liquid crystals into new fields.

Bibliography

[1] F. Reinitzer, Monatshefte fur Chemie **9**, 421 (1888).

[2] G. Friedel, Ann. Physique **18**, 273 (1922).

[3] I. Sage, *Handbook of Liquid Crystals.*. volume 3 (Wiley-VCH, 1998).

[4] J. Goodby, Science **231**, 350 (1986).

[5] L. Goodman, J. Vac. Sci.Tech. **10**, 804 (1973).

[6] R. Eidenschink and A. Hager, Mol. Cryst. Liq. Cryst. **304**, 513 (1997).

[7] S. Morris, A. Ford, M. Pivnenko, and H. Coles, J. Appl. Phys. **97**, 023103 (2005).

[8] Y. Zhou, Y. Huang, A. Rapaport, M. Bass, and S. Wu, Mol. Cryst. Liquid Cryst. **454**, 377 (2006).

[9] C. Goltner and M. Antonietti, Adv. Mater. **9**, 431 (1997).

[10] A. Cammidge and R. Busby, *Handbook of Liquid Crystals.* volume 2B (Wiley-VCH, 1998).

[11] S. Chandrasekhar, B. K. Sadashiva, and K. A. Suresh, Pramana **9**, 471 (1977).

[12] K. Hiltrop, In *Liquid Crystals*, edited by H. Baumgartel, E. U. Frank, W. Grunbein, and H. Stegemeyer, chapter 4 (Springer, New York, 1994).

[13] V. Percec, P. W. Chu, G. Ungar, and J. P. Zhou, J. Am. Chem. Soc. **117**, 11441 (1995).

[14] S. A. Ponomarenko, N. I. Boiko, V. P. Shibaev, R. M. Richardson, I. J. White-house, E. A. Rebrov, and A. M. Muzafarov, Macromolecules **33**, 5549 (2000).

[15] R. M. Richardson, S. A. Ponomarenko, N. I. Boiko, and V. P. Shibaev, Liq. Cryst. **26**, 101 (1999).

[16] I. Saez and J. Goodby, Liq. Cryst. **26**, 1101 (1999).

[17] I. Saez, J. Goodby, and R. Richardson, Chem. Eur. J. **7**, 2845 (2001).

[18] I. Saez and J. Goodby, J. Mater. Chem. **11**, 2845 (2001).

[19] H. Frey and C. Schlenk, Topics in Current Chemistry **210**, 69 (2000).

[20] G. R. Newkome, C. N. Moorefield, and F. Vögtle, *Dendrimers and Dendrons.* (Wiley-VCH, 2001).

[21] C. Tschierske, J. Mat. Chem. **11**, 2647 (2001).

[22] C. Tschierske, Curr. Opin. Colloid Interface Sci. **7**, 69 (2002).

[23] C. Tschierske, Nature **419**, 681 (2002).

[24] M. W. P. L. Baars, S. H. M. Sontjens, H. M. Fischer, H. W. I. Peerlings, and E. W. Meijer, Chem.-A Eur. J. **4**, 2456 (1998).

[25] J. Knapen, A. Van Der Made, J. De Wilde, P. Van Leeuwen, P. Wijkens, D. Grove, and G. Van Koten, Nature **372**, 659 (1994).

[26] R. Gossage, L. Van De Kuil, and G. Van Koten, Acc. Chem. Res. **31**, 423 (1998).

[27] C. Lach, D. Brizzolara, and H. Frey, Macromol. Theory Simul. **6**, 371 (1997).

[28] J. Roovers, L. Zhou, P. Toporowski, M. Van Der Zwan, H. Iatrou, and N. Had-jichristidis, Macromolecules **26**, 4324 (1993).

[29] L. Zhou, N. Hadjichristidis, P. Toporowski, and J. Roovers, Rubber Chem. Tech. **65**, 303 (1992).

[30] H. Ringsdorf and A. Schneller, British Polym. J. **13**, 43 (1981).

[31] Roviello A, J. Polym. Sci., Polym. Lett. Ed. **13**, 455 (1975).

[32] W. Jackson, J. Polym. Sci., Polym. Chem. Ed. **14**, 2043 (1976).

[33] I. Saez and J. Goodby, J. Mater. Chem. **15**, 26 (2005).

[34] S. Campidelli, C. Eng, I. M. Saez, J. W. Goodby, and R. Deschenaux, Chem. Comm. **13**, 1520 (2003).

[35] J. Goodby, G. Mehl, I. Saez, R. Tuffin, G. Mackenzie, R. Auzely-Velty, T. Benvegnu, and D. Plusquellec, Chem. Comm. **19**, 2057 (1998).

[36] M. Murat and G. S. Grest, Macromolecules **29**, 1278 (1996).

[37] R. Elsasser, G. Mehl, J. Goodby, and M. Veith, Angew. Chem. Int. Ed. **40**, 2688 (2001).

[38] S. D. Hudson, H. T. Jung, V. Percec, W. D. Cho, G. Johansson, G. Ungar, and V. S. K. Balagurusamy, Science **278**, 449 (1997).

[39] V. Percec, C.-H. Ahn, T. K. Bera, G. Ungar, and D. J. P. Yeardley, Chem. Eur. J. **5**, 1070 (1999).

[40] V. Percec, C. H. Ahn, W. D. Cho, A. M. Jamieson, J. Kim, T. Leman, M. Schmidt, M. Gerle, M. Moller, S. A. Prokhorova, S. S. Sheiko, S. Z. D. Cheng, A. Zhang, G. Ungar, and D. J. P. Yeardley, J. Am. Chem. Soc. **120**, 8619 (1998).

[41] V. Percec, C. H. Ahn, G. Ungar, D. J. P. Yeardley, M. Moller, and S. S. Sheiko, Nature **391**, 161 (1998).

[42] M. R. Wilson, In *Structure and Bonding: Liquid Crystals*, edited by M. Mingos, volume 94 (Springer-Verlag, Heidelberg, 1999).

[43] P. A. Lebwhol and G. Lasher, Phys. Rev. A **6**, 426 (1972).

[44] C. Chiccoli, P. Pasini, and C. Zannoni, Liq. Cryst. **2**, 39 (1987).

[45] M. J. Cook and M. R. Wilson, Molecular Crystals and Liquid Crystals **363**, 181 (2001).

[46] D. L. Cheung, S. J. Clark, and M. R. Wilson, Chem. Phys. Lett. **356**, 140 (2002).

[47] D. L. Cheung, S. J. Clark, and M. R. Wilson, J. Chem. Phys. **121**, 9131 (2004).

[48] M. J. Cook and M. R. Wilson, Mol. Cryst. Liq. Cryst. **363**, 181 (2001).

[49] D. Frenkel, J. Phys. Chem. **92**, 3280 (1988).

[50] S. C. McGrother, D. C. Williamson, and G. Jackson, J. Chem. Phys. **104**, 6755 (1996).

[51] D. Frenkel, H. N. W. Lekkerkerker, and A. Stroobants, Nature **332**, 822 (1988).

[52] J. A. C. Veerman and D. Frenkel, Phys. Rev. A **41**, 3237 (1990).

[53] A. L. Onsager, NY Acad. Sci. **51**, 627 (1949).

[54] D. Williamson and F. del Rio, J. Chem. Phys. **109**, 4675 (1998).

[55] D. Williamson and Y. Guevara, J. Phys. Chem. **103**, 7522 (1999).

[56] A. Cuetos, B. Martinez-Haya, L. F. Rull, and S. Lago, J. Chem. Phys. **117**, 2934 (2002).

[57] K. Aoki, Mol. Cryst Liq. Cryst. **299**, 45 (1997).

[58] K. Aoki, Mol. Cryst. Liq. Cryst. **262**, 543 (1995).

[59] K. Aoki, Mol. Sim. **16**, 99 (1996).

[60] D. J. Earl, J. Ilnytskyi, and M. R. Wilson, Mol. Phys. **99**, 1719 (2001).

[61] J. G. Gay and B. J. Berne, J. Chem. Phys. **74**, 3316 (1981).

[62] E. de Miguel, E. M. del Rio, J. T. Brown, and M. P. Allen, J. Chem. Phys. **105**, 4234 (1996).

[63] G. R. Luckhurst, R. A. Stephens, and R. W. Phippen, Liq. Cryst. **8**, 451 (1990).

[64] E. de Miguel, L. F. Rull, M. K. Chalam, and K. E. Gubbins, Molec. Phys. **71**, 1223 (1990).

[65] R. Berardi, A. P. Emerson, and C. Zannoni, J. Chem. Soc. Faraday Trans. **89**, 4069 (1993).

[66] A. P. J. Emerson, G. R. Luckhurst, and S. G. Whatling, Mol. Phys. **82**, 113 (1994).

[67] R. Memmer, H. G. Kuball, and A. Schonhofer, Liq. Cryst. **15**, 345 (1993).

[68] R. Berardi and C. Zannoni, J. Chem. Phys. **113**, 5971 (2000).

[69] R. Berardi, S. Orlandi, and C. Zannoni, Int. J. Mod. Phys. C **10**, 477 (1999).

[70] C. Zannoni, J. Mater. Chem. **11**, 2637 (2001).

[71] M. P. Neal and A. J. Parker, Mol. Cryst. Liq. Cryst. **330**, 1809 (1999).

[72] U. Burkert and N. L. Allinger, *Molecular Mechanics*, chapter 3 (American Chemical Society, 1982).

[73] N. L. Allinger, Rev. Phys. Org. Chem. **13**, 1 (1976).

[74] C. H. Langley, J. H. Lii, and N. L. Allinger, J. Comp. Chem. **22**, 1476 (2001).

[75] N. L. Allinger and D. Y. Chung, J. Am. Chem. Soc. **98**, 6798 (1976).

[76] N. L. Allinger, M. T. Tribble, M. A. Miller, and D. H. Wertz, J. Am. Chem. Soc. **93**, 1637 (1971).

[77] W. D. Cornell, P. Cieplak, C. I. Bayly, I. R. Gould, K. M. M. Jr., D. M. Ferguson, D. C. Spellmeyer, T. Fox, J. W. Caldwell, and P. A. Kollman, J. Am. Chem. Soc. **117**, 5179 (1995).

[78] S. J. Weiner, P. A. Kollman, D. A. Case, U. C. Singh, C. Ghio, G. Alagona, S. Profeta, and P. Weiner, J. Am. Chem. Soc. **106**, 765 (1984).

[79] W. Jorgensen, D. Maxwell, and J. TiradoRives, J. Am. Chem. Soc. **118**, 11225 (1996).

[80] W. L. Jorgensen and N. A. McDonald, Theochem - J. Molec. Structure **424**, 145 (1998).

[81] N. L. Allinger, J. Am. Chem. Soc. **99**, 8127 (1977).

[82] N. L. Allinger, Y. H. Yuh, and J. Lii, J. Am. Chem. Soc. **111**, 8551 (1989).

[83] N. Nevins, K. S. Chen, and N. L. Allinger, J. Comp. Chem. **17**, 669 (1996).

[84] N. L. Allinger, K. S. Chen, and G. M. A. J. A. Katzenellenbogen, S. R. Wilson, J. Comp. Chem. **17**, 747 (1996).

[85] W. Jorgensen, J. Madura, and C. Swenson, J. Am. Chem. Soc. **106**, 6638 (1984).

[86] N. Metropolis and S. Ulam, J. Am. stat. Ass. **44**, 335 (1949).

[87] M. R. Wilson, J. Chem. Phys. **107**, 8654 (1997).

[88] P. Pant and D. Theodorou, Macromolecules **28**, 7224 (1995).

[89] V. Mavrantzas, T. Boone, E. Zervopoulou, and D. Theodorou, Macromolecules **32**, 5072 (1999).

[90] N. Karayiannis, A. Giannousaki, V. Mavrantzas, and D. Theodorou, J. Chem. Phys. **117**, 5465 (2002).

[91] L. Verlet, Phys. Rev. **159**, 98 (1967).

[92] W. Swope, H. C. Andersen, P. H. Berens, and K. R. Wilson, J. Chem. Phys. **76**, 637 (1982).

[93] H. Andersen, J. Chem. Phys. **72**, 2384 (1980).

[94] H. J. C. Berendsen, J. P. M. Postma, W. F. VanGunsteren, A. DiNola, and J. R. Haak, J. Chem. Phys. **81**, 3684 (1984).

[95] S. Nosé, Molec. Phys. **52**, 255 (1984).

[96] W. G. Hoover, Phys. Rev. A **31**, 1695 (1985).

[97] S. Toxvaerd, Phys. Rev. E **47**, 343 (1993).

[98] M. Wilson, In *Advances in the Computer Simulations of Liquid Crystals*, edited by P. Pasini and C. Zannoni, chapter 13, 389–412 (Kluwer Academic Publishers, 2000).

[99] P. Hilbers and K. Esselink, In *Computer Simulations in Chemical Physics*, edited by M. P. Allen and D. J. Tildesley, 473–493 (Kluwer, The Netherlands, 1992).

[100] W. Smith, Comp. Phys. Comm. **62**, 229 (1991).

[101] M. R. Wilson, M. P. Allen, M. A. Warren, A. Sauron, and W. Smith, J. Comp. Chem. **18**, 478 (1997).

[102] J. Ilnytskyi and M. R. Wilson, Comp. Phys. Comm. **134**, 23 (2001).

[103] J. Ilnytskyi and M. R. Wilson, Comp. Phys. Comm. **148**, 43 (2002).

[104] P. Hoogerbrugge and J. Koelman, **19**, 155 (1992).

[105] P. Espanol and P. Warren, Europhys. Lett. **30**, 191 (1995).

[106] R. D. Groot and P. B. Warren, J. Chem. Phys. **107**, 4423 (1997).

[107] Y. K. Levine, A. E. Gomes, A. F. Martins, and A. Polimeno, J. Chem. Phys. **122**, 144902 (2005).

[108] A. E. Gomes, A. F. Martins, and A. Polimeno, Molec. Crys. Liq. Cryst. **435**, 795 (2005).

[109] S. Willemsem, T. Vlugt, H. Hoefsloot, and B. Smit, J. Comp. Phys. **147**, 507 (1998).

[110] L. M. Stimson, Ph.D. thesis, University of Durham (2003).

[111] M. R. Wilson, J. M. Ilnytskyi, and L. M. Stimson, J. Chem. Phys. **119**, 3509 (2003).

[112] O. Hahn, L. D. Site, and K. Kremer, Macromol. Theory Simul. **10**, 288 (2001).

[113] W. Tschöp, K. Kremer, J. Batoulis, T. Bürger, and O. Hahn, Acta. Polym. **49**, 61 (1998).

[114] M. R. Wilson, J. Chem. Phys. **107**, 8654 (1997).

[115] C. McBride and M. R. Wilson, Mol. Phys. **97**, 511 (1999).

[116] K. Kremer and G. S. Grest, J. Chem. Phys. **92**, 5057 (1989).

[117] A. G. Vanakaras and D. J. Photinos, J. Mater. Chem. **11**, 2832 (2001).

[118] R. M. Richardson, E. B. Barmatov, I. J. Whitehouse, V. P. Shibaev, T. Yongjie, and M. H. F. Godhino, Mol. Cryst. Liq. Cryst. **330**, 285 (1999).

[119] L. M. Stimson and M. R. Wilson, J. Chem. Phys. **123**, 034908 (2005).

[120] V. Percec, W. D. Cho, and G. Ungar, J. Am. Chem. Soc. **122**, 10273 (2000).

[121] M. Lee, B. K. Cho, K. J. Ihn, W. K. Lee, N. K. Oh, and W. C. Zin, J. Am. Chem. Soc. **123**, 4647 (2001).

[122] S. Pensec, F. G. Tournilhac, P. Bassoul, and C. Durliat, J. Phys. Chem. B **28**, 3080 (1995).

[123] R. Stadler, C. Auschra, J. Beckmann, U. Krappe, I. Voigtmartin, and L. Leibler, Macromolecules **28**, 3080 (1995).

[124] V. Percec, M. Glodde, T. K. Bera, Y. Miura, I. Shiyanovskaya, K. D. Singer, V. S. K. Balagurusamy, P. A. Heiney, I. Schnell, A. Rapp, H. W. Spiess, S. D. Hudson, and H. Duan, Nature **419**, 384 (2002).

[125] V. Percec, A. E. Dulcey, V. S. K. Balagurusamy, Y. Miura, J. Smidrkal, M. Peterca, S. Nummelin, U. Edlund, S. D. Hudson, P. A. Heiney, D. A. Hu, S. N. Magonov, and S. A. Vinogradov, Nature **430**, 764 (2004).

[126] D. Earl and M. Deem, Phys. Chem. Chem. Phys. **7**, 3910 (2005).

[127] C. Geyer, *Computing Science and Statistics Proceedings of the 23rd Symposium on the Interface*, 156 (American Statistical Association, New York, 1991).

[128] U. Hansmann, Chem. Phys. Lett. **281**, 140 (1997).

[129] Y. Sugita and Y. Okamoto, Chem. Phys. Lett. **314**, 141 (1999).

[130] H. Kokubo and Y. Okamoto, J. Chem. Phys. **120**, 10837 (2004).

[131] M. Falcioni and M. Deem, J. Chem. Phys. **110**, 1754 (1999).

[132] R. Swendsen and J.-S. Wang, Phys. Rev. Lett. **57**, 2607 (1986).

[133] R. Zhou, J. Mol. Graphics Modell. **22**, 451 (2004).

[134] V. Favre-Nicolin and R. Cerny, J. Appl. Crystallogr. **35**, 734 (2002).

[135] P. Zavalij, S. Yang, and M. Whittingham, Acta Crystallogr. **B59**, 753 (2003).

[136] Q. Yan and J. de Pablo, J. Chem. Phys. **113**, 1276 (2000).

[137] A. Bunker and B. Dunweg, Phys. Rev. E **63**, 016701 (2000).

[138] D. Bedrov and G. Smith, J. Chem. Ohys. **115**, 1121 (2001).

[139] F. Calvo, J. Phys. Chem. **105**, 2183 (2001).

[140] F. Chuaung, C. Ciobanu, C. Predescu, C. Wang, and K. Ho, Surf. Sci. **578**, 183 (2005).

[141] M. Habeck, M. Nilges, and W. Riepling, Phys. Rev. Lett. **94**, 018105 (2005).

[142] D. Kofke, J. Chem. Phys. **117**, 6911 (2002).

[143] D. Kofke, J. Chem. Phys. **120**, 10852 (2004).

[144] D. Kofke, J. Chem. Phys. **121**, 1167 (2004).

[145] A. Kone and D. Kofke, J, Chem. Phys. **122**, 206101 (2005).

[146] N. Rathore, M. Chopra, and J. de Pablo, J. Chem. Phys. **122**, 024111 (2005).

[147] M. Wilson, Liq. Cryst. **21**, 437 (1996).

[148] Q. Yan and J. de Pablo, J. Chem. Phys. **111**, 9509 (1999).

[149] C. Tsallis, J. Stat. Phys. **52**, 479 (1988).

[150] I. Andricioaei and J. Straub, Phys. Rev. E **53**, R3055 (1996).

[151] I. Andricioaei and J. Straub, J. Chem. Phys. **107**, 9117 (1997).

[152] T. Whitfield, L. Bu, and J. Straub, Physica A **305**, 157 (2002).

[153] S. Wang and Y. Pak, J. Chem. Phys. **111**, 4359 (1999).

[154] Y. Pak, S. Jang, and S. Shin, J. Chem. Phys. **116**, 6831 (2002).

[155] S. Jang, S. Shin, and Y. Pak, Phys. Rev. E **91**, 058305 (2003).

[156] A. AlSunaidi, W. Den Otter, and J. Clarke, Phil. Trans. Roy. Soc. London A. **1821**, 1773 (2004).

[157] T. Beutler, A. Mark, R. van Schaik, P. Gerber, and W. van Gunsteren, Chem. Phys. Lett. **222**, 529 (1994).

[158] D. J. Earl, J. Ilnytskyi, and M. R. Wilson, Molec. Phys. **99**, 1719 (2001).

[159] M. R. Wilson, J. Chem. Phys. **107**, 8654 (1997).

[160] A. Lyulin, M. Al-Barwani, M. Allen, M. Wilson, I. Neelov, and N. Allsopp, Macromolecules **31**, 4626 (1998).

[161] R. Groot, Langmuir **16**, 7492 (200).

[162] A. Schlijper, P. Hoogerbrugge, and C. Manke, J. Rheol. **39**, 567 (1995).

[163] Y. Kong, C. Manke, W. Madden, and A. Schlijper, Int. J. Thermophys. **39**, 567 (1994).

Appendix A

Conferences, Courses and Seminars Attended

A.1   Conferences

British Liquid Crystal Society Winter Workshop

University of Hull, U.K., 15th-17th December. 2003

Work presented in poster format.

British Liquid Crystal Society Conference

University of Manchester, U.K., 5th-7th, 2004

Work presented in poster format.

Simu: Bridging the Scales

Genoa, Italy, 29th-31st August, 2004

Work presented in poster format.

Conference on Computational Physics (CCP) 2004

Genoa, Italy, 1st-4th September, 2004

Work presented in poster format.

British Liquid Crystal Society Conference

University of Exeter, UK, 22nd-24th March, 2005

Work presented in poster format.

Thermodynamics 2005

Sesimbra, Portugal, 6th-8th April, 2005

Work presented in poster format.

6th Liquid Matter Conference

Utrecht, the Netherlands, 2nd-6th July, 2005

Work presented in poster format.

Royal Society Discussion Meeting on New Directions in Liquid Crystal Science

London, U.K., 5th-6th December, 2005

British Liquid Crystal Society Conference

University of York, U.K., 11th-13th April, 2006

Work presented in poster format.

21st International Liquid Crystal Conference

Keystone, Colorado, U.S.A., 2nd-7th July, 2006

Work presented in poster format.

A.2   Courses

Introduction to FORTRAN Programming

Information Technology Service, Durham University

Introduction to Unix

Information Technology Service, Durham University

Further Unix

Information Technology Service, Durham University

Numerical Methods and Data Analysis

Department of Chemistry, Durham University

Diffraction and Scattering Methods

Department of Chemistry, Durham University

Practical and Electronic Structure Calculations

Department of Chemistry, Durham University

Experimental Design

Department of Chemistry, Durham University

Teaching and Demonstrating

Centre for Learning, Teaching and Research in Higher Education, Durham University

A.3   Seminars

Applications of catalytic asymmetric C-H activation to organics synthesis
Prof. Huw Davis, 15th October, 2003

Pouring oil on troubled waters: wetting and phase transitions in oil drops on surfactant solutions
Dr. Colin Bain, 5th November, 2003

A new molecular orbital description derived from ZEKE (Zero Electron Kinetic Energy) photoelectron spectroscopy with rotational resolution
Prof. Klaus Mueller-Dethlefs, 11th November, 2003

Electrochemical and spectrochemical studies of transition metal complexes

Dr. Lesley Yellowlees, 28th January, 2003

Protein folding and misfolding from and NMR perspective

Prof. J. Waltho, 18th February, 2004

Expression of quantum cellular automata, surface bound mixed-valence complexes as field switchable charge containers

Prof. Thomas P. Fehlner, 10th March, 2004

Bottom-up assembly of peptide-based supermolecular and nanoscale structures

Dr. D. N. Woolfson, 24th March, 2004

Gas sorption by organic crystals

Prof. Leonard J. Barbour, 15th November, 2004

New methodology for organic synthesis

Prof. Varinder Aggarwal, 17th November, 2004

Computer simulations of chemical reactions in complex systems: from proton transfer to ligand binding

Prof. Markus Meuwly, 23rd February, 2005

Molecular tailoring of solid surfaces

Prof. J. P. S. Badyal, 4th May, 2005

Understanding phase transitions in chiral systems of biological interest

Prof. George Jackson, 18th May, 2005

First-principles predictions for water: clusters and condensed phases

Prof. Pavel Kocovsky, 25th May, 2005

Protein folding - nature's origami

Dr. Lorna Smith, 22nd June, 2005

Chemical Nanoengineering

Prof. Jon A. Preece, 26th October, 2005

How do calculated kinetic isotope effects relate to transition state structure

Prof. Ian Williams, 16th November, 2005

Mass spectrometry: the analytical challenge of the post-genomic era

Prof. Jane Thomas-Oates, 30th November, 2005

Ultrafast excited-state processes of d6-metal carbonyl-diimine complexes: from excitation to photochemistry

Prof. A. Vicek, 11th January, 2006

Beyond nano - the chemistry of emergence

Prof. Stephen Mann, 1st March, 2006

3rd Year Postgraduate Poster Symposium

4th May, 2006

2nd Year Postgraduate Symposium

10th May, 2006

Precise synthesis and properties of organometallic dendrimers

Dr. Kiyotaka Onitsuka, 15th May, 2006

3rd Year Postgraduate Symposium
15th-16th May, 2006

Aspects of chemical biology: diversity based synthesis and oxidative stress
Dr. Richard Hartley, 14th June, 2006

A.4   Publications

Hughes, Z.E., Wilson, M.R. and Stimson, L.M., Coarse-grained simulation studies of a liquid crystal dendrimer: towards computational predictions of nanoscale structure through microphase separation, *Soft Matter*, **1**, 436 (2005)

Wilson, M.R., Ilnytskyi, J.I., Stimson, L.M. and Hughes, Z.E., Computer simulations of liquid crystal polymers and dendrimers in *Computer Simulation of Liquid Crystals and Polymers*, edited by Pasini, P., Zannoni, C. and Zumer, S., 57-78, (Kluwer, 2004)